UNIVERSITÀ DEGLI STUDI DI NAPOLI FEDERICO II

PH.D. THESIS IN

INFORMATION TECHNOLOGY AND ELECTRICAL ENGINEERING

SCATTERING MODELS IN REMOTE SENSING

APPLICATION TO SAR DESPECKLING AND SEA TARGET DETECTION FROM SPACEBORNE GNSS-R IMAGERY

ALESSIO DI SIMONE

TUTOR: PROF. DANIELE RICCIO

XXIX CICLO

SCUOLA POLITECNICA E DELLE SCIENZE DI BASE
DIPARTIMENTO DI INGEGNERIA ELETTRICA E TECNOLOGIE DELL'INFORMAZIONE

To my parents, Rosa and Raimondo,
to my wife, Roberta,
and to our child she's carrying

This page intentionally left blank.

Preface

This Book is a compendium of the results of my research activities carried out within the Ph.D. degree in Information Technology and Electrical Engineering at the University of Naples “Federico II”. The main research topics are related to the remote sensing field using, in particular, synthetic aperture radar (SAR) and Global Navigation Satellite System-Reflectometry (GNSS-R) data. The research activities started from the idea that remote sensing applications and techniques could greatly benefit from a proper modeling of the complex scattering phenomena involved in remote sensing technologies. Starting from this general statement, two research topics were identified and investigated leading to the results presented in this Book. The first one concerns SAR despeckling, i.e., the problem of reducing speckle noise effects in SAR imagery to improve the readability and the understanding of SAR products. It has been my primary research topic studied during the Ph.D. course, and, consequently, the most investigated and assessed. The main result related to this topic is the development of two despeckling algorithms based on the exploitation of a priori information about the scattering behavior of the illuminated surface. The proposed algorithms represent a modified version of pre-existing techniques to account for the a priori scattering information. The exploitation of such information allows for a significant performance enhancement with respect to the original filters in terms of both speckle reduction in homogeneous areas and details preservation in presence of non-negligible topography.

The second topic of research has been conducted during a four-month stay at the Polytechnic University of Catalonia in collaboration with the Passive Remote Sensing Group led by Adriano Camps. It comprises the development, implementation, and validation of a sea target detection algorithm using GNSS-R observables. Notwithstanding the poor spatial resolution, GNSS-R instruments have been shown to be capable to detect sea targets from spaceborne platforms and to provide a useful help to other well-assessed remote sensing technologies, primarily optical satellites and SAR systems, owing to the low revisit time exhibited by constellations of potential future GNSS-R satellites.

All algorithms proposed in this Ph.D. Thesis have been implemented in MATLAB R2016a and are provided in the attached DVD, along with some sample data.

In order to let the reader understand the concepts, ideas and techniques developed within my research activities and presented in this Book, some preliminary chapters about basic concepts of electromagnetism and remote sensing have been inserted. For more details about the treated topics, the reader is referred to the quoted literature.

Alessio Di Simone
University of Naples "Federico II"
February 2017

Contents

This page intentionally left blank.

List of Acronyms

The following acronyms are used throughout this text.

2-D	Two-Dimensional
3-D	Three-Dimensional
AIS	Automatic Identification System
AWGN	Additive White Gaussian Noise
CDMA	Code Division Multiple Access
CFAR	Constant False Alarm Rate
DDM	Delay-Doppler Map
DEM	Digital Elevation Model
EM	Electromagnetic
ENL	Equivalent number of looks
fBm	fractional Brownian motion
FDMA	Frequency Division Multiple Access

GNSS	Global Navigation Satellite System
GNSS-R	GNSS-Reflectometry
GO	Geometrical Optics
IEM	Integral Equation Method
KA	Kirchhoff Approximation
LEO	Low Earth Orbit
LFSR	Linear Feedback Shift Registers
LSF	Least Square Fitting
MAP	Maximum a Posteriori
NLM	non-local means
NRCS	Normalized Radar Cross Section
pdf	probability density function
PO	Physical Optics
PPB	Probabilistic Patch-Based
PPS	Precise Positioning Service
PRF	Pulse Repetition Frequency
PRN	Pseudo-Random Noise
PSF	Point Spread Function
RAR	Real Aperture Radar
RCS	Radar Cross Section

RNSS	Radio Navigation Satellite Service
RO	Radio Occultation
ROC	Receiver Operating Characteristic
SAR	Synthetic Aperture Radar
SARBM3D	SAR Block-Matching 3-D
SB	Scattering-Based
SNR	Signal-to-Noise Ratio
SPM	Small-Perturbation Method
SPS	Standard Positioning Service
TDS-1	TechDemoSat-1
UDWT	Undecimated Discrete Wavelet Transform
WAF	Woodward Ambiguity Function
WMLE	Weighted Maximum Likelihood Estimation
WT	Wavelet Transform

This page intentionally left blank.

List of Tables

This page intentionally left blank.

List of Figures

Chapter 1

Introduction

Remote sensing represents a fundamental tool for Earth observation and monitoring and for the study and analysis of other celestial bodies. In its broadest definition, *remote sensing* is *the acquisition of information at a distance.* However, this extensive definition must be refined in order to better focus on the topics treated in this Ph.D. Thesis and exclude some concepts, methodologies and technologies that could be reasonably included in wider definitions, such as sensing the Earth's magnetic field or atmosphere or the temperature of the human body. In this Ph.D. Thesis, the following focused definition by J. B. Campbell will be used [1]:

> *"Remote sensing is the practice of deriving information about the Earth's land and water surfaces using images acquired from an overhead perspective, using electromagnetic radiation in one or more regions of the electromagnetic spectrum, reflected or emitted from the Earth's surface."*

Within this definition, remote sensing stands for the set of procedures and methodologies aimed at gathering Earth's surface information by means of irradiation and acquisition of Electromagnetic (EM) waves. The frequency range adopted impacts hardware as well as the acquirable information and, consequently, applications of the remote sensing systems. Radar remote sensing typically uses microwave and millimeter wave propagation, whereas optical sensors rely on light propagation; finally, the lidar remote sensing is based on the emission and reflection of laser pulses in near infrared, visible, and ultraviolet regions of the EM spectrum. Whatever the source, remote sensing is strictly related to the EM wave propagation and reflection/scattering from natural or man-made surfaces and, therefore, to the complex phenomenology of the radiation-matter interactions. However, EM theory provides analytical solutions only in few canonical cases, in which a closed-form expression for the scattered field is derived in a deterministic framework. When dealing with remote sensing data, these cases very rarely represent an adequate model. For instance, for scattering evaluation purposes, large ice sheets and very calm sea can be modeled as infinite planes. In most cases, the reflecting interface has to be modeled as a random rough surface, thus causing random variations of the acquired signal. In such cases, the actual signal measurements cannot be predicted and relevant information about the illuminated surface is gathered from signal statistics.

1.1 Motivations

Imaging sensors are an essential tool for the observation of the Earth's surface and the study of other celestial bodies. The capability to produce radar images of the illuminated surface is strictly related with the complex phenomenology of the radiation-matter interaction. The electromagnetic scattering theory is a well-established and well-assessed topic in electromagnetics; however, its usage in the remote sensing field is not adequately investigated and studied. The motivations for this Ph.D. Thesis arose from the idea of applying scattering models in remote sensing data and exploiting a priori information about the scattering behavior of the illuminated surface to improve performance of existing algorithms and to allow for novel applications. In particular two main topics were identified, investigated and discussed in this Ph.D. Thesis:

I. Synthetic Aperture Radar (SAR) despeckling.

SAR data represent an essential tool for monitoring Earth resources and analyzing both urban and natural areas. As the very recent ESA Sentinel mission shows, SAR systems and sensors play a key role in understanding, controlling, and preserving our surrounding environment. However, SAR image readability and information retrieval procedures are dramatically affected by *speckle*, the multiplicative noise typical of coherent acquisition systems, like SAR. Consequently, analysis and understanding of a single-look SAR image are often a difficult task even for SAR-expert users [2]. In the last decades, with the introduction of increasingly powerful hardware and software resources, huge efforts have been made in the despeckling field, aimed at the reduction of speckle effects to increase the readability of SAR data and, consequently, the potential users. Numerous kinds of approaches and methods facing the despeckling problem have been proposed so far, as it can be appreciated from the surveys in [3], [4], [5]. The first technique is the so-called spatial multilook, simply based on an incoherent averaging of neighboring pixels within a fixed window. Despite its simplicity, this technique is the best (in terms of mean-squared error) in the case of homogeneous SAR images, i.e., SAR images of surfaces with constant geometrical and electromagnetic parameters. Unluckily, in most cases, a homogeneous SAR image is not of practical interest, and it is of really rare occurrence. Typically, SAR images depict a very inhomogeneous scenario, i.e., regions characterized by spatial variations of at least one of the numerous parameters influencing SAR image formation (dielectric constant, electrical conductivity, microscopic and macroscopic roughness). Depending on these parameters variations, SAR images present several features like edges — typically associated with changes of the electromagnetic parameters of the surface — textures and patterns — typically associated with changes of the geometric parameters of the surface — homogeneous regions, and so on. The huge amount of information carried by these features makes their preservation of key importance in despeckling.

Seeking inspiration from the huge literature about denoising of signals affected by the Additive White Gaussian Noise (AWGN) has been, for a long time, the most followed approach in the development of despeckling algorithms for SAR images: as a matter of fact, numerous both old and recent techniques used the homomorphic approach, taking the logarithm of the data [6], [7], [8]. Despite their simplicity and analytical tractability, the homomorphic approach causes a severe distortion of the dynamics, as well as of the fundamental properties of the SAR data. In fact, the log-transformed speckle noise is neither Gaussian nor zero-mean so that AWGN denoising methods would not provide reliable results unless these noise peculiarities are properly taken into account. As soon as speckle statistical descriptions and models became available in literature [9], [10] and the denoising community became more aware about the peculiarities of SAR images [11], e.g., spatial nonstationarity, more advanced techniques were conceived and developed [12], [13], [14], [15], [16], [17], [18], [19], [20].

As an alternative to the previous techniques, all operating in the native data domain, i.e., the spatial one, the 1990s saw the rapid diffusion of the wavelet-based denoising techniques [8], [21], [22], [23], [24]. This approach allows for both huge noise reduction and detail preservation, owing to the sparse representation of the signal in the transformed domain. Wavelet transform ensures a very accurate separation between signal and noise, also with richly detailed images, so that excellent and promising results are provided by wavelet-based approaches.

More recently, the non-local means (NLM) approach, first introduced in [25], has been developed, and it represents a candidate breakthrough in the despeckling community. The basic idea is to provide an estimate of the clean image via a proper averaging of similar pixels or patches, i.e., blocks of close pixels. The main contribution is to introduce, in a very basic way, some physical concepts by means of an intensity-based similarity criterion rather than of a pure geometrical one. NLM techniques are actually of great interest, owing to their edge preservation and speckle reduction capabilities [24], [25], [26]. The nonlocal filter proposed in [25], optimal for AWGN, was generalized to SAR imagery and speckle noise by Deledalle *et al.* in [26], introducing a distance suitable for the Nakagami–Rayleigh distribution typical of SAR speckle noise. An improved version of the filter in [26] suitable for both polarimetric and interferometric SAR data has been published very recently [27].

Despite their peculiarities, all of the aforementioned approaches suffer a general lack of physically based concepts: despeckling is considered as a pure statistical estimation problem, without taking into account the physical phenomenology inherent to the SAR image acquisition process. However, electromagnetic scattering phenomena play a key role in the SAR image formation process: as a matter of fact, SAR data can be modeled as the reflectivity pattern of the illuminated scene filtered by the SAR system [28], [29], as it will be discussed further in this Ph.D. Thesis. The past and current representation-based approaches in denoising SAR images could be substituted by the more meaningful and promising object-based approach, in which the similarity criterion is evaluated on the object properties rather than on those ones relevant to its representation through the sensor. However, an object-based approach cannot be performed without taking into account the physics behind the data acquisition and the related phenomena, which, in the SAR case, are essentially represented by scattering. In the meantime, the availability of both closed-form scattering models and a more accurate knowledge of all the parameters and phenomena involved in electromagnetic scattering from natural surfaces call for the introduction of scattering concepts in the despeckling chain in order to obtain a significant improvement of the state of the art.

In this Ph.D. Thesis, we describe the novel idea of despeckling based on scattering phenomena hidden behind SAR image formation. This general idea is applied to two well-known state-of-the-art despeckling algorithms - namely the SAR Block-Matching 3-D (SARBM3D) and the Probabilistic Patch-Based (PPB) filters proposed in [24] and [26], respectively - by employing a scattering-based similarity criterion. In particular, an EM scattering model suitable to natural surfaces has been selected, and then, the original filters have been modified in order to account for the a priori information about the EM behavior of the scattering cell. The new filters have been called Scattering-Based (SB)-PPB and SB-SARBM3D. The proposed approach requires the knowledge of the scene topography. As discussed more in detail in this Ph.D. Thesis, this does not significantly limit the applicability of the proposed methods since accurate Digital Elevation Model (DEM)s are by now easily available for most part of the world.

II. Sea target detection from GNSS-Reflectometry (GNSS-R) imagery.

The monitoring of inhomogeneous features on the sea surface, such as ice sheets and ships, impacts hydrological, biological, chemical and geological processes at and near the Earth's surface. Ice sheet mapping plays a key role in numerous applications, such as climate changes analysis and maritime security. Despite their high accuracy, in-situ measurements only provide local information and a coverage limited to the Northern Hemisphere midlatitudes [30]. In order to address accurate ice sheet mapping at a global scale, spaceborne measurements from satellite constellations come into play. Detection and monitoring of ships is important in maritime traffic control, illegal activities prevention, environment and pollution control, and naval warfare [31]. Despite the comprehensive information – name, speed, course, etc. – purchasable, the Automatic Identification System (AIS) protocol allows for sea traffic control within a limited area off the coastal line [31]. Remote sensing provides an unquestionable support in sea and ice monitoring, thanks to the global coverage. In particular, during the last three decades, SAR and optical data have been extensively exploited in the sea target detection field [31], [32], [33], [34] with an increased interest after the launch of recent missions, such as RADARSAT-2, COSMO-SkyMed, and the EU Copernicus system. Despite their high spatial resolution, SAR and optical satellites offer a temporal resolution, i.e., revisit time, on the order of days that affects the exploitation of such systems for near real-time sea monitoring. Indeed, it is noteworthy that a temporal resolution on the order of hours or less is required for ship detection [35]; the World Meteorological Organization indicates a revisit time of the order of hours for sea-ice cover concerning the Global Numerical Weather Prediction, climate monitoring and ocean applications [36]. GNSS-R is a recently remote sensing approach mainly exploited for sea state estimation [37], [38]. Due to its low cost, low power consumption, low size, and low weight, GNSS-R instruments can be launched in constellation formation at a relative low cost, fulfilling the temporal requirements for near real-time ship and ice monitoring as shown further in this Ph.D. Thesis.

Thanks to the short revisit time and high global coverage of potential future GNSS-R constellations, the sea target detection problem is expected to benefit from GNSS-R imagery. However, these very recent topics have not been properly and deeply investigated yet, and very few works focusing especially on the assessment and feasibility of ship detection from GNSS-R observables can be found in the related literature [39], [40], [41], [42], [43].

The main contributions to sea target detection using GNSS-R data described in this Ph.D. Thesis are as follows:

- Numerical analysis of the revisit time provided by constellations of GNSS-R instruments by means of realistic simulated missions;
- Derivation and implementation of a sea target detection algorithm from spaceborne GNSS-R Delay-Doppler Map (DDM)s;
- Validation of the algorithm using actual GNSS-R data.

1.2 Organization of this Ph.D. Thesis

This Ph.D. Thesis is essentially divided in two parts: the first part includes Chapters 2 to 4 and aims at providing the reader with the basic notions and preliminary concepts about electromagnetism and remote sensing to guarantee a full understanding of the Book even to non-expert readers. However, the reader is referred to the excellent books quoted throughout the text for more details. Due to the broad extent of these topics, the above-mentioned chapters deal exclusively with the concepts and technologies related with the research activities described in the second part of this Ph.D. Thesis, comprising Chapters 5 to 7. In particular, this Ph.D. Thesis is organized as follows.

Chapter 2 is devoted to preliminary concepts about the phenomenology of electromagnetic scattering from natural rough surfaces. Notwithstanding several scattering models have been developed and studied so far, only the scattering and surface models exploited in the second part of this Ph.D. Thesis are presented and described. In particular, the Small-Perturbation Method (SPM) and Geometrical Optics (GO) approaches are discussed assuming a fractal and normally distributed surface, respectively. These models are exploited in Chapters 5 and 6, respectively.

Chapter 3 provides a brief description of the SAR basic principles and characteristics. The radar concept is presented and the Real Aperture Radar (RAR) system to acquire Two-Dimensional (2-D) images of the surface reflectivity is briefly described to introduce the underlying principles exploited in the SAR technology to reach a superior spatial resolution. The geometric distortions typical of SAR systems are described to make the reader aware about the main difficulties in SAR imagery interpretation. The Chapter concludes with the derivation of the SAR impulse response and the related SAR image model that links the SAR focused data to the 2-D reflectivity of the sensed surface.

Chapter 4 describes the emerging remote sensing tools using Global Navigation Satellite System (GNSS) signals of opportunity. It introduces the GNSS technology for navigation services and provides a brief description of the main current GNSS constellations providing services at a global scale, namely the US GPS, the Russian GLONASS, the European Galileo, and the Chinese BeiDou-2. GNSS Radio Occultation (RO) and GNSS-R remote sensing technologies based on GNSS signals are describes as well, with a particular focus on the GNSS-R methodology and observables, namely the DDM, used further in this Ph.D. Thesis.

Chapter 5 presents two novel despeckling algorithms for SAR imagery based on the exploitation of a priori information about the scattering behavior of the illuminated surface. The proposed algorithms, named SB-PPB and SB-SARBM3D, represent a modified version of the original PPB and SARBM3D filters, in which the a priori scattering information is accounted for. The original filters are briefly described in order to let the reader understand the proposed changes, which represent the core of the Chapter. The results obtained with both simulated and actual SAR images are shown and commented as well. The Chapter concludes with an experimental sensitivity analysis aimed at a quantitative evaluation of the robustness of the proposed despeckling filters against diverse error sources.

Chapter 6 discusses a novel application of GNSS-R data in the ocean monitoring field, i.e., sea target detection. The Chapter analyzes the most diffuse remote sensing tools used for sea target detection purposes, describing their main advantages and drawbacks. GNSS-R is then demonstrated to be a valid opportunity in this field, owing to the very low revisit time that can be achieved by constellations of GNSS-R instruments. A sea target detection algorithm for spaceborne GNSS-R DDMs is then presented and described. Its effectiveness is demonstrated with actual UK TechDemoSat-1 (TDS-1) data and some relevant results are shown and commented.

Finally, Chapter 7 concludes this Ph.D. Thesis with a brief summary of the obtained results as well as some future research lines related to the presented topics.

Chapter 2

Electromagnetic Scattering: Theory and Models

Electromagnetic scattering from random rough surfaces has been subject of intensive study in the last two centuries, with the first works by J. W. Strutt Rayleigh on the light reflection and dispersion from randomly distributed particles [44]. The extremely complex phenomenology of wave-matter interaction justifies the huge efforts conducted by physicists and engineers to provide a comprehensive understanding of the EM wave scattering from random rough surfaces. The theory of EM scattering is strictly related to the Maxwell equations and its main aim is to develop methodologies and approaches to solve them. The different approaches to the problem can be categorized into analytical models, empirical models and a combination of them. Empirical models provide closed-form formulas based on measurements. These models are commonly used wherein a theoretical solution of Maxwell equations does not exist and numerical algorithms cannot be easily applied. However, they provide accurate results only in the context where they are derived. A theoretical derivation of the solution of the EM scattering problem can be addressed only in a very limited number of canonical cases, i.e., cases not physically reproducible or representing an approximation of the reality. Analytical models allow for a rigorous expression of the scattered field to be used for objective and measurable assessments, by using well-known and well-assessed mathematical tools. The hard mathematical tractability leads to nonclosed-form solutions in most of application scenarios, such as remote sensing, where the problem of modeling the EM field scattered from natural surfaces or man-made objects is of great interest. Indeed, the understanding of the relationship between the incident and scattered fields via closed-form analytical formulas allows for an easier inference about the surface parameters of interest via inversion techniques. To improve the mathematical tractability of the solution and provide a closed-form formula of the scattered field, asymptotic methods come into play. These methods are based on some restrictive hypotheses aimed at recovering the mathematical tractability of the problem and the derivation of a closed-form expression. Each asymptotic method holds under the appropriate surface roughness regime and illumination conditions and is characterized by validity limits dictated by the assumptions made. The Kirchhoff Approximation (KA), the SPM, and the Integral Equation Method (IEM) are well-known and well-assessed asymptotic methods used in the remote sensing field. The KA and the SPM represent early approaches to scattering which are still much used, whereas the IEM represents a newer approach which has a larger domain of validity. By introducing further hypotheses, the GO and Physical Optics (PO) solutions are derived from the KA. These methods have been found to be the most common in the literature and many other methods are based or have much in common with these approaches. A huge literature related to the EM scattering from random rough surface exists. The reader is referred to [45], [46], [47], [48], [49], [50], [51], [52]. In this Chapter, we focus on the scattering models used in this Ph.D. Thesis, namely the SPM and the GO. In particular, the SPM scattering model will be used to model the scattering behavior of the resolution cell in the proposed scattering-based despeckling algorithms; the GO solution will be exploited in the sea target detection algorithm to describe the forward scattering from sea surface in the GNSS-R DDM. The Chapter is organized as follows: Section 2.1 briefly introduces and describes the fundamental equations related to the EM scattering from a dielectric interface. In Section 2.2, a brief presentation of the SPM is given; in Section 2.3, the KA approach and the GO solution are described. The Normalized Radar Cross Section (NRCS) is provided as a closed-form function of the surface and EM incident field parameters for both cases.

2.1 Integral Formulation of Electromagnetic Scattering

A monochromatic, linearly polarized incident plane wave is considered. Consequently, the electric and magnetic field incident on the random rough surface can be written as follows:

$$\mathbf{E}^i(\mathbf{r}) = \hat{\mathbf{p}} E_p \exp\left(-j\mathbf{k}_i \cdot \mathbf{r}\right) = \hat{\mathbf{p}} E_p^i \tag{2.1}$$

$$\mathbf{H}^i(\mathbf{r}) = \frac{1}{\zeta} \hat{\mathbf{k}}_i \times \mathbf{E}^i(\mathbf{r}) \tag{2.2}$$

where $\mathbf{k}_i = \hat{\mathbf{k}}_i k$ is the wave vector, $\hat{\mathbf{p}}$ is the unit polarization vector, E_p is the electrical field amplitude, and $\zeta = \sqrt{\mu/\varepsilon}$ is the intrinsic impedance of the medium. We focus on surfaces with random surface profiles (i.e., not periodic surfaces) separating two regions, each one filled with homogeneous media. The geometry of the scattering problem is shown in Fig. 2.1, where a Cartesian (O, x, y, z) and a polar (O, r, ϑ, ϕ) reference systems are introduced. The $z = 0$ plane is chosen as the surface mean-plane and the

$y-$axis is chosen perpendicular to the incidence plane. Consequently, the incident EM field is uniquely described by the incidence angle ϑ_i.

It can be shown that the far zone scattered field, $\mathbf{E}^s$, can be written in terms of the tangential surface fields in the medium above the separating surface as (Stratton-Chu integral) [47]:

$$\begin{aligned}\mathbf{E}^s(\mathbf{r}) = &-\frac{jk\exp(-jkr)}{4\pi r}\left(I-\hat{\mathbf{k}}_s\hat{\mathbf{k}}_s\right)\\ &\cdot\int_S\left\{\hat{\mathbf{k}}_s\times\left[\hat{\mathbf{n}}\times\mathbf{E}(\mathbf{r}')\right]+\zeta\left[\hat{\mathbf{n}}\times\mathbf{H}(\mathbf{r}')\right]\right\}\exp\left(j\mathbf{k}_s\cdot\mathbf{r}'\right)dS' \end{aligned}\tag{2.3}$$

where $\hat{\mathbf{n}}$ stands for the unit normal vector to the surface,

$$\mathbf{k}_s = k\hat{\mathbf{k}}_s = k\left(\sin\vartheta_s\cos\phi_s\hat{\mathbf{x}}+\sin\vartheta_s\sin\phi_s\hat{\mathbf{y}}+\cos\vartheta_s\hat{\mathbf{z}}\right) = k_{sx}\hat{\mathbf{x}}+k_{sy}\hat{\mathbf{y}}+k_{sz}\hat{\mathbf{z}}\tag{2.4}$$

and the unit vector $\hat{\mathbf{k}}_s$ defines the observation direction. To compute the scattered field, the tangential surface fields in Eq. 2.3 need to be evaluated. As shown in [53], the tangential surface fields in the medium above the scattering dielectric surface can be expressed via the following integral equations:

$$\begin{aligned}\hat{\mathbf{n}}\times\mathbf{E} = {}&2\hat{\mathbf{n}}\times\mathbf{E}^i-\frac{2}{4\pi}\hat{\mathbf{n}}\\ &\times\int jk\zeta\left(\hat{\mathbf{n}}'\times\mathbf{H}'\right)G_1-\left(\hat{\mathbf{n}}'\times\mathbf{E}'\right)\times\Delta' G_1-\left(\hat{\mathbf{n}}'\cdot\mathbf{E}'\right)\Delta' G_1\,dS'\end{aligned}\tag{2.5}$$

$$\begin{aligned}\hat{\mathbf{n}}\times\mathbf{H} = {}&2\hat{\mathbf{n}}\times\mathbf{H}^i+\frac{2}{4\pi}\hat{\mathbf{n}}\\ &\times\int \frac{jk}{\zeta}\left(\hat{\mathbf{n}}'\times\mathbf{E}'\right)G_1-\left(\hat{\mathbf{n}}'\times\mathbf{H}'\right)\times\Delta' G_1-\left(\hat{\mathbf{n}}'\cdot\mathbf{H}'\right)\Delta' G_1\,dS'\end{aligned}\tag{2.6}$$

where $\hat{\mathbf{n}}'$ is the unit normal vector to the surface; $\hat{\mathbf{n}}\times\mathbf{E}$ and $\hat{\mathbf{n}}\times\mathbf{H}$ are the tangential fields on the rough surface in the medium above the separating interface; G_1 and G_2 are the Green's functions in the same medium. It is noteworthy that Eqs. 2.5 and 2.6 provide an exact expression of the tangential fields on the separating interface. By substituting Eqs. 2.5 and 2.6 in Eq. 2.3, the analytic expression of the scattered field can be derived. Once the scattered field is computed, the NRCS can be derived. The NRCS of an extended surface is defined as follows:

$$\sigma_{pq}^{0} = \frac{4\pi R_0^2 \langle |E_q^s|^2 \rangle}{A_s |E_p^i|^2} \tag{2.7}$$

where E_q^s is the q-component of the field backscattered in the far-field region by the area A_s of the surface illuminated by the plane wave in Eq. 2.1; R_0 is the distance from its center to the receiver; p and q stand for h or v (horizontal or vertical polarization).

However, the integral equations 2.5 and 2.5 cannot in general be solved analytically and an analytical solution to the general scattering problem encounters several difficulties. Therefore approximations are required to obtain closed-form analytical solutions to the scattering problem. To provide a closed-form solution to the integral equations 2.5 and 2.5 and, then, compute the NRCS, a surface model is required as well. Depending on the surface model used, different expressions of the NRCS can be derived. Analytic models used within this Ph.D. Thesis are able to handle a variety of natural surfaces: bare and moderately vegetated soils, as well as ocean surfaces. The approximated methods and surface models used within this Ph.D. Thesis are discussed in the next sections.

2.2 Small-Perturbation Method

In this Section, the SPM is briefly described. In particular, the surface model used within the SPM framework is presented in Section 2.2.1, while

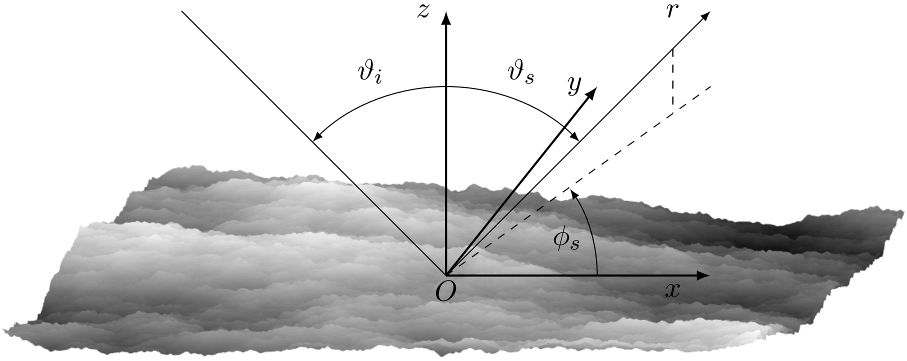

Figure 2.1. Cartesian and polar reference systems relevant to the scattering surface.

the SPM and the related NRCS are described in Section 2.2.2.

2.2.1 Surface Model

Many surface models have been presented in the scientific literature - deterministic, stochastic, empirical - each with its advantages and drawbacks. Among these, the most accepted and suitable model for natural surfaces is the fractal one. Indeed, there is an increasing experimental evidence that the fractal geometry represents the most appropriate mathematical environment to describe the shape of natural surfaces [54], [55], [56]. One of the reasons for this success is the ability of fractal models to properly account for the statistical scale-invariance properties (in particular, self-affinity) of natural surfaces. Thus, it is well known that natural surfaces show fractal behavior varying both in space and in scale. Otherwise stated, natural surfaces exhibit different roughness in different locations and at different observation scales [57], [58], [59]. Furthermore, fractal approaches provide a description of the surface with a minimum number of independent parameters [45]. In particular, we consider here a (topological) 2-D fractional Brownian motion (fBm) stochastic process $z(x, y)$ defined as follows [45]:

$$Pr\left\{z(x,y) - z(x',y') < \bar{\zeta}\right\} = \frac{1}{\sqrt{2\pi}T^{(1-H)}\tau_d^H} \int_{-\infty}^{\bar{\zeta}} \exp\left(-\frac{\zeta^2}{2T^{2(1-H)}\tau_d^{2H}}\right) d\zeta \tag{2.8}$$

where $Pr\{\}$ stands for "probability", $\bar{\zeta}$ is the considered height increment, $z(x, y)$ is the surface elevation,

$$\tau_d = \sqrt{(x - x')^2 + (y - y')^2} \tag{2.9}$$

is the distance between the two considered points of coordinates (x, y) and (x', y'), and

- H: Hurst coefficient $(0 < H < 1)$ related to the fractal dimension $D = 3 - H$;
- T: topothesy [m], i.e., the distance over which chords joining points on the surface have a surface-slope mean-square deviation equal to unity.

Fractal geometry is the mathematical abstraction of fractal physics: it exhibits properties (for instance, self-affinity) on all scales and does not allow the derivative operation at any point. Surface fractal corrugations possess power spectra that diverge in the low-frequency regime (infrared catastrophe) and exhibit non-stationary correlation functions. Usage of mathematical fractals to model natural surfaces would make any scattering computation completely intractable. However, natural surfaces are observed, sensed, measured, and represented via instruments that are, for their intrinsic nature, band-limited. In other words, no actual natural surface holds property 2.8 at any scale, and some properties of fBm mathematical surfaces may be relaxed. Accordingly, mathematical fractals may be band-limited, thus generating the physical fractals that hold most of the properties needed to manage them in the electromagnetic scattering theory. The range of scales of interest for a scattering problem is limited on one side by the finite linear size of the illuminated surface, and on the other side by the fact that surface variations on scales much smaller than the incident wavelength λ do not affect the scattered field. An efficient approach of surface modeling relies on considering surfaces that satisfy property 2.8 only in a limited range of τ_d [45]. That is why these surfaces are also referred to as band-limited fBm or physical fBm, as defined in [45].

2.2.2 Scattering Model

The second step is the choice of the electromagnetic method, i.e., the scattering model. The SPM scattering model provides a simple expression for the NRCS and shows a range of validity adequate to SAR applications. Thus, this method allows a very simple relation between fractals parameters and backscattered field.

Within the SPM approach, the NRCS of a stationary isotropic random rough surface can be expressed as follows [47]:

$$\sigma^0_{pq} = 2\pi 8 k^4 \cos^4\vartheta |\beta_{pq}|^2 W(2k\sin\vartheta) \tag{2.10}$$

where k is the wavenumber of the incident field, and β_{pq} is a function of both the complex dielectric constant ε_r of the surface and the local incidence angle ϑ [60]:

$$\begin{aligned}
\beta_{hh} &= \frac{\cos\vartheta - \sqrt{\varepsilon_r - \sin^2\vartheta}}{\cos\vartheta + \sqrt{\varepsilon_r - \sin^2\vartheta}},\\
\beta_{vv} &= (\varepsilon_r - 1)\frac{\sin^2\vartheta - \varepsilon_r(1+\sin^2\vartheta)}{\left[\varepsilon_r\cos\vartheta + \sqrt{\varepsilon_r - \sin^2\vartheta}\right]^2},\\
\beta_{hv} &= \beta_{vh} = 0,
\end{aligned} \tag{2.11}$$

$W(\kappa)$ is the spectrum of the stationary isotropic surface, defined as:

$$W(\kappa) = \frac{\sigma^2}{2\pi} \int_0^{+\infty} J_0(\kappa\tau)C(\tau)\tau \, d\tau, \tag{2.12}$$

where σ is the surface's height standard deviation, $J_0(\kappa\tau)$ is the zero-order Bessel function of the first kind, and $C(\tau)$ is the surface normalized autocorrelation function.

The power-density spectrum of the 2-D fBm exhibits an appropriate power-law behavior [45]

$$W(\kappa) = S_0 \kappa^{-\alpha_S} \tag{2.13}$$

characterized by two spectral parameters - the spectral amplitude, S_0 measured in [m^{2-2H}], and the spectral slope, α_S - that depend on the fractal parameters introduced in the space domain, namely the Hurst coefficient and topothesy:

$$\begin{aligned} S_0 &= 2^{2H+1}\Gamma^2(1+H)\sin(\pi H)T^{2(1-H)}, \\ \alpha_S &= 2+2H, \end{aligned} \tag{2.14}$$

where $\Gamma(\cdot)$ is the gamma function. Considering a monostatic radar and assuming that the surface can be described as a physical fBm, the SPM-derived NRCS is [61]

$$\sigma^0_{pq} = 2\pi 8k^4 \cos^4\vartheta |\beta_{pq}|^2 \frac{S_0}{(2k\sin\vartheta)^{(2+2H)}}. \tag{2.15}$$

2.3 Kirchhoff Approximation

In this Section, the Kirchhoff approach, also known as the tangent plane approximation, is described. It was one of the first methods applied to model the EM scattering from rough surfaces. In section 2.3.1, the

GO approximation is briefly described as one of the well-assessed methods to compute the radiation integral in Eq. 2.3 and obtain a closed-form expression of the scattered field. We will present results for the case of a surface which can be characterized as a Gaussian random process. For more details about of the Kirchhoff method, the reader is referred to [46], [47], and [50].

KA provides an estimate of the scattered field tangent to the separating interface in terms of the incident one. In particular, the scattered tangential field at any point of the surface is evaluated by locally approximating the surface with its tangent plane (for this reason, the KA is also known as *tangent plane approximation*). The total field at each point of the surface is approximated with the field that would be present on an infinitely extended plane tangent at that point on the surface. The reflection is therefore considered to be locally specular, and the local incidence angle is evaluated with reference to the local tangential plane; hence, for random rough surfaces, the tangential plane changes randomly over the surface according to the local normal $\hat{\mathbf{n}}$.

In order to apply the KA, it is required that the surface has a sufficiently large radius of curvature relative to the wavelength of the incident field in each point. Thus, under the tangent-plane approximation, the total field at a point on the surface is assumed equal to the incident field plus the field reflected by an infinite plane tangent to the surface at that point.

By applying KA, the surface integrals in Eqs. 2.5 and 2.6 are no longer necessary, since the tangential fields are evaluated with reference to the locally tangent planes and the Fresnel reflection coefficients come into play relating directly the scattered and incident fields over the plane discontinuity. A dramatic simplification of Eq. 2.3 is then provided.

To proceed further, let us introduce a *local* incident-field-polarization reference system $\left(\hat{\mathbf{h}}_l, \hat{\mathbf{v}}_l, \hat{\mathbf{k}}_i\right)$ for any surface point:

$$\begin{cases} \hat{\mathbf{h}}_l = \dfrac{\hat{\mathbf{n}} \times \hat{\mathbf{k}}_i}{|\hat{\mathbf{n}} \times \hat{\mathbf{k}}_i|}, \\ \hat{\mathbf{v}}_l = \hat{\mathbf{k}}_i \times \hat{\mathbf{h}}_l \end{cases} \tag{2.16}$$

To take advantage of the local tangent plane approximation and apply the Fresnel reflection coefficients to compute the scattered field, the EM incident field is decomposed into its perpendicular and parallel components:

$$\begin{aligned} \mathbf{E}^i &= \left[(\hat{\mathbf{p}} \cdot \hat{\mathbf{v}}_l)\hat{\mathbf{v}}_l + (\hat{\mathbf{p}} \cdot \hat{\mathbf{h}}_l)\hat{\mathbf{h}}_l\right] E_p \exp(-j\mathbf{k}_i \cdot \mathbf{r}') \\ \mathbf{H}^i &= \frac{1}{\zeta}\hat{\mathbf{k}}_i \times \mathbf{E}^i = \left[-(\hat{\mathbf{p}} \cdot \hat{\mathbf{v}}_l)\hat{\mathbf{h}}_l + (\hat{\mathbf{p}} \cdot \hat{\mathbf{h}}_l)\hat{\mathbf{v}}_l\right] \frac{E_p}{\zeta} \exp(-j\mathbf{k}_i \cdot \mathbf{r}'). \end{aligned} \tag{2.17}$$

Natural surfaces are of interest in this work; therefore, it is considered propagation in free space, and incidence on a homogeneous medium whose complex relative permittivity is ε_r and whose permeability coincides with that of the free space. In this case, the Fresnel reflection coefficients read as:

$$\begin{aligned} R_h &= \frac{\cos\vartheta - \sqrt{\varepsilon_r - \sin^2\vartheta}}{\cos\vartheta + \sqrt{\varepsilon_r - \sin^2\vartheta}}, \\ R_v &= \frac{\varepsilon_r\cos\vartheta - \sqrt{\varepsilon_r - \sin^2\vartheta}}{\varepsilon_r\cos\vartheta + \sqrt{\varepsilon_r - \sin^2\vartheta}}. \end{aligned} \tag{2.18}$$

By considering reflection over an infinite plane tangent to the surface, the tangent scattered field is proportional to the incident one via the Fresnel reflection coefficients:

$$\begin{aligned} \hat{\mathbf{n}} \times \left(\mathbf{E}^s \cdot \hat{\mathbf{h}}_l\right)\hat{\mathbf{h}}_l &= R_h\hat{\mathbf{n}} \times \left(\mathbf{E}^i \cdot \hat{\mathbf{h}}_l\right)\hat{\mathbf{h}}_l, \\ \hat{\mathbf{n}} \times \left(\mathbf{E}^s \cdot \hat{\mathbf{v}}_l\right)\hat{\mathbf{v}}_l &= R_v\hat{\mathbf{n}} \times \left(\mathbf{E}^i \cdot \hat{\mathbf{v}}_l\right)\hat{\mathbf{v}}_l. \end{aligned} \tag{2.19}$$

Hence, in the KA framework, the total tangential surface fields are [47]:

$$\begin{aligned}\hat{\mathbf{n}} \times \mathbf{E}\left(\mathbf{r}'\right) &= \hat{\mathbf{n}} \times \mathbf{E}^{i}\left(\mathbf{r}'\right) + \hat{\mathbf{n}} \times \mathbf{E}^{s}\left(\mathbf{r}'\right)\\ &= \Big[\big(\hat{\mathbf{p}} \cdot \hat{\mathbf{v}}_l\big)\big(\hat{\mathbf{n}} \times \hat{\mathbf{v}}_l\big)\big(1 + R_v\big) + \big(\hat{\mathbf{p}} \cdot \hat{\mathbf{h}}_l\big)\big(\hat{\mathbf{n}} \times \hat{\mathbf{h}}_l\big)\big(1 + R_h\big)\Big]\\ &\times E_p \exp\big(-j\mathbf{k}_i \cdot \mathbf{r}'\big),\end{aligned} \tag{2.20}$$

$$\begin{aligned}\hat{\mathbf{n}} \times \mathbf{H}\big(\mathbf{r}'\big) &= \hat{\mathbf{n}} \times \mathbf{H}^{i}\big(\mathbf{r}'\big) + \hat{\mathbf{n}} \times \mathbf{H}^{s}\big(\mathbf{r}'\big)\\ &= \Big[\big(\hat{\mathbf{p}} \cdot \hat{\mathbf{h}}_l\big)\big(\hat{\mathbf{n}} \times \hat{\mathbf{v}}_l\big)\big(1 - R_h\big) - \big(\hat{\mathbf{p}} \cdot \hat{\mathbf{v}}_l\big)\big(\hat{\mathbf{n}} \times \hat{\mathbf{h}}_l\big)\big(1 - R_v\big)\Big]\\ &\times \frac{E_p}{\zeta} \exp\left(-j\mathbf{k}_i \cdot \mathbf{r}'\right).\end{aligned} \tag{2.21}$$

In the far-field zone, the EM scattered field can be expressed as:

$$\begin{aligned}\mathbf{E}^{s}\left(\mathbf{r}\right) = -\frac{jk \exp\left(-jkr\right)}{4\pi r} E_p\big(I - \hat{\mathbf{k}_{\mathbf{s}}}\hat{\mathbf{k}_{\mathbf{s}}}\big)\\ \cdot \int_{A_s} \mathbf{F}_p\left(\alpha, \beta\right) \exp\left[-j\left(\mathbf{k}_i - \mathbf{k}_s\right) \cdot \mathbf{r}'\right] dA',\end{aligned} \tag{2.22}$$

where $\mathbf{r} = [x, y, z\left(x, y\right)]$, $A_s = XY$ is the illuminated area S projected onto the (x, y) plane, α and β stand for the surface local slopes, i.e.:

$$\begin{aligned}\alpha &\triangleq \frac{\partial z}{\partial x},\\ \beta &\triangleq \frac{\partial z}{\partial y},\end{aligned} \tag{2.23}$$

and [45]

$$\begin{aligned}\mathbf{F}_p(\alpha,\beta) =& \Big\{ (\hat{\mathbf{p}}\cdot\hat{\mathbf{v}}_l)\left[\hat{\mathbf{k}}_s\times(\hat{\mathbf{n}}\times\hat{\mathbf{v}}_l)\right](1+R_v) + (\hat{\mathbf{p}}\cdot\hat{\mathbf{h}}_l)\left[\hat{\mathbf{k}}_s\times(\hat{\mathbf{n}}\times\hat{\mathbf{h}}_l)\right] \\ &(1+R_v) + \left[(\hat{\mathbf{p}}\cdot\hat{\mathbf{h}}_l)(\hat{\mathbf{n}}\times\hat{\mathbf{v}}_l)(1-R_h)\right. \\ &\left. -(\hat{\mathbf{p}}\cdot\hat{\mathbf{v}}_l)(\hat{\mathbf{n}}\times\hat{\mathbf{h}}_l)(1-R_v)\right]\Big\}\sqrt{1+\alpha^2+\beta^2}.\end{aligned} \tag{2.24}$$

Equation 2.22 represents the scattered field formulated under the KA.

As it stands, the expression is a complicated function of the surface function and its partial derivatives. No analytic solution can be obtained from Eq. 2.22 without additional simplifying assumptions. Two approaches have been developed to proceed further at this point and provide an analytical formulation of the integral in Eq. 2.22, namely GO and PO. Both approaches assume simplifying hypothesis about the surface roughness [47]. For surfaces with a large (with respect to the wavelength) standard deviation of surface heights, an asymptotic expansion of the integral in Eq. 2.22 can be used. This is the approach followed in GO, also referred to as stationary-phase approximation, whose validity is in the so-called high-frequency regime. On the contrary, for surfaces with small slopes and a medium or small standard deviation of surface heights, a series expansion of the function $\mathbf{F}_p(\alpha,\beta)$ is used. This is the method followed in the PO.

For the surfaces of interest in this work (sea water), the GO approximation comes into play and we will focus on it, disregarding the PO approach, deeply described in the related literature [47].

2.3.1 Geometrical Optics

As stated in the previous section, the GO solution to the scattering problem comes from the KA approach with the further assumption of height variations small compared to the wavelength. In this case, the

$\mathbf{F}_p(\alpha, \beta)$ function can be assumed slowly-varying w.r.t. the phase factor $\exp\left[-j\left(\mathbf{k}_i - \mathbf{k}_s\right)\cdot\mathbf{r}'\right]$ and the integral in Eq. 2.22 can be evaluated by means of the stationary-phase approximation. Under the stationary-phase approximation the local tangent plane on a surface point can be considered infinite and, as consequence, any point of the surface re-irradiate the incident energy only in the specular direction. This means that the EM energy incident on a rough surface is scattered only along directions for which there are specular points on the surface, i.e., diffraction, shadowing and multiple scattering effects are not taken into account. The phase factor can be rephrased as follows:

$$Q \triangleq \left(\mathbf{k}_s - \mathbf{k}_i\right)\cdot\mathbf{r} = \mathbf{q}\cdot\mathbf{r} = q_x x + q_y y + q_z z, \tag{2.25}$$

where

$$\begin{aligned} q_x &= k\left(\sin\vartheta_s\cos\phi_s - \sin\vartheta_i\cos\phi_i\right), \\ q_y &= k\left(\sin\vartheta_s\sin\phi_s - \sin\vartheta_i\sin\phi_i\right), \\ q_z &= k\left(\cos\vartheta_s + \cos\vartheta_i\right) \end{aligned} \tag{2.26}$$

are the components of the scattering vector $\mathbf{q}$. In the stationary-phase approximation, only those points in which the phase is stationary - the so-called stationary-phase points - contribute to the scattering integral in Eq. 2.22. In these points, the phase factor Q exhibits null derivatives:

$$\begin{aligned} \frac{\partial Q}{\partial x} &= 0 = q_x + q_z\frac{\partial z}{\partial x}, \\ \frac{\partial Q}{\partial y} &= 0 = q_y + q_z\frac{\partial z}{\partial y}. \end{aligned} \tag{2.27}$$

As a consequence, in a stationary point, the surface local slopes read as:

$$\begin{aligned} \alpha &= -\frac{q_x}{q_z}, \\ \beta &= -\frac{q_y}{q_z}. \end{aligned} \tag{2.28}$$

Therefore, the scattered field can be expressed as:

$$\mathbf{E}^s(\mathbf{r}) = -\frac{jk\exp(-jkr)}{4\pi r}E_p\big(I-\hat{\mathbf{k}_\mathbf{s}}\hat{\mathbf{k}_\mathbf{s}}\big) \cdot \mathbf{F}_p(\alpha,\beta)\int_{A_s}\exp\left[-j(\mathbf{k}_i-\mathbf{k}_s)\cdot\mathbf{r}'\right]dA', \tag{2.29}$$

since the terms $\hat{\mathbf{n}}\times\mathbf{E}$ and $\hat{\mathbf{n}}\times\mathbf{H}$ are now constant over the integration domain. At this point, in order to evaluate the scattered field in a closed-form expression, the surface height function $z(x,y)$ has to be provided. Thus, the dependence of the scattered field upon the separating interface is in $\mathbf{r}'$ inside the integral in Eq. 2.29. However, for a random rough surface, the scattered field is a random variable at any point in the upper medium. To compute the scattering coefficient for different polarization states, the ensemble average of $|\mathbf{E}^s(\mathbf{r})|^2$ is required:

$$\langle|\mathbf{E}^s(\mathbf{r})|^2\rangle = \left|\frac{jk}{4\pi r}E_p\mathbf{F}_\mathbf{p}\right|^2\int\int\langle\exp\left[-j(\mathbf{k}_i-\mathbf{k}_s)\cdot(\mathbf{r}-\mathbf{r}')\right]\rangle\,dAdA'. \tag{2.30}$$

To proceed further, a stochastic characterization of the surface height function is needed. By assuming the surface roughness as a stationary and isotropic Gaussian random process, with zero mean, variance σ^2 , and correlation coefficient ρ, and in the assumption that the standard deviation of surface heights is large - that is, $(q_z\sigma)^2$ large -, a closed-form of the scattered power $\langle|\mathbf{E}^s(\mathbf{r})|^2\rangle$ can be derived [47]:

$$\langle|\mathbf{E}^s(\mathbf{r})|^2\rangle = \left|\frac{jk}{4\pi r}E_p\mathbf{F}_\mathbf{p}\right|^2\frac{2\pi A_s|\mathbf{q}|^2}{q_z^4\sigma^2|\rho''(0)|}\exp\left[-\frac{q_x^2+q_y^2}{2q_z^2\sigma^2|\rho''(0)|}\right] \tag{2.31}$$

where $\rho''(0)$ is the second derivatives of ρ evaluated at the origin and $\sigma^2|\rho''(0)|$ corresponds to the mean-squared slope of the surface. The scattering coefficient can then be evaluated as follows:

$$\sigma^0 = \frac{k|\mathbf{q}||U_{qp}|^2}{2q_z^4\sigma^2|\rho''(0)|}\exp\left[-\frac{q_x^2+q_y^2}{2q_z^2\sigma^2|\rho''(0)|}\right]. \tag{2.32}$$

where

$$U_{qp} = \frac{1}{E_p}\hat{\mathbf{q}}\cdot\hat{\mathbf{k}}_s\times\Big[(\hat{\mathbf{n}}\times\mathbf{E}) - \zeta\hat{\mathbf{k}}_s\times(\hat{\mathbf{n}}\times\mathbf{H})\Big]. \tag{2.33}$$

This equation represents the NRCS of a 2-D normally distributed zero-mean isotropic rough surface under the GO approach. Within this framework, a purely incoherent scattering is present due to the assumed large surface roughness. With decreasing $(q_z\sigma)^2$, a coherent component begins to appear in the scattered energy. To examine such situation, the PO approximation - not treated in this Ph.D. Thesis - needs to be explored.

Chapter 3

Synthetic Aperture Radar

In this Chapter, the fundamental principles of radar and SAR are introduced and described. The intent is to give the reader a fundamental understanding of these concepts and to identify the major issues in SAR data analysis and imagery interpretation. Numerous books dealing with SAR systems, SAR data acquisition and processing, and SAR applications exist in literature. Some excellent books are [2], [29], [62], [63], [64], [65], [66], and [67].

During its forty year history, SAR has revealed as a fundamental tool for the understanding of the Earth and other celestial bodies. As an active microwave sensor, it allows for a continuous monitoring, analysis and study of geophysical parameters and characteristics of the sensed surface in all weather conditions. From such information, electrical and structural properties of the surface (and subsurface) can be inferred via a proper data modelization and analysis. Furthermore, as discussed further in this Chapter, the peculiar SAR processing permits the retrieval of information with a spatial resolution independent from the platform altitude. Recognition of the key benefits for global monitoring of Earth's resources has led national space agencies, intergovernmental organization, and private companies to deploy a series of SAR systems in the last decades. The Canadian Space Agency launched the next-generation commercial radar satellite, named RADARSAT-2, in December 2007. The main payload is a C-band SAR with multiple polarization modes, including a fully-polarimetric mode. It was designed to offer a wide variety of applications, such as marine surveillance, environmental monitoring, disaster and resource management and mapping. COSMO-SkyMed is a four-satellite constellation supported by the Italian Space Agency and equipped with a X-band SAR. The first satellite of the COSMO-SkyMed constellation was launched on June 2007 and the constellation is fully operational since mid 2010. The TerraSAR-X mission, supported by the German Aerospace Center, was launched in June 2007 and operational since January 2008. A high-resolution X-band SAR system is mounted on board and it is capable to acquire single or dual polarization and even full polarimetric data with a revisit time of about 2 days at 95% probability to any point on Earth. The mission was completed with the launch of the second satellite, TanDEM-X, to form a twin constellation aimed at providing a high-resolution global DEM of the Earth's land surface. The very recent Sentinel mission by the European Space Agency witnesses the great interest among the European Communities in developing and supporting Earth observation missions by means of SAR remote sensing. Within the Sentinel fleet, Sentinel-1 is a constellation of two satellites orbiting 180° apart and mounting a C-band SAR built on the heritage of previous SAR systems, such as ERS-1, ERS-2 and Envisat. However, SAR imagery interpretation is a challenging task, and the analysis of SAR data is still a prerogative of SAR expert users. Indeed, as explained further in this Chapter, due to the peculiar image acquisition geometry and process, SAR images are greatly affected by geometric and radiometric distortions, and speckle noise that impair data analysis, image readability and information extraction by non-SAR expert users.

The Chapter is organized as follows: Section 3.1 introduces the fundamental concepts of the radar working principle that are needed to understand the following. Section 3.2 focuses on imaging radars, known as RAR, i.e., radar systems designed to provide a range-azimuth (or range-Doppler) image of the surface reflectivity. The chirp modulation is introduced and explained as a waveform design choice to improve the spatial resolution in the range direction. The synthetic aperture concept for the improvement of the azimuth resolution is described in Section 3.3. The SAR processing and a SAR image model are provided in the stripmap configuration. Geometric distortions and speckle are treated as well.

3.1 Basic Principles of Radar

The word *radar* identifies a well-known system whose meaning is clear to most people. However, this word is an acronym standing for RAdio Detection And Ranging and concisely describes the primary functions of such a system, i.e., target detection and target distance determination by exploiting the EM radiation-matter interaction.

A radar is an electrical system that emits radiofrequency EM waves toward a region of interest and receives the EM energy reflected from objects possibly present in that region. The physical phenomenon exploited to detect targets in the region of interest is the reflection of EM waves at an impedance discontinuity due for instance to the presence of an object in that region. The working principle of a radar system is shown in Fig. 3.1. The signal transmitted by the radar antenna propagates through the environment surrounding the radar system to the target. The EM wave incident on the target induces electrical currents on it and reradiates EM energy into the environment. Similarly, many other reflections come from other surfaces on the ground and in the atmosphere and contribute to the so-called *clutter*. A portion of the reflected signal propagates back to the radar and is captured by the receiver antenna. The received echo is processed by the radar receiver that has to reveal the target, if present.

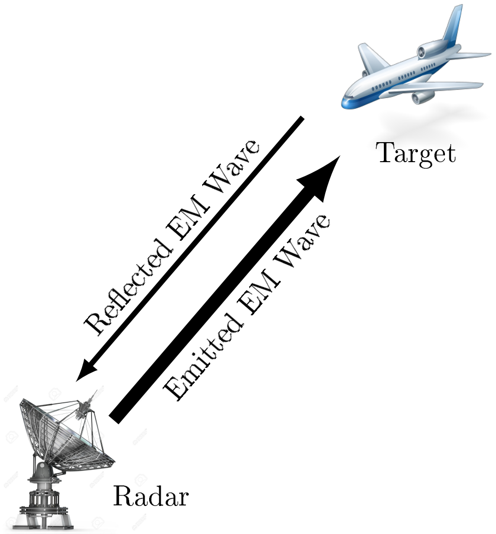

Figure 3.1. Working principle of a radar system. The EM wave emitted from the radar antenna propagates into the surrounding medium, is reflected from the target, and comes back to the receiver.

The range, R, to a detected target can be computed by measuring the time, ΔT, it takes the EM wave to propagate to that target and back at the speed of light. Since the distance the EM wave has to travel to the target and back to the radar is $2R$,

$$R = \frac{c\Delta T}{2}, \tag{3.1}$$

where c is the speed of light ($c \approx 3 \times 10^8$ m/s). The target echo co-exists with other signal sources - such as EM interference, intentional countermeasures (jamming), echoes from the environment (clutter) and thermal noise - that affect detectability of the target. The received echo is a coherent summation of all these contributions.

Radar systems have evolved tremendously since their early days when their functions were limited to target detection and ranging. Indeed, modern radars are sophisticated computer systems that, besides the abovementioned functions, allow for target tracking, identification, imaging, and classification while contrasting strong unwanted echoes such as clutter and jamming. Consequently, the range of application of such modern systems is wide as the traditional military and civilian tracking of aircraft and vehicles to 2-D and Three-Dimensional (3-D) imaging, collision avoidance, Earth resources monitoring, and many others. In the next sections, a deep insight into imaging radars is provided.

3.2 Real Aperture Radar

An imaging radar is a radar system whose primary function is to provide a 2-D or 3-D image of the underlying surface (and subsurface). The radar is typically mounted on a moving platform, such as an aircraft or spacecraft. The image characteristics depend on the radar operating frequency, due the dependence of the penetration depth δ in the medium on the transmitted EM wave frequency as follows:

$$\delta = \frac{1}{\sqrt{\mu f \pi \sigma_c}}, \tag{3.2}$$

where f is the radar operating frequency, μ and σ_c are the magnetic permeability, and the electrical conductivity of the medium, respectively. From Eq. 3.2, the penetration depth of the EM incident wave is a decreasing function of its frequency.

Imaging sensors can be classified as *active* and *passive* systems: the former make use of a transmitter module to provide an image of the sensed surface at the desired frequency and measure the energy reflected from the surface; the latter detect the radiation naturally emitted or reflected from the surface. For passive systems, such as radiometers and imaging cameras, Sun is the primary energy source for the reflected energy, thus limiting the imaging capabilities of the Sun-reflected radiation at daytime. Passive sensors usually operate at very high frequencies and measure natural surface emissions in the visible, infrared and thermal regions of the EM spectrum. Clouds, fog and rain can limit the applicability of passive sensors as well. On the other hand, active systems, such as scatterometers, altimeters, SAR, operate at lower frequencies, between approximately 1 and 30 GHz [68], and provide light- and weather-independent imaging capabilities - a fundamental prerequisite for a global and continuous monitoring - due to the presence of a specific illumination source, that makes active systems typically more complex and power-hungry compared to passive sensors. Imaging active systems are mostly implemented as radar systems operating at microwaves [69], i.e., in the portion of EM spectrum from 300 MHz to 300 GHz [29]. They are usually referred to as RAR [29].

The *spatial resolution*, defined as the minimum distance at which two different objects are detected by the system as separated, is one of the most important parameters characterizing an imaging system, and impacts the image interpretation capability as well as the accuracy and resolution of information retrieval procedures. In the field of remote sensing imaging, spatial resolution is typically split in two terms: range resolution, or across-track resolution, and azimuth resolution, or along-track resolution. Assuming a radar transmitting an ideal rectangular pulse of duration τ, the Rayleigh range resolution Δr reads as:

$$\Delta r = \frac{c\tau}{2}. \tag{3.3}$$

From Eq. 3.3, the shorter the transmitted pulse, the better the range resolution. Very short pulse durations ($\tau \approx 10^{-8} \div 10^{-7}$ s) are needed to reach a resolution on the order of magnitude of meters. However, reducing the pulse duration to improve the range resolution is not always advisable, since it greatly affects the Signal-to-Noise Ratio (SNR) also, and then the detectability of the target. As a consequence, an higher power peak is needed for shorter pulses to keep a constant SNR value.

A possible alternative to improve the range resolution is via a proper waveform design of the transmitted pulse. To this aim, Eq. 3.3 can be rewritten as:

$$\Delta r = \frac{c}{2\Delta f}, \tag{3.4}$$

where the pulse bandwidth $\Delta f \approx 1/\tau$ for an ideal rectangular pulse. A way to improve the range resolution without reducing the pulse duration is to increase the pulse bandwidth via a proper modulation scheme. A typical waveform implemented in the field of radar imaging is the *chirp* pulse, defined as follows:

$$f_1(t) = \exp\left[j\left(\omega t + \frac{\alpha_c t^2}{2}\right)\right]\text{rect}\left[\frac{t}{\tau}\right], \tag{3.5}$$

where $\omega = 2\pi f$ is the angular frequency, $\text{rect}[t/\tau]$ is a rectangular pulse of duration τ, and α_c is the chirp rate related to the pulse bandwidth:

$$\Delta f \approx \frac{\alpha_c \tau}{2\pi}. \tag{3.6}$$

By substituting Eq. 3.6 in Eq. 3.4, the range resolution can be linked to the chirp rate as follows:

$$\Delta r \approx \frac{\pi c}{\alpha_c \tau} \tag{3.7}$$

Equation 3.7 represents the range resolution of an imaging radar implementing the chirp pulse concept. Assuming a pulse duration of 1 μs, a chirp rate $\alpha_c = 10^{15}$ (corresponding to a bandwidth $\Delta f \approx 160$ MHz) is required for a range resolution of 1 m.

While the range resolution depends on the signal characteristics, namely the signal bandwidth, the azimuth resolution is strictly related to the antenna system. Indeed, the azimuth extension of the resolution cell, i.e., the azimuth resolution, is the antenna footprint X, defined as the surface portion illuminated by the antenna pattern. Therefore, for a side-looking RAR (see Fig. 3.2), the azimuth resolution Δx is:

$$\Delta x \equiv X \cong R\Delta\vartheta = \frac{h}{\cos\vartheta_0}\Delta\vartheta, \tag{3.8}$$

where R is the slant range of the scene center, $\Delta\vartheta$ is the antenna beamwidth in the azimuth direction, h is the platform altitude, and ϑ_0 is the radar look angle. Assuming a 2° antenna beamwidth operating at an altitude of 800 km with a radar look angle of 30°, an azimuth resolution of more than 30 km is obtained. To improve the azimuth resolution, a longer antenna in the along-track direction is required. However, microwave spaceborne radars would require antenna dimensions between several hundred meters to some kilometers to achieve azimuth resolution on the order of magnitude of meters [29]. Indeed, the azimuth resolution is the main limitation of RAR systems in the field of microwave radar imaging. To achieve a better resolution with feasible antenna sizes, the synthetic aperture concept comes into play.

3.3 Synthetic Aperture Radar

A SAR is a coherent radar imaging system based on the synthetic aperture or synthetic antenna concept, first conceived by Wiley [70]. Within this approach, a very long antenna is synthesized by moving a shorter one along a convenient path, usually the flight path. The recorded received echoes undergo a proper processing in which both the phase and amplitude of the echo samples must be used to simulate the long antenna. This data processing, typically performed digitally, is an essential step in the SAR data acquisition and image formation processes and allows for

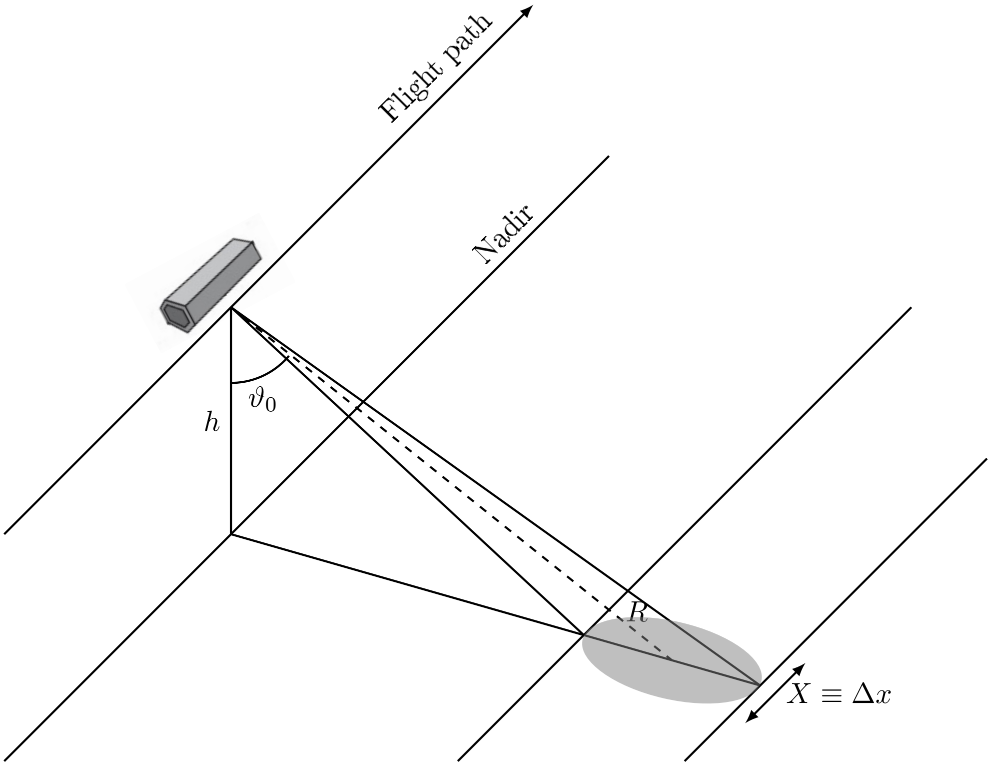

Figure 3.2. Side-looking viewing geometry of an imaging radar system.

a dramatic improvement of the along-track resolution up to meters, thus making the SAR a fundamental tool in the observation and monitoring of the Earth's [71] and other planets' [72] surface.

A SAR system can operate in three operating modes: strimap, spotlight and scanSAR. In the most common stripmap configuration, the antenna beam is kept at a fixed angle with respect to the flight direction and the antenna footprint covers a strip on the sensed surface as the system moves. A stripmap image is then limited in the range direction and unlimited in the azimuth one. The spotlight mode allows for a significant increase of the azimuth resolution. In this configuration, the antenna beam is steered along the platform path to cover a limited area on the ground. The better azimuth resolution is due to the longer synthetic aperture allowed by the radar antenna steering and is traded off by a limited image in the along-track direction. Finally, the scanSAR mode allows for an extension of the acquired image in the across-track direction. In this configuration, the synthetic aperture is divided in orthogonal sub-apertures, each one pointed at a different look angle. The system switches cyclically the beam among the different angles, thus covering a larger area w.r.t. the stripmap mode. However, the shorter synthetic aperture causes a loss in the azimuth resolution. To avoid range-doppler ambiguities, a shared characteristic of the above-mentioned operating modes is the side-looking viewing geometry, in which the radar antenna is aimed to the left or right of the flight path and typically perpendicular to the flight direction.

In the following Section, we focus on the derivation of the transfer function and image model in the standard stripmap mode.

3.3.1 Stripmap Transfer Function

The SAR stripmap transfer function is derived assuming the basic geometry configuration shown in Fig. 3.2, where the cylindrical coordinates (x, r, θ) are referred to as *azimuth*, *slant range* (o simply *range*) and *look* *angle*, respectively. The x-axis is chosen coincident with the platform trajectory, assumed as a straight line, and oriented as the velocity vector. The r-axis points toward the Earth and is aligned with the radar antenna; r stands even for the minimum distance between the sensor and the target. Finally, θ is the polar angle in the plane orthogonal to the x-axis and containing the r-axis.

Range

In the assumed cylindrical coordinate system, the chirp signal f_1 (see 3.5) reflected from a target $T \equiv (0, r, \theta)$ and received on board is given by:

$$f_1\left(t - \frac{2r}{c}\right) = \exp\left[j\omega\left(t - \frac{2r}{c}\right) + j\frac{\alpha_c}{2}\left(t - \frac{2r}{c}\right)^2\right] \mathrm{rect}\left[\frac{t - 2r/c}{\tau}\right]. \quad (3.9)$$

After the heterodyne operation and the following formal change of variables:

$$\begin{aligned} r &\rightarrow \frac{r}{c\tau/2} \\ r' &\rightarrow \frac{ct/2}{c\tau/2}, \end{aligned} \quad (3.10)$$

the received signal is:

$$f(r') = \exp\left[-j\omega\tau r + j\frac{\alpha_c \tau^2}{2}(r' - r)^2\right] \mathrm{rect}[r' - r]. \quad (3.11)$$

The matched filter used to further process the signal $f(r')$ is defined as follows:

$$g(r') \triangleq \exp\left[-j\frac{\alpha_c \tau^2}{2} r'^2\right] \mathrm{rect}[r']. \quad (3.12)$$

Then, the received signal $f(r')$ undergoes a convolution with the filter $g(r')$. The output signal is:

$$\hat{f}(r') = f \otimes g(r') = \exp(-j\omega\tau r) \int \exp\left[j\frac{\alpha_c\tau^2}{2}(r' - r - u)\right] \exp\left[-j\frac{\alpha_c\tau^2}{2}u^2\right] \cdot \mathrm{rect}[r' - r - u]\,\mathrm{rect}[u]\,du. \quad (3.13)$$

The convolution in Eq. 3.13, even if usually implemented via fast Fourier transform (FFT) codes, can be analytically computed as shown in [29]. After some manipulations and assuming $|r' - r| \ll 1$, the signal $\hat{f}(r')$ can be written as follows:

$$\hat{f}(r') = \exp(-j\omega\tau r)\,\mathrm{sinc}\left[\alpha_c\tau^2\frac{r' - r}{2}\right] = \exp(-j\omega\tau r)\,\mathrm{sinc}\left[\frac{\pi}{\Delta r}(r' - r)\right], \quad (3.14)$$

where

$$\Delta r = \frac{1}{\tau\Delta f} \quad (3.15)$$

is the 3 decibel (dB) range resolution, i.e., the 3 dB width of the point target response, the so-called Point Spread Function (PSF).

In non-normalized units the spread function reads as:

$$\hat{f}(r') = \exp\left(-j\frac{4\pi}{\lambda}r\right)\mathrm{sinc}\left[\frac{\pi}{\Delta r}(r' - r)\right], \quad (3.16)$$

where

$$\Delta r = \frac{c}{2\Delta f}. \quad (3.17)$$

The range resolution in Eq. 3.17 represents the minimum distance between two point targets of *equal* spread function amplitude that are detected as separate entities. Consequently, Eq. 3.17 is usually referred to as the *nominal* range resolution and it does not adequately describe the actual range resolution when one target dominates.

In presence of a continuous distribution of scatterers, the processed echo can be written as a superposition of PSFs, each one weighted by the *reflectivity pattern* $\gamma(r)$ proportional to the ratio between the backscattered and incident field and related to the Radar Cross Section (RCS) of the target. In this case, Eq. 3.14 becomes:

$$\hat{\gamma}(r') = \int \gamma(r)\hat{f}(r'-r)\,dr = \int \gamma(r)\exp(-j\omega\tau r)\,\text{sinc}\left[\frac{\pi}{\Delta r}(r'-r)\right]dr. \tag{3.18}$$

Azimuth

For a RAR, the ability to resolve targets in the azimuth direction is strictly related to the radar antenna beamwidth. Thus, two separated targets can be resolved only if they are not present in the antenna beamwidth simultaneously. Consequently, the azimuth resolution is equal to the antenna footprint and it is given by:

$$\Delta x \approx r\frac{\lambda}{L_a} \tag{3.19}$$

where r is the slant range of the target, λ is the radar EM wavelength and L_a is the *effective* antenna length in the azimuth direction. The obtained resolution is on the order of magnitude of kilometers and does not match most imaging applications requirements. To overcome this limitation, the SAR concept comes into play. The synthesis is addressed by coherently combining the received echoes recorded along the flight path.

Let us suppose the radar transmitting pulses at equally spaced positions $S_n \equiv (x' = n'd, r = 0)$ toward a point target located at $T \equiv (0, r, \theta)$, where d is the distance covered by the platform between two consecutive pulses.

The radar antenna footprint X identifies the number of echoes received by the target as a function of the Pulse Repetition Frequency (PRF) and the platform velocity. Assuming the point target illuminated by $2N+1$ pulses and an isotropic antenna within its beamwidth, the signal reflected from the target and received by the antenna can be written as (after the heterodyne process):

$$f(n'd) = \exp\left(-j\omega\frac{2R}{c}\right) \approx \exp\left[-jw\frac{2r}{c} - j\frac{2\pi}{\lambda r}(n'd)^2\right] \tag{3.20}$$

where $n' = -N, ..., N$, and

$$R = \sqrt{r^2 + (n'd)^2} \approx r + \frac{(n'd)^2}{2r} \tag{3.21}$$

is the sensor-target distance. By introducing the following azimuth reference function:

$$g(n'd) \triangleq \exp\left[j\frac{2\pi}{\lambda r}(n'd)^2\right], \quad n' = -N, ..., N, \tag{3.22}$$

the synthetic aperture processing is addressed as the convolution of the $2N+1$ echoes (recorded on board) received by the radar antenna and the azimuth reference function:

$$\hat{f}(n'd) = \sum_{k=n'-N}^{N} \exp\left[-j\frac{2\pi d^2}{\lambda r}k^2\right] \exp\left[+j\frac{2\pi d^2}{\lambda r}(n'-k)^2\right]. \tag{3.23}$$

As for the range case, the convolution in Eq. 3.23 can be treated analytically and leads to [29]

$$\hat{f}(x') \approx \frac{\sin\left(\dfrac{2\pi X}{L_a}x'\right)}{\dfrac{X}{d}\sin\left(\dfrac{2\pi d}{L_a}x'\right)} \tag{3.24}$$

where $x' = n'd/X$ is the normalized discrete azimuth abscissa of the sensor and the amplitude factor $2N = X/d$ is ignored. Equation 3.24 represents the azimuth counterpart of Eq. 3.14 and describes the power spreading of the target response (i.e., the PSF) in the azimuth direction. Close to the target, i.e., for $x \approx 0$, the PSF exhibits a *sinc* pattern in the azimuth direction as well:

$$\hat{f}(x') \approx \mathrm{sinc}\left(\frac{2\pi X}{L_a}x'\right) = \mathrm{sinc}\left(\frac{\pi}{\Delta x}x'\right) \tag{3.25}$$

where

$$\Delta x = \frac{L_a}{2X} \tag{3.26}$$

is the 3 dB normalized resolution in the azimuth direction. In nonnormalized units:

$$\Delta x = \frac{L_a}{2} \tag{3.27}$$

It is noteworthy that: 1) the azimuth resolution does not depend on the platform height. This is due to the fact that the higher the platform altitude, the longer the synthetic antenna, and then the larger the number of acquired target echoes. 2) the smaller the antenna, the better the resolution. This surprising result is explained by the longer antenna footprint and synthetic antenna with a smaller real antenna.

Similarly to the range processing, the processed signal in the case of distributed targets can be modeled as follows:

$$\hat{\gamma}(n'd) = \int \gamma(x)\hat{f}(n'd - x)\,dx = \int \gamma(x)\,\mathrm{sinc}\left[\frac{\pi}{\Delta x}(n'd - x)\right]dx. \tag{3.28}$$

A continuous version $\hat{\gamma}(x')$ of the signal $\hat{\gamma}(n'd)$ in Eq. 3.28 can be reconstructed via sampling interpolation, since its bandwidth is limited by the sinc function and equals $1/\Delta x$:

$$\hat{\gamma}(x') = \sum \hat{\gamma}(n'd)\,\mathrm{sinc}\left[\frac{\pi}{\Delta x}(x - n'd)\right] = \int \gamma(x)\,\mathrm{sinc}\left[\frac{\pi}{\Delta x}(x' - x)\right] dx. \tag{3.29}$$

Finally, the overall SAR image model can be obtained by combining Eqs. 3.18 and 3.29:

$$\hat{\gamma}(x', r') = \int\int \gamma(x, r)\,\mathrm{sinc}\left[\frac{\pi}{\Delta x}(x' - x)\right]\mathrm{sinc}\left[\frac{\pi}{\Delta r}(r' - r)\right] dx dr, \tag{3.30}$$

where $\gamma(\cdot,\cdot)$ stands for the 2-D reflectivity pattern of the illuminated scene also including the phase factor $\exp(-j\omega\tau r)$ of Eq. 3.18.

3.3.2 Geometric Distortions

At first glance, a SAR image may seem to closely resemble an optical image. Closer inspection, however, reveals striking differences which can be used, given knowledge of how radar interacts with ground features, to provide a wide spectrum of information about the targets. The most obvious difference from an optical image is the geometric distortion produced by the radar look angle and the height or slope of the target. Thus, the most striking feature in SAR images is the peculiar geometry in range direction. This effect is caused by the SAR imaging principle: measuring signal travel time and not angles as optical systems do. The time delay between the radar echoes received from two different points determines their distance in the image. In other words, the slant-range distortion occurs because the radar is measuring the distance to features in slant-range rather than the true horizontal distance along the ground. This results in a varying image scale, moving from near to far range. The presence of geometric distortions, also referred to as *slant-range distortions* intrinsic to the *range* imaging mode limits use of SAR images computed in the natural coordinates (i.e., *slant* range and azimuth) in many applications (i.e., geology studies, glaciology, land resource analysis, etc.) [73].

To clarify this point let us consider the SAR geometry in the plane orthogonal to the azimuth direction, with the antenna pointing to one side of the flight track as usual (see Fig. 3.3).

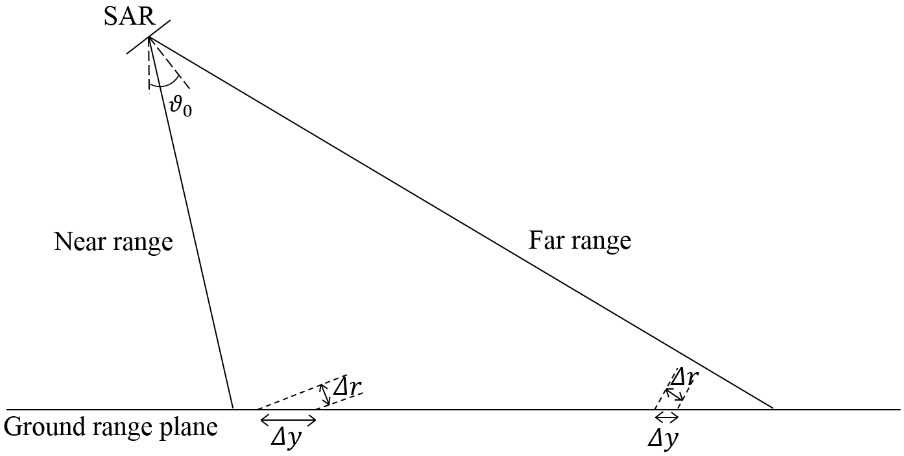

Figure 3.3. SAR geometry.

It is evident that a constant resolution Δr in the slant range direction does not correspond to a similarly constant resolution, Δy, on the ground range. In particular, we have for the geometry of Fig. 3.3:

$$\Delta y = \frac{\Delta r}{\sin \vartheta} \tag{3.31}$$

where the variation of the local incidence angle ϑ from near to far range leads to a decrease of the ground range resolution Δy.

Let us relax the planarity assumption and consider the effect of a surface slope α in the range direction. In this case, the resolution on the ground depends on the local incidence angle $\vartheta = \vartheta_0 - \alpha$. Foreshortening, layover and shadowing represent the geometric distortions typical of SAR images and depend on local slope of the surface. Each of these effects corresponds to a different relationship between the surface slope α, and the radar look angle ϑ_0.

Foreshortening

Foreshortening is present when $-\vartheta_0 < \alpha < \vartheta_0$ and corresponds to a dilation or compression of the resolution cell on the ground with respect to the planar case of Fig. 3.3, depending on the conditions $0 < \alpha < \vartheta_0$ or $-\vartheta_0 < \alpha < 0$, respectively. Foreshortening occurs when the radar beam reaches the base of a tall feature tilted towards the radar (e.g. a mountain) before it reaches the top (Fig. 3.4). Because the radar measures distance in slant-range, the slope (from point A to point B) will appear compressed and the length of the slope will be represented incorrectly (A' to B') at the image plane. Points A, B and C are equally spaced when vertically projected on the ground (as it is done in conventional cartography). However, the distance between A' and B' is considerably shortened as compared to B' - C', because the top of the mountain is relatively close to the SAR sensor.

Foreshortening is a dominant effect in SAR images of mountainous areas. Especially in the case of steep-looking spaceborne sensors, the across-track slant-range differences between two points located on foreslopes of mountains are smaller than they would be in flat areas. This effect results in an across-track compression of the radiometric information backscattered from foreslope areas which may be compensated during the geocoding process if a DEM of the surface is available. Foreshortening is obvious in mountaineous areas, where the mountains seem to “lean” towards the sensor (see Fig. 3.5). It is worth noting that shortening effects are still present on ellipsoid corrected data and in presence of very small slopes as well.

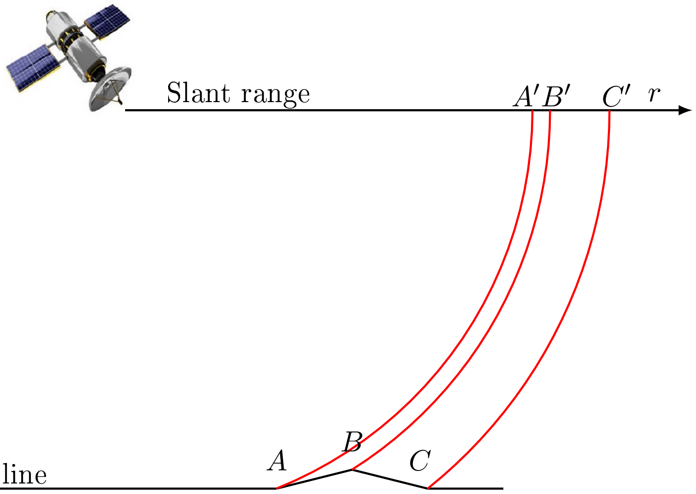

Figure 3.4. Foreshortening compression and dilatation effect. Foreslope cells are compressed; backslope cells are dilated.

Layover

Layover occurs when the local range-slope of the surface is larger than the radar look angle, i.e., when $\alpha > \vartheta_0$. In this case, the echo signal coming from the top of the mountain reaches the radar receiver before the signal reflected from the basis (see Fig. 3.6). Therefore, layover consists of an *inversion* between the top and bottom of the valley. In other words, the ordering of surface elements on the radar image is the reverse of the ordering on the ground: peaks of hill or mountains with a steep slope commute with their bases in the slant range, thus causing an extremely severe image distortion. A particular case is represented by the situation $\alpha = \vartheta_0$ corresponding to the compression of the area with this slope into a single pixel.

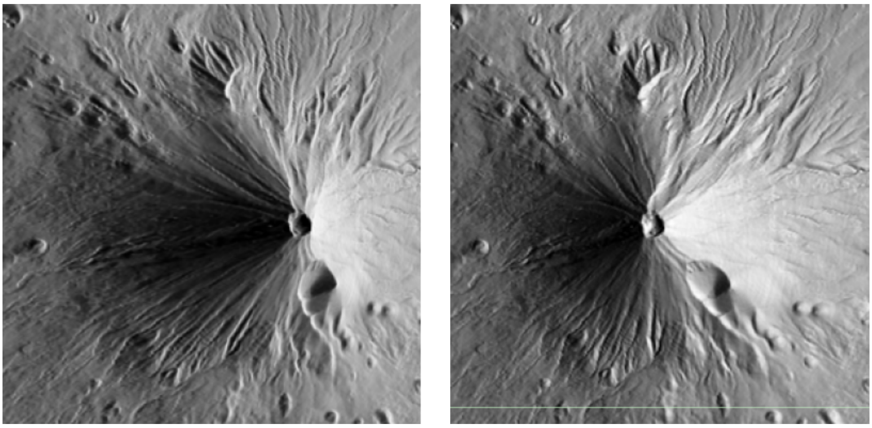

(a) *Foreshortened image* **(b)** *Non foreshortened image (Ortho-image)*

Figure 3.5. Foreshortening effect on SAR images

Generally, layover zones appear as bright features on the image due to the low incidence angle since they face radar illumination. Ambiguity occurs between targets in the valley and in the foreland of the mountain, in case they have the same slant-range distance. For steep incidence angles this might also include targets on the backslope. An image is affected by layover only if very high slopes are present or if the radar look angle is sufficiently small.

Geocoding cannot resolve the ambiguities due to the representation of several points on the ground by one single point on the image; these zones also appear bright on the geocoded image.

Figure 3.7 shows two SAR images acquired over a mountainous zone close to Udine (Italy) by ERS-1 and Landsat-5, respectively. The effect of layover is visible in the whole SAR image, in particular on the two mountains that are on the right of the lake. The height of the upper one (Mt. San Simeone) is about 1000 m above the valley bottom (1220 m), while the height of the lower one (Mt. Brancot) is 1015 m.

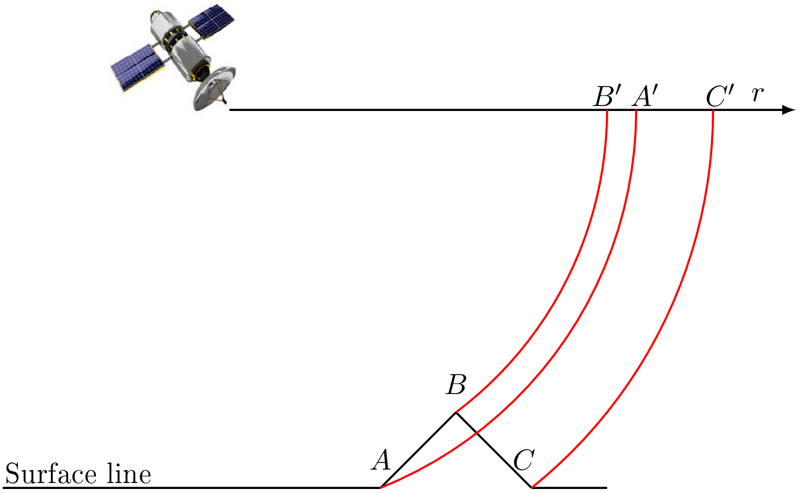

Figure 3.6. Layover effect.

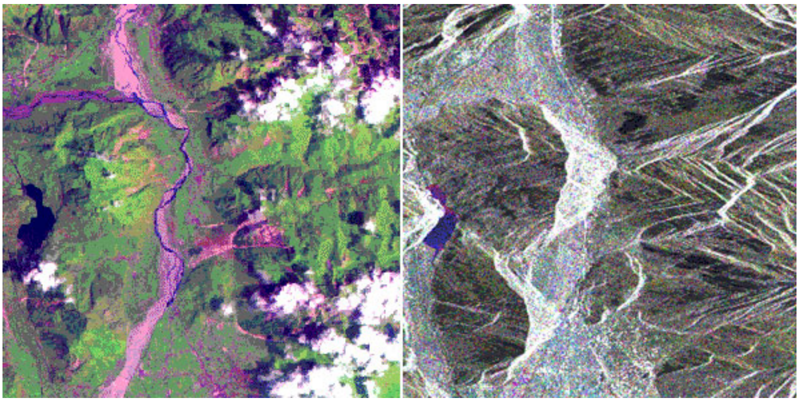

Figure 3.7. Layover effect. Inversion between the top and bottom of the valley is clearly visible.

Shadowing

Shadowing occurs when $\alpha \leq \vartheta_0 - \pi/2$. This is a necessary condition for appearance of shadow, whose effect can extend over other areas with no constraint on the slope. In this case, the region does not produce any backscattered signal, and no significant contribution to the image is generated by these areas (Fig. 3.8).

A slope away from the radar illumination with an angle that is steeper than the sensor depression angle provokes radar shadows. It should be also noted that the radar shadows of two objects of the same height are longer in the far range than in the near range.

Shadow regions appear as dark (zero signal) with any changes due solely to system noise, sidelobes, and other effects normally of small importance.

The multitemporal (Sep. 13-19-25, 1991) SAR image depicted in Fig. 3.9 (right) has been acquired over the Cote D'Azur area (France). The Gran Canon du Verdon visible in the central part of the image has a very steep gorge that descends swiftly to the valley bottom, causing radar shadow. This is shown by the dark zones in the central part of the image. A map of the area is depicted in Fig. 3.9 (left).

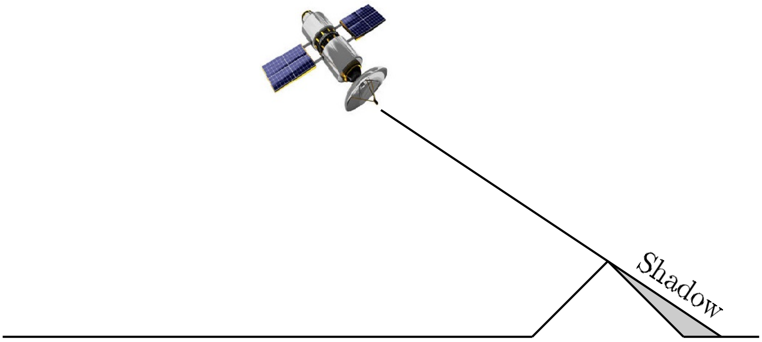

Figure 3.8. Shadowing effect. Dark regions are not illuminated and the shadow extends over other areas.

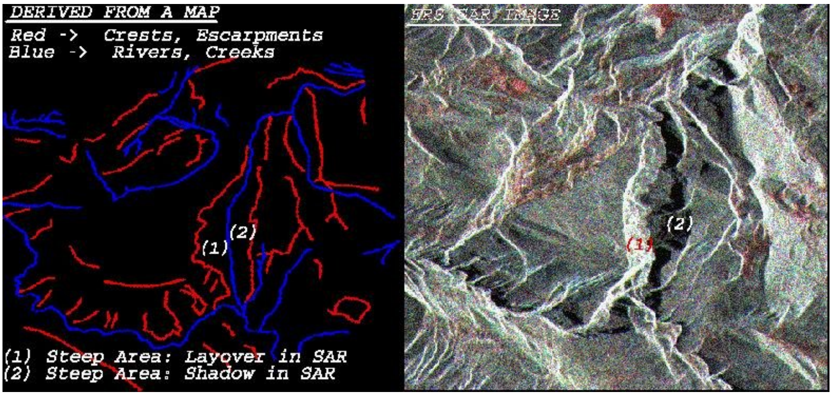

Figure 3.9. Shadowing effect on a real SAR image of the Gran Canon du Verdon, Cote D'Azur (France).

3.3.3 SAR Signal Statistics

Due to the complex mechanisms at the basis of the EM radiation/matter interaction and, then, SAR image formation, SAR data cannot be modeled exclusively in a deterministic framework and randomness of the received signal has to be accounted for. Indeed, the signal scattered from the illuminated surface depends upon numerous geometrical and electromagnetic parameters of the sensed surface, such as relative dielectric constant, electrical conductivity, local incidence angle (i.e., macroscopic roughness), and microscopic roughness. As a matter of fact, while knowledge of the electromagnetic characteristics of the surface can be easily addressed for instance by knowing the surface type, the roughness of the scene can only be described in a statistical framework, thus causing SAR data to be a random process. A SAR resolution cell is typically large compared with the wavelength of the incident EM field. Since the operating frequency is typically on the order of GHz, this characteristic applies even to the recent very high-resolution SAR sensors, such as TerraSAR-X and COSMO-SkyMed, whose spatial resolution is up to 1 m in the spotlight mode. Furthermore, roughness and inhomogeneities of the surface cause the presence of a large number of scatterers within the resolution cell. The phase of each single term is related to the sensor-scatterer distance normalized to the radar wavelength and, therefore, large variations of the phase of the contributions are due to the large resolution cell w.r.t. the wavelength of the incident field. The received signal is the coherent superposition of the contributions from the single scatterers within the resolution cell and, consequently, experiences large fluctuations - the so-called *fading* - due to the large variations of the phase of each single term. The coherent SAR image acquisition processing makes fading appear as grainy noise: the so-called *speckle*. Speckle can then be interpreted as an interference phenomenon between the different contributions within the resolution cell, in which the main source of the noise-like behavior of the observed data is the distribution of the phase terms.

Assuming that no dominant scatterer is present within the resolution cell and that all the scatterers are statistically independent, the received signal reads as:

$$V_1 + jV_2 = \sum_{i=1}^{N} V_i \exp(j\phi_i) = \sum_{i=1}^{N} V_i \cos\phi_i + j \sum_{i=1}^{N} V_i \sin\phi_i \tag{3.32}$$

where N stands for the number of scatterers within the resolution cell, V_1 and V_2 represent the real and imaginary parts of the received echo, and V_i and ϕ_i are the amplitude and phase of the contribution of the $i-$th scatterer. Since the resolution cell is large compared to the radar wavelength, N is large and V_1 and V_2 can be assumed zero-mean normally distributed as a consequence of the central limit theorem. Accordingly, the probability density function (pdf) of V_1 and V_2 are:

$$\begin{aligned} p(V_1) &= \frac{1}{\sqrt{2\pi\sigma_V^2}} \exp\left(-\frac{V_1^2}{2\sigma_V^2}\right) \\ p(V_2) &= \frac{1}{\sqrt{2\pi\sigma_V^2}} \exp\left(-\frac{V_2^2}{2\sigma_V^2}\right), \end{aligned} \tag{3.33}$$

with variance σ_V^2 [47]. Let us assume V_1 and V_2 to be uncorrelated, i.e., $E[V_1V_2] = E[V_1]E[V_2] = 0$, and, then, independent, being normally distributed. Consequently, the joint pdf is given by:

$$p(V_1, V_2) = \frac{1}{2\pi\sigma_V^2} \exp\left(-\frac{V_1^2 + V_2^2}{2\sigma_V^2}\right) \tag{3.34}$$

In polar coordinates, we get [29]:

$$p(V, \phi) = \frac{V}{2\pi\sigma_V^2} \exp\left[-\frac{V^2}{2\sigma_V^2}\right] \tag{3.35}$$

where $V = \sqrt{V_1^2 + V_2^2}$ is the amplitude of returned echo. By integrating Eq. 3.35 over V and ϕ, we get the following pdfs for the phase and amplitude of the received signal, respectively:

$$p(\phi) = \int_0^{+\infty} p(V, \phi)\, dV = \frac{1}{2\pi}, \phi \in [0, 2\pi] \tag{3.36}$$

$$p(V) = \int_0^{2\pi} p(V, \phi)\, d\phi = \frac{V}{\sigma_V^2} \exp\left(-\frac{V^2}{2\sigma_V^2}\right), V \geq 0 \tag{3.37}$$

As a result, the amplitude of the signal is Rayleigh distributed in $(0, +\infty)$ and the phase is uniformly distributed in $(0, 2\pi)$. The signal power is $W = V^2$ and, therefore, exponentially distributed:

$$p(W) = \frac{1}{2\sigma_V^2} \exp\left(-\frac{W}{2\sigma_V^2}\right) \tag{3.38}$$

The Rayleigh and exponential distributions are of key importance in handling SAR data and are completely characterized by a single parameter, namely σ_V, carrying all the information about the scene. No information is carried out by phase signal, whose distribution is independent from the illuminated scene. Phase becomes relevant when dealing with interferometric and polarimetric SAR data or when high-performance imaging of deterministic (man-made) targets is of interest [2]. However, this simple model is adequate for homogeneous SAR data, i.e., SAR images acquired over a scene characterized by homogeneous parameters. In this case, the hypothesis about the absence of a dominant scatterer is valid and then V_1 and V_2 can be properly modeled as normal random variables. Indeed, the consistency of this speckle model with observed data is supported by numerous studies [74], [75]. However, this statistical description of SAR data is adequate in a very limited number of cases or specific applications, such as agricultural fields, untextured regions, low-resolution sea clutter. In most cases, the illuminated scene exhibits significant inhomogeneities and more involved statistical models are required. Typical models used to describe both SAR image amplitude and intensity (i.e., amplitude squared) of realistic scenarios are the K, Weibull, and log-normal distributions. These pdfs are characterized by two degrees of freedom, and, therefore, are more powerful in fitting real SAR data of inhomogeneous scenes. Their success in statistical modeling of even very high-resolution SAR data is related to the good compromise between law complexity and fitting capabilities they can offer. The log-normal distribution has been successfully applied to model high-resolution data [76], [77], [78], and land clutter over built-up areas [79], [80]. The works in [81], [82], [83] demonstrate the capability of the Weibull distribution to fit a wide range of ocean measurements at different resolutions. The Weibull distribution has also been applied to model sea-ice [84], weather [85] and land [81], [86], [87] clutter.

The log-normal distribution is given by:

$$p(x) = \frac{1}{x\sqrt{2\pi\sigma_x^2}} \exp\left[-\frac{(\log x - \nu_x)^2}{2\sigma_x^2}\right] \tag{3.39}$$

where ν_x and σ_x^2 stand for the mean and variance of $\log x$. The log-normal distribution assigns zero probability to the observable equal to zero. Consequently, this model provides poor performance in fitting single-look intensity speckle. However, it usually provides a better match to amplitude pdfs, especially in regions of strong spatial variation such as built-up areas [79], [80].

The Weibull distribution is given by:

$$p(x) = \frac{cx^{c-1}}{b^c} \exp\left[-\left(\frac{x}{b}\right)^c\right] \tag{3.40}$$

where b is a scaling parameter, and c controls the shape. With $c = 2$, the Weibull distribution becomes a Rayleigh pdf. Despite its higher generality compared with the Rayleigh distribution, it cannot represent multilook speckle adequately.

The Product Model

To overcome the general limitations of the previous speckle models and to ensure better fitting capabilities without losing physical meanings, the product model comes into play. It has been widely demonstrated that speckle formation is strictly related with the superposition of two unrelated processes that can be encapsulated in a product model [88]. In its simplest form, this speckle model combines an underlying RCS σ, with an uncorrelated multiplicative speckle contribution n so the observed SAR intensity can be expressed as:

$$I = n\sigma. \tag{3.41}$$

For L-look SAR intensity data, the pdf of speckle noise is:

$$p(n) = \frac{L^L n^{L-1}}{\Gamma(L)} \exp(-Ln). \tag{3.42}$$

This model is at the basis of most reconstruction filters and despeckling algorithms aimed at estimating the underlying RCS of the illuminated surface from noisy samples. It is noteworthy that, in order to exploit this model, it is necessary that the speckle noise fluctuations are on a much smaller scale than RCS.

In order to derive a statistical model for SAR data, a model describing the RCS fluctuations is required. For an assigned pdf of the RCS $p(\sigma)$, the pdf of the observed intensity reads as:

$$p(I) = \int_0^{+\infty} p(I|\sigma)p(\sigma)\, d\sigma = \frac{L^L I^{L-1}}{\Gamma(L)} \int_0^{+\infty} \frac{1}{\sigma^L} \exp\left[-\frac{LI}{\sigma}\right] p(\sigma)\, d\sigma. \tag{3.43}$$

The importance of the product model lies in the separation of the SAR data in two distinct contributions: a noise term, namely speckle, accounting for the random distribution of the scatterers within the resolution cell; an electromagnetic term, namely the RCS, depending on the physical properties of the surface.

RCS fluctuations are typically described by means of the gamma pdf, since it is the only distribution yielding to a closed-form analytic distribution for the SAR intensity. Therefore:

$$p(\sigma) = \left(\frac{\nu}{\mu_\sigma}\right)^{\nu} \frac{\sigma^{\nu-1}}{\Gamma(\nu)} \exp\left[-\frac{\nu\sigma}{\mu_\sigma}\right], \tag{3.44}$$

where ν is an order parameter and μ_σ is the mean RCS. A theoretical derivation of such a model based on the assumption of a random number of scatterers in the resolution cell is presented in[89].

Finally, by combining the speckle and RCS pdfs, the distribution of

L-look intensity SAR data can be derived from Eq. 3.43 [90]:

$$p(I) = \frac{2}{\Gamma(L)\Gamma(\nu)} \left(\frac{L\nu}{\mu_I}\right)^{(L+\nu)/2} I^{(L+\nu-2)/2} K_{\nu-L}\left[2\left(\frac{\nu L I}{\mu_I}\right)^{1/2}\right], \tag{3.45}$$

where $K_{\nu-L}(\cdot)$ is the modified Bessel function of order $\nu - L$. As $\nu \to \infty$, Eq. 3.45 tends to the gamma distribution.

The pdf of the amplitude ($A = \sqrt{I}$) is K-distributed as well:

$$p(A) = \frac{4}{\Gamma(L)\Gamma(\nu)} \left(\frac{L\nu}{\mu_I}\right)^{(L+\nu)/2} A^{(L+\nu-1)/2} K_{\nu-L}\left[2A\left(\frac{\nu L I}{\mu_I}\right)^{1/2}\right]. \tag{3.46}$$

In the radar field, the K distribution has been extensively exploited in modeling both sea [88], [89], [91] and land [92], [93], [94] clutter.

This page intentionally left blank.

Chapter 4

Global Navigation Satellite System-Reflectometry

In this Chapter, the GNSS-R technique for the remote sensing of the Earth's surface is described. The Chapter is organized as follows: in Section 4.1, the basic principles of the navigation services are introduced and the main GNSS developed or under development are briefly described. Navigation signals and messages adopted to address the navigation services and exploited in GNSS-based remote sensing applications are presented and discussed. Section 4.2 is devoted to the currently most important remote sensing technologies using GNSS signals of opportunity, namely GNSS-RO and GNSS-R.

4.1 Global Navigation Satellite System

GNSS denotes a positioning system developed from the second half of the twentieth century and primary designed to provide users located on or near the Earth's surface with the capability of determining their position. A GNSS is essentially based on a constellation of satellites orbiting around the Earth and transmitting navigation signals used by the users to locate themselves in real-time. To address this task, GNSS satellites are equipped with atomic clocks used to allow the user's receiver to compute the position of the transmitting satellite via the broadcasting of signals containing time information of the transmission. Range estimations are performed by measuring time or phase difference based on the correlation of two signals, namely the received satellite signal and a locally generated replica. By the knowledge of the position of at least four satellites, the user determines his/her position (and eventually further information, such as velocity and attitude) via triangulation.

Figure 4.1 shows the spectral allocation of the major GNSS navigation signals as established by the International Telecommunications Union (ITU) at the World Radio Communication Conferences in 2000 and 2003 [95]. GNSS services have been assigned to the Radio Navigation Satellite Service (RNSS), that makes use of the L-band and involves, for instance, television, radio, cell-phone, and radar satellite broadcasting services. The innovation of GNSS, including the GPS, is the use of a high-frequency Pseudo-Random Noise (PRN) code sequence as ranging signal.

Such systems are currently exploited in a wide range of applications, such as fleet management, search and rescue, wildlife tracking, vehicle guidance or leisure interactive maps, and many others. Currently, the most popular and widely used GNSS is the American GPS, fully operational since more than two decades. However, it is not the only GNSS in full use, since the GLONASS constellation, the Russian counterpart of GPS, is fully operational since 2010. The European Galileo will reach full operational capabilities in 2019, while the Chinese BeiDou-2 is scheduled to be completely operational on a global scale in 2020. When all the currently planned GNSSs will be fully deployed, users of multi-constellation receivers will benefit from more than 120 satellites, with a significant improvement of positioning performance, especially in the so-called urban canyons [96]. The wide availability of such signals has made GNSS a valuable source of signals of opportunity for Earth remote sensing, as discussed further in this Chapter.

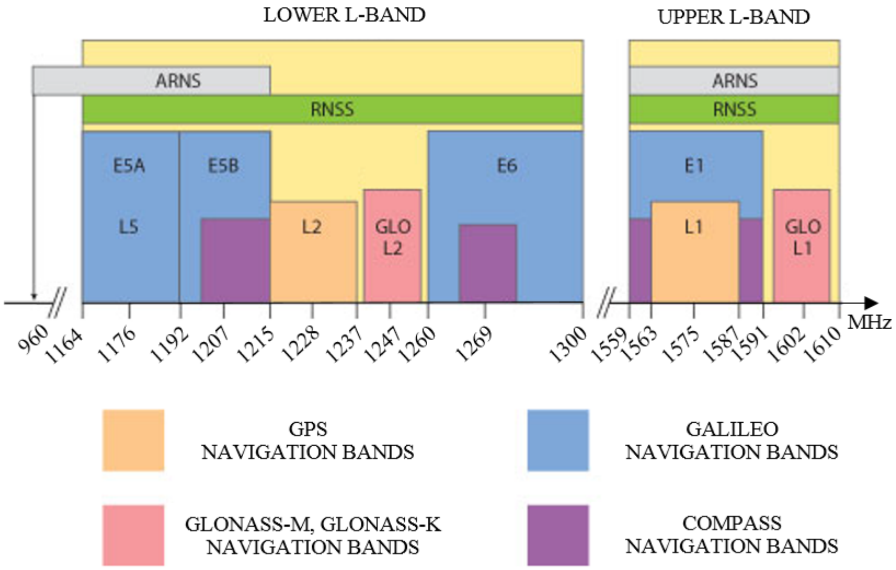

Figure 4.1. Radio Navigation Satellite Service band distribution. ARNS is the acronym for Aeronautical Ratio Navigation Service. This band is dedicated to safety-of-life services (i.e., civil aviation). RNSS is the acronym for Radio Navigation Satellite Service.

4.1.1 GPS

The GPS, also known as Navstar GPS or simply Navstar, is the US GNSS under the responsibility of the Joint Program Office (JPO), directed by the US Department of Defense. Despite its first use for military purposes, the US Congress promoted its extension to civilian use as well. The GPS project was launched in 1973 to overcome the shortcomings of early navigation systems, such as its immediate predecessor, namely the Navy

Navigation Satellite System (NNSS), also called Transit system, conceived in the late 1950s and developed in the 1960s by the US military [97]. The main objectives of GPS were the real-time determination of position and velocity (i.e., navigation), and the precise coordination of time (i.e., time transfer).

The current GPS constellation consists of 24 operational satellites deployed in six evenly-spaced planes with an inclination of 55° and with four satellites per plane. The orbital altitude is about 20,200 km above the Earth's surface with a period of approximately 12 sidereal hours. The constellation is completed with several further satellites active for replenishment. The full space segment provides global coverage with four to eight simultaneously accessible satellites above 15° elevation at any instant.

For point positioning and timing purposes, GPS provides two service levels: the Standard Positioning Service (SPS), freely available to all kinds of users on a continuous and worldwide basis, and the Precise Positioning Service (PPS), whose access is restricted to authorized users only, such as US armed forces, US federal agencies, and some other selected governments.

GPS provides a very high accuracy in both positioning - up to 13 m horizontally, and 22 m vertically - and velocity - up to a fraction of a meter per second - thanks to the precise control of all signal components with atomic clocks, producing the fundamental frequency $f_0 = 10.23$ MHz. From this frequency, two signals, named L1 and L2, are coherently derived by multiplying the fundamental frequency by 154 and 120, respectively, yielding

$$\begin{aligned} L1 &= 1575.42\text{MHz}, \\ L2 &= 1227.60\text{MHz}. \end{aligned} \tag{4.1}$$

These frequencies allow for a strong reduction of the main error source, i.e., the ionospheric refraction. To estimate the pseudo-ranges from each satellite to the receiver, two PRN codes are introduced and modulated onto the two carriers in Eq. 4.1. The first sequence is the coarse/acquisition (C/A) code, which is accessible to civilian users and define the SPS. It is currently superimposed upon the L1 signal only to deny full system accuracy to non-military users. The PPS is based on the second code, named precision (P) code. The P-code is modulated on both carriers L1 and L2 and is now encrypted to the Y-code to make it accessible to authorized users only. Each effective bit of the PRN code sequence is called a *chip*. Besides the PRN codes, further information regarding the satellite status, clock bias, and ephemerides is modulated onto the carriers. The PPS mode ensures a better precision in range measurements as compared to SPS owing to the tenfold smaller chip length of the P-code compared to the C/A-code. This also allows for a major robustness of the PPS against spoofing and jamming, thanks to the slower repeating PRN code. Besides the L1 and L2 signals, other navigation signals have been designed and implemented to address specific applications. The carriers L3 and L4 have been used for the development of nuclear detection systems. The L5 civil signal has been conceived and designed to meet the requirements of safety-of-life applications and to provide better autocorrelation and cross-correlation properties for enhanced navigation performance. The military M-code allows for a higher robustness against jamming, higher transmitted power, and higher security thanks to new cryptography schemes. All navigation signals emitted are right-hand circularly polarized. The main characteristics of the GPS navigation signals are listed in Table 4.1.

GPS uses a Code Division Multiple Access (CDMA) as channel access method. Consequently, GPS satellites share the same carrier frequencies and each station employs a unique PRN spreading code that modulates the carrier and is used in the receiver to separate the navigation signals transmitted from different satellites. Since its full operational capability, GPS has been providing three ranging code signals modulated onto two

Table 4.1. GPS navigation signals

Link	Factor ($\cdot f_0$)	Frequency [MHz]	Wavelength [cm]	ITU allocated bandwidth [MHz]	Frequency band
L1	154	1575.42	19.0	24.0	ARNS/RNSS
L2	120	1227.60	24.4	24.0	RNSS
L5	115	1176.45	25.5	24.0	ARNS/RNSS

carrier frequencies:

$$\begin{aligned} s_{L1}(t) &= a_1 c_P(t) d(t) \cos(2\pi f_1 t) + a_2 c_{C/A}(t) d(t) \sin(2\pi f_1 t), \\ s_{L2}(t) &= a_3 c_P(t) d(t) \cos(2\pi f_2 t), \end{aligned} \tag{4.2}$$

where $c_P(t)$ denotes the precision code, $c_{C/A}(t)$ is the coarse/acquisition code, and $d(t)$ represents the navigation message. The factor a_i represents the signal component power, and f_i is the carrier frequency.

The C/A code is modulated onto the L1 carrier and consists of 1023 chips with a duration of 1 ms; therefore, the frequency of this code is 1.023 megachips per second (Mcps). The main advantage of the C/A code is the fast signal acquisition owing to its relatively short duration. However, the maximum crosscorrelation level between two C/A-codes is about -24 dB, making this code susceptible to interference.

The more sophisticated P-code is generated by XOR-addition of two auxiliary codes, X1 and X2, generated by short cycling at 4092 and 4093 the output of four 12-bit Linear Feedback Shift Registers (LFSR). Thus, the strength of the P-code lies in its full duration of about 266.41 days that makes it very difficult to acquire if no a priori information is available.

4.1.2 GLONASS

The abbreviation GLONASS stands for the Russian “Global’naya Navigatsionnaya Sputnikovaya Sistema,” translated in English in Global Navigation Satellite System. The history of GLONASS dates back to the mid

1970s, when the GLONASS project, supported by the Union of Soviet Socialist Republics (USSR), started from the previously developed Doppler satellite system Tsikada. As defined by the Coordination Scientific Information Center in 2002, the main objective of GLONASS is to provide an "unlimited number of air, marine, and any other type of users with allweather three-dimensional positioning, velocity measuring and timing anywhere in the world or near-Earth space". Despite originally developed as a military system operated by the Russian military forces, in 1988 a free of charge diffusion of GLONASS signals was offered [98], and in September 1993 GLONASS was officially declared operational. However, the full constellation was completed in January 1996.

The full GLONASS constellation consists of 24 satellites - 21 active and 3 spares - in three 64.8°-inclined orbital planes and in circular orbits with an altitude of about 19,100 km, and a period of about 11 hours [98]. Each orbit contains eight equally spaced satellites. This constellation guarantees that at least five satellites are visible at a time on 99% of the Earth's surface [99].

Similar to GPS, GLONASS provides two operating services: a free of charge standard-accuracy service available to any user and a high-accuracy service for military use. Within the former service, the horizontal accuracy is between 13 m and 100 m, the vertical accuracy between 22 m and 156 m with a 95% probability, and the velocity accuracy is about 15 cm/s [97].

Two navigation signals are associated to the above-mentioned services: the standard-accuracy ranging code, namely the C/A-code (also referred to as the S-code), and the high-accuracy ranging code, i.e., the P-code. Two L-band subbands, G1 and G2, are used to carry the navigation signals: the C/A signal is modulated onto the G1 carrier frequency only, whereas the P-code is modulated onto both carriers.

The new-generation GLONASS-K satellites provide a third carrier frequency, namely G3, together with a new civil (C/A2) and military (P2) ranging codes. This update increases the reliability and accuracy of the GLONASS system and will especially be useful for safety-of-life applications [100]. The carrier frequencies of the navigation signals are listed in Table 4.2.

In order to allow the receiver to separate signals coming from different stations, GLONASS implements the Frequency Division Multiple Access (FDMA) technique, that ensures a high robustness against narrowband interference, and a low crosscorrelation of about -48 dB between different signals. However, extra-bandwidths are required to realize FDMA. In the near future, a possible switch to CDMA might be implemented in the GLONASS system [97]. Common PRN code sequences are shared by the entire GLONASS constellation, since identification of the transmitting source is addressed by means of FDMA.

All navigation signals are right-handed circularly polarized. The following unique carrier frequencies are used for all satellites:

$$\begin{aligned} f_{1k} &= f_1 + k\Delta f_1 = 1602.0000 + 0.5625k\,[MHz] \\ f_{2k} &= f_2 + k\Delta f_2 = 1246.0000 + 0.4375k\,[MHz] \\ f_{3k} &= f_3 + k\Delta f_3 = 1204.7040 + 0.4230k\,[MHz], \end{aligned} \tag{4.3}$$

where k differentiates the frequency channels, and Δf_i stands for the frequency increment between two adjacent channels. To reduce interference with radio astronomy frequency bands, 12 channels ($k = 1, 2, ..., 12$) have been assigned to GLONASS satellites.

The C/A code is generated through a 9-bit LFSR and it is 511 chips long with a chipping rate of 0.511 Mcps; therefore the code period is 1 ms. The maximum cross-correlation between two signals modulated onto adjacent carriers is about -48 dB. The P-code, generated via a 25-bit LFSR, has a rate of 5.11 Mcps with a duration of 1 s and has not been officially published. However, its decryption was demonstrated in the past, since it is not encrypted [97].

Table 4.2. GLONASS navigation signals

Link	Factor ($\cdot f_1$)	Frequency [MHz]	Increment [MHz]	Wavelength [cm]	Frequency band
G1	1	1602.00	0.5625	18.7	ARNS/RNSS
G2	7/9	1246.00	0.4375	24.1	RNSS
G3	94/125	1204.70	0.4230	24.9	ARNS/RNSS

4.1.3 Galileo

The Galileo constellation is the European Union's (EU) effort to develop both an alternative and a complementary to the other pre-existent GNSSs, GPS and GLONASS. A satellite-based navigation system has been a key research topic within the European Space Agency (ESA) since the 1980s, when a time division multiple access system was analyzed. However, only in 1994 the very first navigation system, named EGNOS, was developed with the objective of improving the previous GNSSs (i.e., GPS and GLONASS). In 1999, EGNOS became part of the Galileo project, conceived to be an open, global system independent from the other satellite-based navigation systems, while ensuring interoperability, and compatibility with them. To this aim, an agreement was signed in 2004 between EU and US to design and implement a common signal structure. The first Galileo satellite was launched in December 2005 and transmitted test signals shortly afterward [101]. Operational Galileo satellites launches began in 2011, and the system completion is currently scheduled for 2020.

The Galileo project has been conceived within a service-oriented framework, and four different service levels have been defined on the basis of user, application and operational needs [97]. Among them, the open service, providing free of charge navigation signals to any user, and the public regulated service, designed to provide support in situations of crises or malfunctioning. In the open service, six unencrypted signals are modulated onto three different carrier frequencies to provide a competitive and complementary navigation service compared to other GNSSs. The usage of several carrier renders the Galileo communications more robust towards EM interference sources, and, on the other hand, requires additional bandwidth resources. Compatibility and interoperability with other GNSSs are ensured by the partial overlap of frequency bands.

Concerning the space segment, the Galileo full satellite constellation will consist of 30 satellites - 27 operational and 3 spare - equally distributed in three nearly circular 56°-inclined orbital planes at an altitude of about 23,222 km. In nominal operating conditions, the Galileo system ensures a minimum of six satellites to be accessible simultaneously to every user on the Earth's surface.

The carrier frequencies are derived from the fundamental frequency $f_0 = 10.23$ MHz, which is coherently generated from the onboard atomic clocks. The complete list of carriers used for navigation service is presented in Table 4.3. For navigation purposes, signals are generated within the L-band to ensure compatibility with GPS and GLONASS, although other alternatives, such as C-band, were investigated for next-generation Galileo. In particular, the frequency band E1 spans from about 1559 MHz up to 1591 MHz, thus including the GPS L1 frequency band. In addition, the frequency bands E5a and E1 have been chosen in common to GPS (Galileo E5a coincides with GPS L5 and are used as synonym), while E5b overlays with GLONASS G3 to increase interoperability. The frequency bands listed in Table 4.3 are shared with several other services and users, such as military systems, primary radar, and radio amateurs.

Several navigation messages and PRN codes have been defined to meet the requirements of the different services provided by the Galileo system. In particular, 10 navigation signals have been defined in the frequency bands E5a, E5b, E6, and E1; furthermore, ranging codes are categorized into three types: the free of charge and publicly available open-access ranging code, the ranging codes encrypted with commercial encryption, and the

Table 4.3. Galileo navigation signals

Link	Factor $(\cdot f_0)$	Frequency [MHz]	Wavelength [cm]	ITU allocated bandwidth [MHz]	Frequency band
E1	154	1575.420	19.0	32.0	ARNS/RNSS
E6	125	1278.750	23.4	40.9	RNSS
E5	116.5	1191.795	25.2	51.2	ARNS/RNSS
E5a	115	1176.450	25.5	24.0	ARNS/RNSS
E5b	118	1207.140	24.8	24.0	ARNS/RNSS

ranging codes encrypted with governmental encryption. However, the access to the carrier frequency E6 and E1 is controlled. Dataless signals, consisting of PRN sequences only, have been introduced as pilot signal to improve tracking performance.

Similar to GPS, a CDMA approach is used for radio accesses management and separation of the different signal sources at the receiver. Consequently, a unique frequency is shared by all satellites.

In contrast with GPS and GLONASS, Galileo provides two different ways for PRN sequence generation: the former is the classical generation via LFSR, the latter is based on the construction and storage of optimized codes on board. LFSR-generated codes are derived from the combination (XOR-addition) of two short-cycled LFSR sequences, namely a long high-frequent primary code and a short low-frequent secondary code. The chip length of the secondary code coincides with the code length of the primary code. Therefore, the code length of the combined code sequence N_t is given by:

$$N_t = N_p N_s \tag{4.4}$$

where N_p and N_s stand for the length of the primary and secondary codes, respectively. This approach increases the robustness of the signal, while the short repetitive cycle allows for a fast acquisition procedure.

4.1.4 BeiDou-2/Compass

The BeiDou-2, also named BeiDou Navigation Satellite System, and formerly known as Compass, is a GNSS currently under development by China within the BeiDou project. The idea of a satellite-based navigation system was conceived in the early 1980s, and in 1993, China started developing the BeiDou system, designed to be a navigation system independent from US GPS and Russian GLONASS [97]. The BeiDou system consists of two separate but cooperating constellations: 1) BeiDou-1, completed in 2003 and designed to offer navigation services on a regional scale limited to China and neighboring regions including India, Malaysia and Philippines; 2) BeiDou-2, conceived as global navigation system based on the previous BeiDou-1 and planned to be fully operational in 2020.

BeiDou-1 comprises a constellation of four (three operating and one backup) satellites and served as an experimental test to validate navigation services on a regional scale. The main feature of this system is the usage of satellites orbiting in geostationary orbits, in contrast with other GNSSs. This configuration allows for a lower constellation size owing to the higher satellite altitude, but limits the coverage area to regions accessible by the spaceborne platform.

After the successful completion of the BeiDou-1 constellation, China began the second step of the BeiDou project, namely the global navigation system BeiDou-2, which became operational in December 2011. The full constellation, currently under development, is scheduled to be completed in 2020 and will consist of 35 satellites, including five geostationary orbit satellites for backward compatibility with BeiDou-1, and 30 non-geostationary satellites - 27 in medium Earth orbit and 3 in inclined geosynchronous orbit [102].

The 27 MEO satellites - 24 operational and 3 spare - will be evenly distributed in three orbital planes with an inclination of 55° at an altitude of 21,500 km. The satellites in geosynchronous orbit are planned to have the same configuration, but for the altitude of 35,785 km.

As other GNSSs, BeiDou-2 will offer two levels of service: a global open service to accomplish civilian navigation services to general users at no cost and designed to provide position accuracy of 10 m and velocity accuracy of 0.2 m/s [97]; a more accurate licensed service restricted to the Chinese government and military with a location accuracy of 10 cm [103].

When fully operational, BeiDou-2 will share four bands with Galileo, namely E1, E2, E5B, and E6, to ensure interoperability with the European GNSS and simplify the receiver design. On the other hand, these systems will face a major inter-system interference, especially within E1 and E2 bands, used for Galileo's open service [104]. Ranging codes will be broadcast using CDMA techniques with a signal structure similar to Galileo or GPS. However, very little has been officially announced about the signals, whose characteristics have been object of study by independent researchers, especially after the launch of the Compass-M1 satellite aimed at signal testing operations [105]. The signals transmitted by Compass-M1 have been detected as a coherent combination of two quadrature signals. The two signal components exhibit different code lengths: the shorter code is probably to be designed for the open service, whereas the longer codes are likely to accomplish the restricted service. In [106] and [107] short codes were completely decoded, allowing for the development of a hardware Compass receiver [108].

4.2 Remote Sensing Using GNSS Signals of Opportunity

Besides navigation services, GNSS signals and receivers have been opportunistically adopted as a remote sensing tool for observation and monitoring of Earth and other celestial bodies. Up to now, two main demonstrated applications of remote sensing from GNSS are atmospheric sensing via RO and reflectometry via bistatic radar. Both of these applications are covered in more detail in the next sections.

4.2.1 GNSS Radio Occultation

GNSS RO refers to the technology and methodology developed in the last five decades to infer physical properties of the atmosphere - temperature, density, and water content - from measurements of signals transmitted by occulted GNSS stations [109]. An occultation occurs when the celestial body of interest interposes itself between the observer and the signal source (another celestial body, transmitter), occulting (or hidding) the latter. Even if signals at various wavelengths can in general be used to implement remote sensing based on occultation techniques, RO refers to the case of *radio signals*, i.e., signals at a frequency $f \in [0, 300]$ GHz. RO techniques exploit the occultation event to infer the atmospheric structure of the celestial body of interest. The physical mechanism involved in these techniques is the distortion of the signal coming from the occulted source due to the presence of the atmosphere surrounding the middle object.

History of RO techniques dates back to 1960s, when the atmospheres and ionospheres of Mercury, Venus and Mars were sounded within Mariner V and Voyager space missions [110], [111]. In the 1980s, the possibility to profile the Earth's atmosphere at a relative low cost by means of RO techniques was allowed by the launch of the first emerging GNSS constellations [112]. Various studies have demonstrated that GPS-based RO measurements exhibit unique properties - self-calibration, high vertical resolution (< 1 km), all-weather sensing capabilities - as compared to other competitive remote sensing approaches [113], [114].

The RO concept using GNSS transmitters is pictorially shown in Fig. 4.2. A GNSS station outside the ionosphere transmits radio signals for its native navigation applications. The signal travels through the Earth's atmosphere and reaches a receiver mounted on board a Low Earth Orbit (LEO) spacecraft without line-of-sight (dashed line in the figure), i.e. hidden by the Earth. Indeed, along its path, the signal wavefront is bent by changes of the refractive index of the atmosphere. The LEO satellite tracks the GNSS station as it sets or rises through the Earth's atmosphere. By measuring and recording the change of the received radio signal characteristics, primarily the time delay, over the period of an occultation event, the behavior of the refractive index can be reconstructed as a function of time, and, then, inverted in vertical profiles by accounting for the movements of the transmitting and receiving satellites. Since the refractive index is directly related to electron density in the ionosphere, further atmospheric parameters, such as air density, temperature, pressure, and humidity, can be estimated [115], [116].

GNSS satellites are particularly suitable for the RO approach, since phase and amplitude of the GNSS navigation signals can be measured with extremely high precision. The conventional approach to retrieve atmospheric parameters from GNSS RO measurements is a two-step procedure: first, the bending angle profile is derived from the phase delay and SNR measurements as a function of the ray impact parameter; second, the bending angle profile is used to retrieve the refractive index and then the atmospheric parameters of interest. To this aim, a GO approximation is used to model the GNSS signal propagation.

The first constellation dedicated primarily to RO was FORMOSAT-3/COSMIC, launched in April 2006 and consisting of six microsatellites. The follow-on FORMOSAT-7/COSMIC-2 mission will launch a six-satellite constellation into low-inclination orbits in 2017, and another six-satellite constellation into high-inclination orbits in 2020. The GNSS RO payload will be able to track GPS, GLONASS and Galileo satellites at the same time, thus providing up to 12,000 profiles per day with both constellations for mesoscale weather forecasting, such as tropical cyclones, thunderstorms etc. For more in-depth details about the GNSS radio occultation technique in Earth and planetary sciences, the reader is referred to [110], [111], [117], [118].

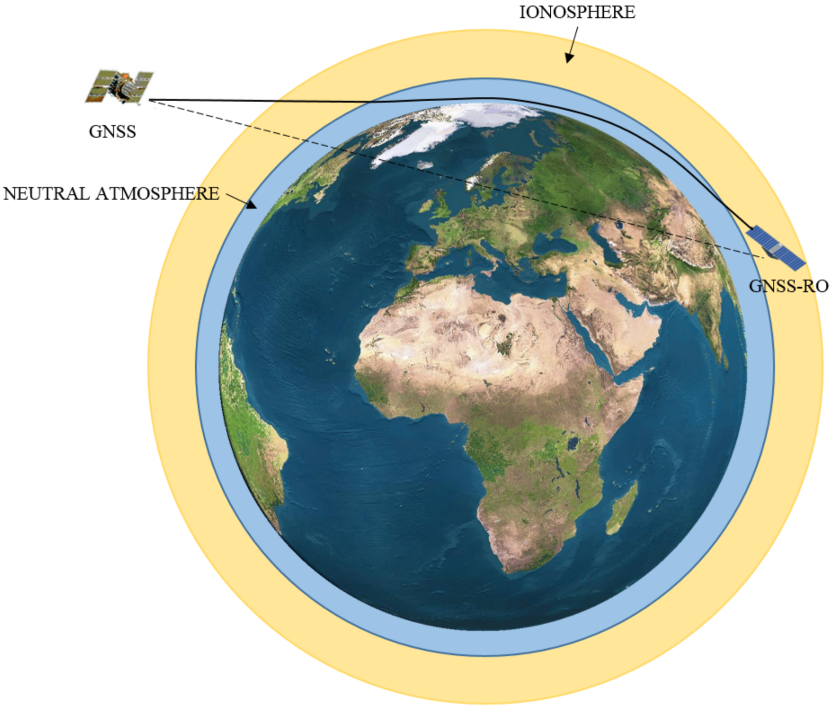

Figure 4.2. Geometry of a GNSS RO event. The navigation signal transmitted from the GNSS station propagates into the atmosphere and is bent as it travels due to the changes in the refractive index of the Earth's atmosphere (solid line). The signal source is hidden behind Earth and there is no line-of-sight (dashed line) between transmitter and receiver.

4.2.2 GNSS-Reflectometry

The acronym GNSS-R denotes a very recent remote sensing technique, whose full name clearly explain the basic working principle: the navigation signals transmitted by GNSS satellites are exploited for remote sensing purposes by taking advantage of the *reflection* of the GNSS signals on the

Earth's surface (Fig. 4.3). Basically, a GNSS-R system is a bistatic radar, i.e., a radar system in which transmitter and receiver are not colocated. Furthermore, it is commonly considered a passive system, in the sense that, for remote sensing purposes, GNSS satellites, even though they are an active source, exist a priori and then, are often considered as part of the environment.

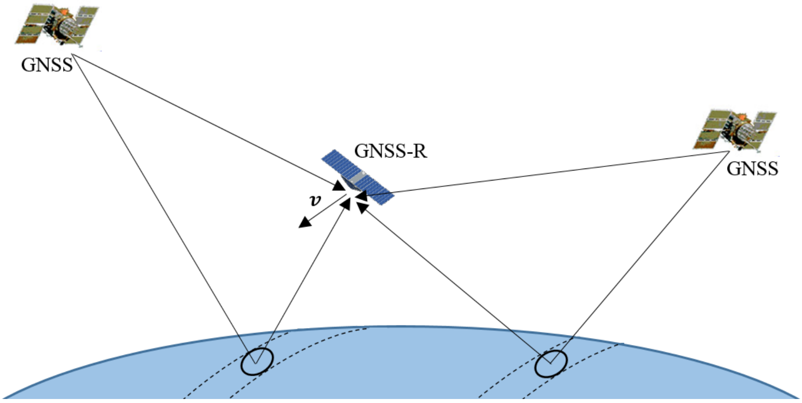

Figure 4.3. Illustration of GNSS-R basic principle. Signals coming from GNSS stations are reflected by the Earth's surface and acquired by the GNSS-R receiver.

Usage of Earth-reflected GNSS signals was first proposed for ocean remote sensing. In [119] Hall and Cordey applied GNSS-R concepts for ocean surface analysis; later, it was proposed as an alternative solution for ocean mesoscale altimetry by Martin-Neira in [120], and by Garrison *et al.* in [121] for ocean surface roughness. However, the first detection of GPS signals from a spacecraft was achieved by Lowe *et al.* via the acquisition of calibrated data from the SIR-C radar experiment on board the US Space Shuttle [122]. In the past decade, other GNSS-R remote sensing applications were conceived and demonstrated. Among them, retrieval of sea surface roughness represents one of the most investigated potentiality of GNSS-R-based bistatic radars [109], [117], [123], [124]. Interest for this application lies in the possibility to derive wind speed and direction on the sea surface, useful for near-surface meteorological conditions forecasting [124]. Other areas of pressing need were investigated as well: sea ice sensing was shown to be possible by Komjathy *et al.* in [125]; altimetry measurements were acquired in numerous aircraft campaings [126], [127]; feasibility of near-surface soil moisture content estimation for agriculture and urban planning applications was demonstrated by Katzberg *et al.*, at NASA Langley Research Center in [128]. Currently, GNSS-R applications include most of the applications of competitive active remote sensing instruments, such as ocean, land and cryosphere remote sensing [109], [129].

GNSS-R data can be used to retrieve geophysical parameters of the reflecting surface by exploiting the nature of the radiation-matter interaction, strictly related to the geometric and electromagnetic parameters of the surface. Indeed, the characteristics of the reflected GNSS signals can provide useful information about the reflecting surface. However, to fully address this objective, two main steps need to be addressed: 1) the received signal structure has to be related to the surface parameters of interest via a proper modeling of the scattering phenomenology involved in the data acquisition process. This step provides a mathematical description of the received signal waveform to be used in the second step; 2) the acquisition process has to be described in order to provide useful observables to be used in the retrieval algorithms.

Concerning the first step, the electromagnetic scattering problem has been deeply treated in Chapter 2 of this Ph.D. Thesis. Despite its limitations, the most widely used scattering model to describe sea surface bistatic scattering is the GO approximation under the KA approach [37]. It describes the EM scattering from a rough surface modeled as a 2-D stochastic Gaussian process and provides quite accurate results in the computation of the quasi-specular scattering cross-polar component. Hence, it is particularly suitable to model the forward scattering typical in the bistatic

GNSS configuration.

As explained in Chapter 2, within the GO framework, the illuminated surface is decomposed in a set of elementary facets, whose size is much larger than the EM wavelength. Each facet is approximated as the plane locally tangent to the surface, and therefore, reflects the incident EM wave in the specular direction only, contributing to the scattered energy proportionally to the probability to produce a specular reflection to the receiver. The total scattered EM field is the coherent sum (integral) of all these contributions over the illuminated surface. In [37], Zavorotny and Voronovich adopted the GO approach to model the reflection on the sea surface of the GPS signal. The received signal is modeled as follows:

$$u(\mathbf{r},t) = \int D(\mathbf{r})a\left[t - \frac{R_0 + R}{c}\right]g(\mathbf{r},t)\,d\mathbf{r}, \tag{4.5}$$

where the reference system is centered on the specular reection point, R_0 and R are the distances from a given surface's point to the transmitter and receiver respectively, $D(\mathbf{r})$ is the antenna pattern value evaluated at the surface's point denoted by $\mathbf{r}$, and

$$g(\mathbf{r},t) = -R_p \frac{\exp(-2\pi j f_{L1} t)}{4\pi j R_0 R} \exp[jK(R_0 + R)] \frac{|\mathbf{q}|^2}{q_z}, \tag{4.6}$$

where R_p is the polarization-dependent reflection coefficient (Eq. 2.18), q_z is the vertical component of the scattering vector $\mathbf{q} = (\mathbf{q}_\perp, q_z)$ defined in Eq. 2.26.

GNSS-R Observable: the Delay-Doppler Map

Once the scattering mechanisms are accounted for, and the received signal has been properly modeled, the second step, consisting in modeling the acquisition process, comes into play. The output of the acquisition process is the so-called *observable*, namely a measurable entity (scalar values, arrays,...) from which geophysical information can be derived. So far, numerous types of GNSS-R observables have been defined and used in the literature; a thorough list can be found in [130], [131]. However, the DDM represents the primary and one of the most used observable, from which the other observables can be derived [130].

Since GNSS is not primarily designed for remote sensing applications, the received Earth-reflected signal exhibits a very low power, well below the (speckle plus thermal) noise level. Therefore, the main aim of the acquisition procedure is to increase the quality (SNR) of the signal. To this aim, the DDM observable takes advantage of the autocorrelation properties of the navigation signals of GNSSs based on CDMA. This is done by correlating the received signal with a local replica of the PRN code. By spanning the delay and doppler shift over a 2-D domain, a map of the reflected power in the delay-Doppler domain, the so-called DDM is obtained. It can be modeled as follows:

$$Y(\Delta\tau, \Delta f_D) = T_c \int D(\mathbf{r})\chi(\Delta\tau, \Delta f_D) g(\mathbf{r}, t_0)\, d^2\mathbf{r}, \tag{4.7}$$

where $\Delta\tau$ and Δf_D stand for the delay lag and Doppler shift w.r.t the signal reflected at the specular point, T_c is the coherent integration time, and $\chi(\Delta\tau, \Delta f_D)$ denotes the autocorrelation function of the PRN sequence code, even referred to as Woodward Ambiguity Function (WAF). The WAF of the GPS C/A code can be approximated as the factorization of a delay lag-dependent and a Doppler shift-dependent functions, i.e., as follows:

$$\chi(\Delta\tau, \Delta f_D) \approx \Lambda(\Delta\tau) S(\Delta f_D), \tag{4.8}$$

where $\Lambda(\cdot)$ is a triangular function, and $S(\cdot)$ is a sinc function. Equation 4.7 models a single-snapshot DDM, i.e., the DDM obtained by correlating the coherently acquired signal. Consequently, the output map is still greatly affected by noise and an additional averaging process is required. To this aim, an incoherent integration of single-snapshot DDMs is performed over a quite long time interval. The subsequent averaged DDM can be expressed in terms of the pdf of the surface local slopes:

$$\overline{|Y(\Delta\tau,\Delta f_D)|^2} = T_c^2 \int\int \frac{|R_p|^2}{4\pi R_0(\mathbf{r})R(\mathbf{r})} D(\mathbf{r})\Lambda^2(\Delta\tau)S^2(\Delta f_D) \times \frac{|\mathbf{q}|^4(\mathbf{r})}{q_z^4(\mathbf{r})} p\left(-\frac{\mathbf{q}_\perp}{q_z}\right) d^2\mathbf{r}, \quad (4.9)$$

Equations 4.7 and 4.9 are commonly known as Z-V model [37].

From a practical point of view, owing to its low computational complexity, the complex DDM is computed directly on board as follows:

$$Y(\tau, f_D) = \int_0^{T_c} s(t)a(t+\tau)\exp[-j2\pi(f_{PRN}+f_D)t]\,dt, \quad (4.10)$$

where $s(\cdot)$ is the received signal, $a(\cdot)$ is the local replica of the PRN code at frequency f_{PRN}, τ and f_D represent the delay-Doppler point where the DDM is evaluated. The incoherently-averaged power DDM is computed as the average of N successive power DDMs:

$$\overline{|Y(\tau, f_D)|^2} = \frac{1}{N}\sum_{n=1}^{N}|Y(\tau, f_D)|^2, \quad (4.11)$$

where the incoherent integration time is $T_i = NT_c$.

An interpretation of the DDM observable follows. Each Earth's surface point corresponds to a point in the delay-Doppler domain determined by the delay lag and Doppler shift of the signal coming from that surface point w.r.t. the signal coming from the specular point. The reverse is not true, since a point in the delay-Doppler domain corresponds to the intersection points between the iso-delay and iso-Doppler lines, namely two points (if intersections exist) or no point (if no intersection exists). Therefore, the

DDM consists of two separate regions: a forbidden region, i.e., the portion of the delay-Doppler domain not corresponding to any geographical counterpart; an allowed region, called *glistening zone*, in which each pixel can be interpreted as the energy scattered from two points inside this region. In other words, the DDM is a 2-D function that can be regarded as the distribution of the scattered power over the glistening zone. The size of the glistening zone, i.e., the region contributing to the scattered energy, is strictly related to the surface roughness: a perfectly smooth surface (for instance very calm sea) totally reflects the incident EM wave in the specular direction and a coherent scattering mechanism is present; consequently, in the GNSS-R configuration, only the specular point contributes to the received signal and the DDM presents an unique bright point. Generally speaking, the rougher the surface, the wider its radiation pattern (the more significant the incoherent scattering contribution), the wider the glistening zone.

Chapter 5

SAR Despeckling Based on Scattering Models

In this Chapter, the SAR despeckling approach based on the use of scattering models is introduced and described. The proposed approach relies on the exploitation of a priori information concerning the scattering behavior of the surface to reduce speckle effects in SAR imagery. The proposed algorithms, named SB-PPB and SB-SARBM3D, represent a modification of the original despeckling algorithms, namely PPB and SARBM3D, in which physical issues related to the electromagnetic properties of the surface come into play.

The Chapter is organized as follows: in Section 5.1, recent and classical approaches to the despeckling problem are briefly presented and discussed; in Sections 5.2 and 5.3, the original SARBM3D and PPB despeckling algorithms are deeply described and discussed; the proposed SB-SARBM3D and SB-PPB filters are introduced and described in Section 5.4.2 and Section 5.4.3, respectively; the filters performance is assessed on both synthetic noisy and actual SAR images in Section 5.5; the results of an experimental sensitivity analysis of both SB-PPB and SB-SARBM3D are pointed out and discussed in Section 5.6.

5.1 State of the Art in SAR Despeckling

SAR images are affected by speckle, which prevents their use in automatic tools for information extraction, and renders their interpretation challenging even for human experts. Often, this problem is contrasted by resorting to some forms of multilook, with the remarkable side effect of losing spatial resolution. A more appealing alternative is to resort to signal processing, looking for SAR despeckling techniques that suppress speckle in homogeneous areas without losing resolution and without impairing the image features of interest. Several techniques have been proposed to tackle this issue [4]. The first approaches known in the literature are local spatial filters [13], [15], [16], which take into account the non-stationarity of the image by adapting the filter to the local statistics within a fixed-size sliding window. Specifically, most of these filters adopt a test to discriminate homogeneous from heterogeneous areas based on the local coefficient of variation, which is a simple and robust index of textural content. In this way, a good balance between smoothing and edge preservation can be achieved. These techniques have the merit of simplicity, but, in general, are characterized by a limited despeckling power.

In order to better take into account the characteristics of the scene fluctuations, a Maximum a Posteriori (MAP) approach is followed in [18], modeling both the scene and the speckle through a Gamma distribution. Improved versions of these filters have been proposed in [132], using the local coefficient of variation combined with a ratio edge detector [17] not only to inhibit smoothing near edges, but also to enhance the edges themselves. In [19], instead, a new model is proposed which better fits SAR data in textured areas, and a more appropriate strategy is used to handle edges and strong scatterers. Still in the context of MAP formulation, a different texture modelization, based on Gauss-Markov Random Fields, is proposed in [133], together with an ad hoc strategy to detect and preserve strong scatterers and borders between regions of uniform backscattering.

More sophisticated methods rely on the use of transforms, which provide a manageable sparse representation of the signal. Several algorithms based on Wavelet Transform (WT) followed by coefficient shrinkage have been proposed. In particular, by using redundant WT [134], [135], they are also able to avoid annoying artifacts such as Gibbs-like ringing in uniform areas and near edges. In this context, a central issue is the adoption of non-linear shrinkage for the wavelet coefficients. Even though deterministic shrinkage represents a simple and effective solution, especially in its adaptive version [134], better results can be expected from statistical shrinkage, and its use in the context of MAP approaches has led to a great variety of filters. Also in this case, results can be improved by taking into account the spatial heterogeneity, as done for example in [136], or in [22], where the local texture energy is used to classify wavelet coefficients and adapt the filtering strategy. More recent techniques take advantage of bidimensional transforms better fit to represent edges, like bandelets [137] and curvelets [138]. Instead of using a fixed transform, an alternative approach is to build an adaptive dictionary from the image itself, as done in [139], [140], [141].

Recently, the nonlocal approach [25] has gained much popularity in this field, proving very effective for various SAR imaging modalities [5]. The basic idea is to take advantage of image self-similarity. Each target pixel is reconstructed through the weighted average of those pixels that are deemed to be more similar to it. These may be located anywhere in the image, not necessarily close to the target. The central issue, therefore, is to find a suitable measure of similarity, typically patch-based, to find these optimal predictors. The basic idea of the nonlocal approach is very intuitive, but it represented a total breakthrough in the denoising community: similarity is no more intended in a pure and exclusive geometrical sense. The geometric Euclidean distance was substituted by the more meaningful intensity distance aimed at averaging only those objects sharing the same physical properties, i.e., the reflectivity. In other words, only those pixels presenting similar amplitude values are averaged, irrespective of their geometric distance. The more similar two pixels are, the greater the weight assigned to them in the average process. The Euclidean intensity distance first proposed by Buades *et al.* in [25] was designed and derived in the assumption of AWGN. This distance was recently modified by Deledalle *et al.* in [26] to account for the special characteristics of SAR speckle noise, as discussed further in this Chapter. Interestingly, a rough form of nonlocal filtering was already present in the well-known sigma filter for additive signal-independent noise [142], later improved in [75], [133], [143] to deal with speckle noise in SAR imagery. In recent years, a number of nonlocal techniques have been proposed for SAR despeckling, e.g., [24], [26], [27], [144]. The most popular among them are arguably PPB [26], characterized by an excellent speckle suppression ability, and SARBM3D [24], which ensures a very good preservation of fine image features. Up to now, NLM represents one of the most widespread, accurate, and promising approaches to SAR imagery despeckling [4], [5], [24], [26], [145]. These patch-based nonlocal algorithms very often show better results w.r.t. other methods [4], [5], [24], [26], [145], although they present some limitations and difficulties in very specific cases, especially for small non-repetitive features, due to the failure of the patch-matching step. A detailed description of the PPB filter, on which the proposed SB-PPB filter is based, is reported in the following.

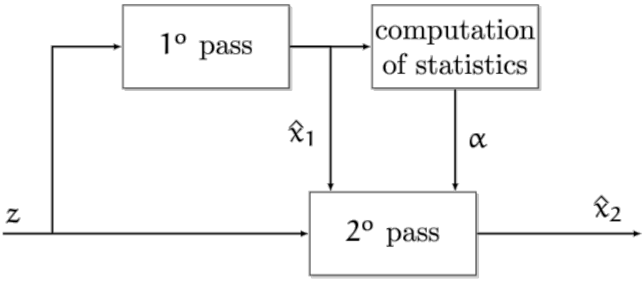

Figure 5.1. Block-scheme of the 2-pass SARBM3D filter.

5.2 SAR Block Matching 3-D Algorithm

The SARBM3D algorithm, originally developed in [24] by Parrilli *et al.*, is a SAR-oriented version of the previous BM3D filter proposed by Dabov *et al.* in [146] and designed for denoising images corrupted by AWGN. In the BM3D framework, the nonlocal approach is combined with wavelet shrinkage and Wiener filtering in a two-step process as shown in Fig. 5.1.

In the first stage, an hard-thresholding in the wavelet domain is used to provide a basic estimate of the clean image and image statistics used in the second stage, where the actual denoising takes place through empirical Wiener filtering in the transform domain. The processing flow is as follows. The first stage comprises the following three passes:

1. Grouping: image patches (block of pixels) are collected in 3-D groups with a similarity criterion based on a minimum Euclidean distance between pixel intensity values.

2. Collaborative filtering: an hard-thresholding in the wavelet domain, followed by inverse WT, is applied to each 3-D group.

3. Aggregation: every block is positioned in its original position in the image domain and contributes to the image statistics estimation with a proper weight.

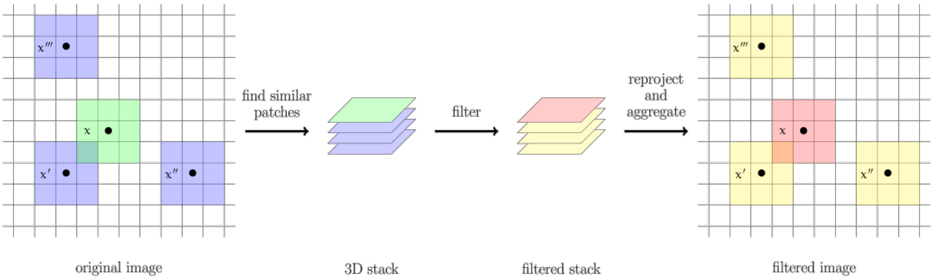

Figure 5.2. Nonlocal block-matching 3-D in SARBM3D. Inspired to Fig. 2 of [5].

In the grouping step the nonlocal principle comes heavily into action. For each target block, the most similar blocks in the neighborhood are located, and collected in a 3-D stack for the subsequent filtering steps (see Fig. 5.2). This nonlocal approach, based on collecting multiple instances of a block in a 3-D stack, is aimed at exploiting the inherent self-similarity exhibited by both radar and optical images to mimic a true statistical filtering based on the stationarity of the signal.

The second step performs the same stages with the differences highlighted in the following:

1. Grouping: the metric used to collect similar blocks is based on the clean image estimation addressed in the first step.
2. Collaborative filtering: all the 3-D blocks undergo Discrete Cosine Transform/WT, Wiener filtering, and inverse transform.
3. Aggregation: the same as in step one.

5.2.1 Dealing With SAR Speckle Noise

SARBM3D departs from its AWGN counterpart under two respects: 1) the use of a block similarity measure tailored to speckle statistics; 2) the use of undecimated WT and Wiener filtering in place of ordinary WT and hard thresholding in the first pass.

Following the usual multiplicative noise model, the observed signal is expressed as

$$z(s) = x(s)n(s) \tag{5.1}$$

where the spatial location is indicated by a single letter for compactness, $z(s)$ and $x(s)$ are the observed and clean signal intensities, and the speckle samples $n(s)$ are independent and identically distributed Gamma random variables. Accordingly, $\hat{x}_1(s)$ and $\hat{x}_2(s)$ are the intensities estimated in the first and second pass.

Nonlocal filtering relies heavily on a suitable measure of similarity. The problem of determining such a measure, depending on noise statistics, has been studied in several papers [147], [148], [149]. A widespread approach, well supported by experimental evidence, is to define the similarity between two noisy observations as the likelihood that they come from the same underlying signal before being corrupted by noise, i.e.,

$$p[a(s), a(t)|x(s) = x(t)] \tag{5.2}$$

where, following [26], we use signal amplitudes $a(s) = z(s)$, rather than intensities, and p indicates a probability density function. Assuming AWGN, this approach leads to the Euclidean distance as a measure of dissimilarity. With L-look SAR images, however, it leads to a different distance

$$d_1[a(B_s), a(B_t)] = (2L-1)\sum_k \log\left[\frac{a(s+k)}{a(t+k)} + \frac{a(t+k)}{a(s+k)}\right] \tag{5.3}$$

where B_s indicates a block centered in s, $a(B_s)$ the corresponding amplitudes, and k scans the block pixels. This distance has been used with success in several nonlocal despeckling techniques. Besides having solid statistical bases, using the ratio of samples rather than their difference makes full sense for multiplicative noise, as it makes the distance independent of the average signal level. When other estimates of the signal are available, coming for example from other sensors [150], the distance can be modified to take into account this side information. This is the case of the second pass of SARBM3D, where the first-pass pilot estimate is already available and the distance is therefore modified accordingly. The other major innovation introduced in SARBM3D concerns the first-pass filtering step aimed at providing the pilot image. As already said, a good pilot is essential for the success of the final despeckling step, especially when the original image is very noisy, as is the case of single-look SAR images. Hence, it makes full sense replacing hard and soft wavelet thresholding with Wiener filtering, which is theoretically optimal. To perform well, however, the latter needs reliable estimates of statistics. When this is not the case, a simpler but more robust thresholding may still be preferable. To address this issue, SARBM3D resorts to Undecimated Discrete Wavelet Transform (UDWT) rather than critically sampled WT. Without decimation, a large number of samples (though more correlated) become available in each subband to estimate the variance of wavelet coefficients, allowing the correct functioning of the Wiener filter. The price to pay is an increase in computation time and memory usage, which is more acceptable as technology progresses.

In [24], the multiplicative noise model is first of all converted in an additive signal-dependent noise model

$$z(s) = x(s)n(s) = x(s) + x(s)[n(s) - 1] = x(s) + v(s) \tag{5.4}$$

Then, resorting to some reasonable simplifications, the filtered wavelet coefficients are computed as [24]

$$\hat{X}_1(i) = \max\left(0, \frac{\left\langle Z^2 \right\rangle_{SB(i)} - \frac{\sigma_u^2}{1+\sigma_u^2} \left\langle z^2 \right\rangle_G}{\left\langle Z^2 \right\rangle_{SB(i)}}\right) Z(i) \qquad (5.5)$$

where $\langle\cdot\rangle_{SB(i)}$ and $\langle\cdot\rangle_G$ stand for the average over the sub-band comprising the i-th coefficient and the whole group, respectively; σ_u^2 is a known parameter depending on the speckle format and the number of looks [151]; capital letters indicate wavelet coefficients. In 5.5 all quantities within the crochets can be estimated reliably by sample averages [24], either over the UDWT subband the coefficient belongs to $\langle\cdot\rangle_{SB}$, or over the whole 3-D stack $\langle\cdot\rangle$. Inverse transform provides eventually the filtered image.

5.2.2 Strengths and Weaknesses

We now focus on the advantages and drawbacks of SARBM3D, only partially highlighted in the above description. Its major strength is certainly the ability to preserve image details, like man-made structures, textures, region boundaries, etc. This is due to the nonlocal approach. Since details represent rare “anomalies” as opposed to the larger homogeneous areas, it is only by collecting multiple similar patches in a large area that one can gather enough information to perform a reliable estimation. This information is then exploited very effectively in SARBM3D by means of a number of sophisticated tools, such as UDWT, Wiener filtering, and the aggregation of multiple estimates. The strengths of SARBM3D, however, are also its weaknesses. Since it preserves very well image structures, it tends to preserve also random patterns originated by speckle in homogeneous areas. Therefore, the speckle suppression in homogeneous areas is not as strong as happens with some competing techniques, e.g., PPB. On the other hand, speckle suppression and detail preservation are inherently contrasting requirements. Interestingly, the reinforcement of random patterns gives rise to despeckling artifacts only occasionally. This important property must be credited to the UDWT/Wiener suite in the first pass which produces a pilot image free of the typical wavelet-basis artifacts. In fact, replacing UDWT with WT, as done in FANS [144] to reduce complexity, originates a number of annoying artifacts. It is therefore reasonable to expect that improving further the pilot, by using some available side information, will entail significant benefits on the final filtered image.

5.3 Probabilistic Patch-Based Algorithm

In their original work, Deledalle *et al.* [26] proposed a probabilistic approach for filter weight evaluation based on the Weighted Maximum Likelihood Estimation (WMLE). The image denoising problem consists of finding the best estimate of the parameter of the parametric noise distribution $p(A_s|\sigma_s)$, with A_s being the amplitude sample located in s and σ_s being a space-varying unknown parameter, assumed to be the reflectivity, i.e., the NRCS, of the scene at pixel s (so that the noise-free amplitude A_s^* is the square root of σ_s). In [26], it was shown that, if the pixel amplitudes are modeled as independent and identically distributed according to the Nakagami–Rayleigh distribution [11], in agreement with the usual multiplicative speckle noise description, then the WMLE of σ_s can be expressed as

$$\hat{\sigma}_s^{WMLE} = \frac{\sum_{t\in\Omega} w_{s,t} A_t^2}{\sum_{t\in\Omega} w_{s,t}} \tag{5.6}$$

where Ω is a (large) window centered at s (search window) and the weight $w_{s,t} \in [0,1]$ depends on the target pixel s and the test pixel t; it can be also seen as a measure of the similarity between the two pixels. The definition of the weights is the key-point of the NLM techniques, as they are directly related to the accuracy of the algorithm. In order to take into account the neighborhood of the pixel under study, in [26], the patch concept is introduced, and the weight is evaluated as the probability that the two patches Δ_s and Δ_t, centered at s and t, respectively, share the same parameters

$$w_{s,t}^{non-it.PPB} \triangleq p(\sigma_{\Delta s} = \sigma_{\Delta t} | A)^{\frac{1}{h}} \tag{5.7}$$

where $h > 0$ is a filter parameter setting the weight decay and the superscript "non-it. PPB" stands for non-iterative PPB. In order to refine the weights, Deledalle *et al.* [26] proposed also an iterative scheme in which the reflectivity estimation at step $i - 1$, $\hat{\sigma}^{i-1}$, is used as a kind of a priori knowledge at step i

$$w_{s,t}^{it.PPB,i} \triangleq p(\sigma_{\Delta s} = \sigma_{\Delta t} | A, \hat{\sigma}^{i-1})^{\frac{1}{h}} \tag{5.8}$$

with the obvious meaning of the superscript "it. PPB". In addition, using again the Nakagami–Rayleigh distribution for modeling the speckle noise and the Kullback–Leibler divergence for modeling the a priori knowledge, the following weight expression can be derived [26]:

$$w_{s,t}^{it.PPB,i} = \exp\left[- \sum_k \left(\frac{1}{\tilde{h}} \ln\left(\frac{A_{s,k}}{A_{t,k}} + \frac{A_{t,k}}{A_{s,k}} \right) + \frac{L}{T_{fil}} \frac{|\hat{\sigma}_{s,k}^{i-1} - \hat{\sigma}_{t,k}^{i-1}|^2}{\hat{\sigma}_{s,k}^{i-1} \hat{\sigma}_{t,k}^{i-1}} \right) \right] \tag{5.9}$$

where L stands for the equivalent number of looks, $\tilde{h} = h/(2L - 1)$, T_{fil} is a filter parameter dictating the decay of the Kullback–Leibler divergence, and k is an index that identifies the pixels within patches Δ_s and Δ_t, so that, for instance, $A_{s,k}$ is the amplitude of the $k-$th pixel of the patch Δ_s. The logarithmic term in Eq. 5.9 weights in an optimal way (in the framework of an WMLE approach) the observed amplitude image samples via a distance suitable for SAR data, whereas the second term takes into account the previous estimate in an iterative scheme and is aimed at avoiding filtering samples drawn from different distributions. For $T_{fil} \to \infty$, we have the non-iterative version of the algorithm, for which

$$w_{s,k}^{non-it.PPB} = \exp\left[-\sum_k \left(\frac{1}{\tilde{h}} \ln\left(\frac{A_{s,k}}{A_{t,k}} + \frac{A_{t,k}}{A_{s,k}}\right)\right)\right]. \qquad (5.10)$$

Since a complete description of the PPB filter goes outside the scope of this Ph.D. Thesis, the reader is referred to [26] for more details.

5.4 Scattering-Based Despeckling

Most state-of-the-art techniques are based on statistical and/or geometrical concepts and approaches, with limited physical insight [3], [4]. Even well-known and well-assessed despeckling techniques ([13], [15], [16]) do not take into any account the physical mechanisms and phenomena involved in SAR image formation. Nonetheless, electromagnetic scattering plays a key role in SAR imagery acquisition process: a SAR image can be modeled as the reflectivity pattern of the illuminated scene filtered by the SAR system [28], [29]. Scattering phenomena are also responsible of the speckle noise that affects every coherent acquisition system like SAR sensors. By explicitly taking into account the electromagnetic phenomena of interest for SAR image formation, notably, the scattering mechanisms, a physical-based approach to despeckling can be pursued. This kind of approach has the potential to provide more reliable and artifact-free SAR images and eventually more informative SAR products, readable also by non-expert SAR users. A first attempt in this direction, only applicable to polarimetric SAR data, can be found in [152]. In this Ph.D. Thesis, the exploitation of scattering models within the despeckling processing chain is investigated and discussed. Two scattering-based despeckling algorithms, namely SB-SARBM3D and SB-PPB have been conceived, implemented and tested. The proposed filters rely on the introduction of a priori information about the electromagnetic energy backscattered from the resolution cell. To this aim, we focus on natural surfaces, that are modeled via the fractal geometry as described in Chapter 2. In particular, as anticipated in Chapter 2, the illuminated surface roughness is modeled as a 2-D fBm stochastic process and its scattering behavior is described through the SPM model. Therefore, the surface NRCS is represented by Eq. 2.15 and is estimated and injected as a priori information in the proposed despeckling algorithms. The ways such a priori information is introduced in the despeckling chain represent the core part of the proposed algorithms and are discussed in Section 5.4.2 and Section 5.4.3. It is noticeable that the proposed surface and scattering models correctly describe single-bounce phenomena occurring on natural surfaces and scenarios (rocks, geomorphologic relief, bare, or little vegetated soil). Multiple-bounce and volume-scattering phenomena — mainly inherent to man-made and vegetated areas — are not taken into account. The next Section discusses the estimation of the surface NRCS.

5.4.1 Estimation of the a Priori Scattering Information

The estimation of the surface NRCS as described in 2.15 requires the knowledge/estimation of a number of surface parameters, such as complex dielectric constant, local incidence angle, microscopic roughness, and topothesy. Even though it is not reasonable to know in advance this information (which would make useless the SAR image itself), an accurate estimation of the surface NRCS is still possible. To this aim, a sensitivity analysis of the scattering behavior of the surface against both electromagnetic and geometric surface parameters is performed. Figure 5.3 shows the dependency of the surface NRCS, evaluated through 2.15, against the local incidence angle, the relative dielectric constant, the electrical conductivity, the Hurst coefficient and the topothesy. All the graphs show that the major contribution to SAR image formation is due to the topography, i.e., to the local incidence angle. In particular, it is important to note that also the microscopic roughness, i.e., Hurst coefficient and topothesy, have a minor influence on SAR image intensity w.r.t. the macroscopic one.

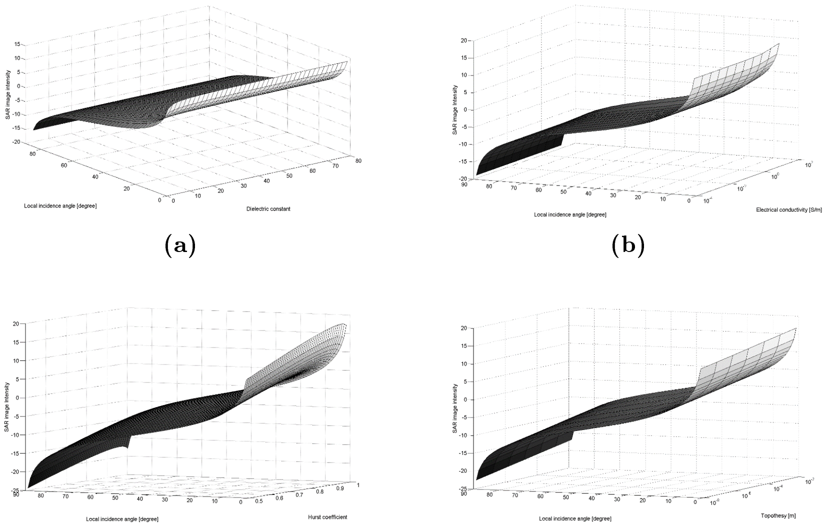

(a) **(b)**

(c) **(d)**

Figure 5.3. Surface NRCS dependencies (see Eq. 2.15): (a) incidence angle vs. dielectric constant assuming $T = 10^{-4}$ m, $H = 0.8$ and $\sigma_c = 10^{-2}$ S/m; (b) incidence angle vs. electrical conductivity assuming $T = 10^{-4}$ m, $H = 0.8$ and $\varepsilon_r = 10$; (c) incidence angle vs. Hurst coefficient assuming $T = 10^{-4}$ m, $\varepsilon_r = 10$ and $\sigma_c = 10^{-2}$ S/m; (d) incidence angle vs. topothesy assuming $\varepsilon_r = 10$, $H = 0.8$ and $\sigma_c = 10^{-2}$ S/m. All graphs are in logarithmic scale on z-axis; electrical conductivity and topothesy axes are in log scale, too.

The local incidence angle can be estimated from a DEM of the sensed surface, if available. The estimate reads as [28]

$$\vartheta = \cos^{-1}\left(\frac{\alpha \sin\vartheta_0 + \cos\vartheta_0}{\sqrt{\alpha^2+\beta^2+1}}\right) \tag{5.11}$$

where ϑ_0 is the radar look angle (i.e., the incidence angle over an horizontal surface), and α and β are the range and azimuth slopes, respectively.

The ability to retrieve the incidence angle is a key ingredient of our proposal. In fact, the SPM NRCS depends heavily on this parameter and much less on other ones, such as the relative dielectric constant, electrical conductivity, and topothesy. Therefore, a good estimate of the NRCS can be obtained even based on this only information. To this end, the local incidence angle map has to be projected into the SAR system geometry and coregistered to the noisy SAR image. The microscopic roughness, instead, can be estimated from the SAR image via the algorithm developed by Di Martino *et al.* [28] once assumed that the same value of H holds at both macroscopic and microscopic scales. This latter is a rather strong assumption, but again, the sensitivity analysis shows that errors on the value of H do not appreciably affect scattering evaluation if a significant topography is present. In conclusion, the NRCS can be estimated based only on the scene DEM, and the approximation is quite accurate where surface scattering is the dominant scattering component, namely, in natural areas with gentle topography or homogeneous flat regions. It is noteworthy to underline that accurate DEMs are by now easily available for most part of the world, often free of charge. In fact, the Shuttle Radar Topography Mission [153] provided a DEM of the entire Earth (with the exception of polar areas), freely available at [154]. In addition, Lidar data providing very high resolution DEMs are becoming more and more widespread, especially in the most developed countries.

5.4.2 SB-SARBM3D

As described in Section 5.2, the first step of SARBM3D aims at estimating the local statistics of image intensity, which are used to drive the actual despeckling process performed in the second step. The quality of such estimates impacts heavily on the filter performance in terms of both speckle rejection and detail preservation. In this Ph.D. Thesis, we improve the estimation quality by using some prior information available on the sensed surface, interpreted through suitable scattering models, as discussed in Section 5.4. As a result, filtering performance improves significantly wherever the proposed scattering model is applicable, and notably in natural areas with gentle topography. In the following, the adopted scattering model and the proposed scattering-based version of SARBM3D are described in detail.

The previous Section provided insight into how the available information on the scene DEM can be converted, through appropriate scattering models, into an estimate, $\hat{\sigma}^0$, of the image NRCS. Our aim is to combine this information with the first-step estimate $\hat{x}_{1,SARBM3D}$ of SARBM3D to form a better pilot image for the second pass to work on, according to the relation

$$\hat{x}_{1,SB-SARBM3D} = f(\hat{x}_{1,SARBM3D}, \hat{\sigma}^0). \tag{5.12}$$

The problem becomes, therefore, the design of the most suitable combination function $f(\cdot,\cdot)$. To this end, it is worth reminding that the available prior information allows for an accurate description of the signal backscattered from natural areas with gentle topography or homogeneous flat regions, where surface scattering is the dominant phenomenon. On the contrary, the description is not reliable in correspondence to non-topographic edges, and in the presence of particular scattering phenomena, such as multiple bounce and volume scattering, typical of vegetated and urban areas. On the other hand, SARBM3D, even in the first step, guarantees mostly complementary properties. Edges, man-made regions and fine details are estimated faithfully, while limited speckle suppression is observed in homogeneous areas, together with some filtering artifacts due to block matching. Based on these observations, we define the function $f(\cdot,\cdot)$ so as to perform a simple weighted averaging of the two quantities (normalized to their mean values), with weights $w(s)$ that adapt pixel-wise to the local

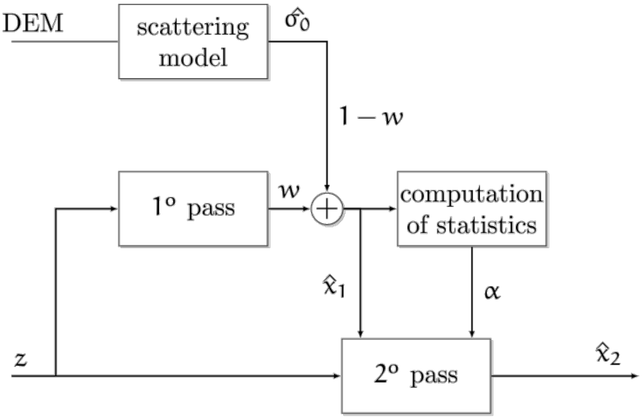

Figure 5.4. Block scheme of the scattering-based SARBM3D algorithm.

image content:

$$\hat{x}_{1,SB-SARBM3D}(s) = w(s)\hat{x}_{1,SARBM3D}(s) + (1-w(s))\hat{\sigma}^0(s). \qquad (5.13)$$

Accordingly, the block scheme of Fig. 5.1 is modified as shown in Fig. 5.4. As both Eq. 5.13 and the block scheme in Fig. 5.4 reveal, the proposed modification of SARBM3D is still applicable to both single and multilook SAR data, since the a priori scattering information is not affected by the number of looks of the SAR image. Consequently, the SB-SARBM3D filter inherits the applicability of the SARBM3D filter to both single and multilook SAR data. The weight w varies in the range $0-1$ adaptively across the image, combining in a suitable way the two contributes: large weights give more importance to the first-step SARBM3D estimate, $\hat{x}_{1,SARBM3D}$, while prior knowledge on scattering becomes dominant with small weights. Therefore, for what was previously stated, the weight is designed to be close to one in correspondence of non-topography-related edges and urban areas (if present), and close to zero in natural areas with gentle topography or homogeneous flat regions. Therefore, to define a sensible weight map, one has to identify beforehand non-topographic edges and man-made structures. To this aim, we apply to the input single-look SAR image the detectors proposed by Lopes *et al.* [17], [155] which identify relevant image features, such as edges, lines and point scatterers. To take into account the multiplicative nature of speckle, these detectors operate on local intensity ratios, rather than on the gradients considered in additive-noise contexts. Moreover, to reduce the effects of speckle, ratios are not computed between single-pixel values, but rather between averages taken over suitable windows in the neighborhood of the target pixel (the reader is referred to [17] and [155] for a more detailed description). In this Ph.D. Thesis, we use the very same windows defined in [155] for detecting edges, lines and strong scatterers. Even so, the output detection map appears to be quite noisy, with many false alarms and missed detections. To improve reliability we could enlarge the reference windows, but this would entail an unacceptable loss of spatial resolution. Instead, we resort here to the virtual multilooking technique introduced in [156] based itself on nonlocal estimation. For each patch of the single-look SAR image, a number of similar patches are collected over a large neighborhood, using block matching with the distance measure of Eq. 5.3. These are averaged together, with no loss of spatial resolution, to obtain a much cleaner patch to which the detectors of [155] are eventually applied. The output ratio map r_I takes values in the range $0-1$, as explained in [156], and provides reliable information on the image details. In order to reduce false alarms in the presence of topography (i.e., to separate non-topographic edges from those caused by terrain topography), we apply the same detector to the local incidence angle map, obviously without any virtual multilooking, obtaining a further ratio map r_θ in the range $0-1$. This step allows us to correctly identify non-topographic edges, man-made structures and homogeneous areas by evaluating the similarity between the two obtained maps r_I and r_θ: similar values reflect gentle topography or homogeneous flat regions; dissimilar values reflect the presence of non-topographic edges and/or man-made structures. Accordingly, the output weight map w is defined based on the similarity between r_I and r_θ:

$$w(s) = 1 - \min\left(\frac{r_I(s)}{r_\theta(s)}, \frac{r_\theta(s)}{r_I(s)}\right) \tag{5.14}$$

5.4.3 SB-PPB

Following the approach in [26], the nonlocal filter output is computed according to 5.6, and the filter weights are defined as the probability that the NRCSs of the two patches Δ_s and Δ_t are equal given an appropriate a priori knowledge. In particular, we introduce the scattering behavior of the resolution cell as an a priori knowledge. Accordingly, the following filter weight definition is proposed:

$$w_{s,t}^{non-it.SB-PPB} \triangleq p(\sigma_{\Delta_s} = \sigma_{\Delta_t} | A, \hat{\sigma}^{SPM})^{\frac{1}{h}} \tag{5.15}$$

with σ_{Δ_s} and σ_{Δ_t} being the NRCS in the selected (Δ_s) and test (Δ_t) patch and A being the amplitude SAR signal; $\hat{\sigma}^{SPM}$ takes into account the a priori information about the signal backscattered from the scene, and h is a parameter controlling the weight decay. By proceeding in a way similar to that of [26], we have

$$\begin{aligned} w_{s,t}^{non-it.SB-PPB} = \exp\Bigg[& -\frac{2L-1}{h} \sum_k \ln\left(\frac{A_{s,k}}{A_{t,k}} + \frac{A_{t,k}}{A_{s,k}}\right) \\ & + \frac{1}{h} \sum_k \ln p(\sigma_{s,k} = \sigma_{t,k} | \hat{\sigma}^{SPM})\Bigg]. \end{aligned} \tag{5.16}$$

Therefore, to properly take into account scattering, a description of the a priori probability $p(\sigma_{s,k} = \sigma_{t,k} | \hat{\sigma}^{SPM})$ is required. To this aim, we use the approach proposed in [26], thus modeling the a priori term via the symmetric version of the Kullback–Leibler divergence [26]

$$
\begin{aligned}
&p(\sigma_{s,k} = \sigma_{t,k} | \hat{\sigma}^{SPM}) \\
&\propto \exp\left\{ -\frac{1}{T_{fil}} \int \left[p\left(\sigma | \hat{\sigma}^{SPM}_{s,k}\right) - p\left(\sigma | \hat{\sigma}^{SPM}_{t,k}\right) \right] \ln \frac{p(\sigma | \hat{\sigma}^{SPM}_{s,k})}{p(\sigma | \hat{\sigma}^{SPM}_{t,k})} d\sigma \right\} \\
&\propto \exp\left(-L \frac{|\hat{\sigma}^{SPM}_{s,k} - \hat{\sigma}^{SPM}_{t,k}|^2}{\hat{\sigma}^{SPM}_{s,k} \hat{\sigma}^{SPM}_{t,k}} \right).
\end{aligned}
\tag{5.17}
$$

As a consequence

$$
\begin{aligned}
w^{non-it.SB-PPB}_{s,t} = \exp\Bigg[-\sum_k \Bigg(\frac{1}{\tilde{h}} \ln\left(\frac{A_{s,k}}{A_{t,k}} + \frac{A_{t,k}}{A_{s,k}} \right) \\
+ \frac{L}{T_{fil}} \frac{|\hat{\sigma}^{SPM}_{s,k} - \hat{\sigma}^{SPM}_{t,k}|^2}{\hat{\sigma}^{SPM}_{s,k} \hat{\sigma}^{SPM}_{t,k}} \Bigg) \Bigg]
\end{aligned}
\tag{5.18}
$$

Therefore

$$
w^{non-it.SB-PPB}_{s,t} = w^{non-it.PPB}_{s,t} \cdot \exp\left(-\sum_k \frac{L}{T_{fil}} \frac{|\hat{\sigma}^{SPM}_{s,k} - \hat{\sigma}^{SPM}_{t,k}|^2}{\hat{\sigma}^{SPM}_{s,k} \hat{\sigma}^{SPM}_{t,k}} \right).
\tag{5.19}
$$

Note that this equation is formally identical to 5.9, provided that the σ estimation at previous step $\hat{\sigma}^{i-1}$ is replaced by the σ value computed by the scattering model $\hat{\sigma}^{SPM}$. It is also worth noticing that 5.18 reduces to 5.10, i.e., to usual non-iterative PPB, for flat areas, because in this case $\hat{\sigma}^{SPM}_{s,k} = \hat{\sigma}^{SPM}_{t,k}$, so that $w^{non-it.SB-PPB}_{s,t} = w^{non-it.PPB}_{s,t}$. Evaluation of 5.18 via the expression in Eq. 2.15 requires the availability of a DEM of the sensed surface, so that the local incidence angle can be computed, and knowledge of the terrain complex relative dielectric constant, Hurst parameter, and spectral parameter. However, if the underlying topography is significant, the backscattered signal and, hence, SAR intensity variations are mostly due to the topographic content of the sensed surface, due to the major influence of the local incidence angle on the NRCS w.r.t. the remaining parameters (see the sensitivity analysis reported in Section 5.4.1). Accordingly, we can reasonably assume that S_0 is constant in the search window, so that it cancels out in 5.18; in addition, dependence on ε_r can be neglected, and a standard value can be used in Eq. 2.15, so that we can assume

$$\hat{\sigma}_p^{SPM} = \hat{\sigma}^{SPM}(\vartheta_p) \propto |\beta(\vartheta_p)|^2 \frac{\cos^4 \vartheta_p}{(\sin \vartheta_p)^{2+2H}} \tag{5.20}$$

where ϑ_p is the local incidence angle evaluated in the location p. With regard to the Hurst coefficient H, it can be estimated from the SAR image via the algorithm by Di Martino *et al.* [28], if one assumes that the same value of H holds at both macroscopic and microscopic scales. This is a rather strong assumption, but again, the sensitivity analysis in Section 5.4.1 shows that errors on the value of H do not appreciably affect scattering evaluation if a significant topography is present. Accordingly, in conclusion, evaluation of the weight 5.18 only requires availability of the scene DEM. In addition, as already mentioned, a uniform standard value of ε_r is assumed. However, this does not mean that the proposed filter is not applicable to different scenarios, where the scattering model is not accurate or ε_r is space-varying. In fact, together with the new distance term based on scattering, the weight used by our algorithm still retains the PPB distance term based on intensity (see 5.10 and 5.18), owing to which SB-PPB can be expected to work well also in regions in which the employed scattering model is not accurate. Further help with this regard is expected to be provided by the adoption of an adaptive scheme, as described in the following. The aforementioned expectations are confirmed by the experimental results of Section 5.5.

Adaptive Scheme

In order to fill the lack of a proper nonuniform a priori knowledge in the initial estimate, Deledalle *et al.* proposed also an iterative scheme within the PPB filter [26], with refined weights given by 5.9 (see Section 5.3). Iterations ensure a better preservation of edges and texture. It is then meaningful to discuss the use of this iterative scheme also for the proposed SB-PPB filter. It is noteworthy that, whenever topography represents the main contribution to the backscattering variations over the scene, an iterative scheme of the proposed technique does not provide relevant improvements since gray-level variations of the SAR image are already properly taken into account by the a priori knowledge about the local incidence angle (see Section 5.5 for an experimental verification). Nevertheless, in case of scenes presenting gentle topography and SAR image intensity variations not related to topography (i.e., related to variations of scene electromagnetic parameters, microscopic roughness or scattering phenomena not described by the proposed one, e.g., volume scattering typical of vegetated areas and double bounce, layover, and shadowing typical of urban areas), iterations can provide better edge and feature preservation capabilities w.r.t. the non-iterative version. In a realistic scenario, distinguishing the main source of the SAR intensity variations may not be an easy task. However, if a DEM of the sensed surface is available, it is possible to establish if the local topography is significant or not. Following this idea, a simple flat—nonflat binary classification-based adaptive iterative scheme of the proposed filter is proposed in this Ph.D. Thesis, based on the iterative PPB filter presented in [26]. Iterations are adaptively performed only in those regions characterized by a flat topography as explained in the next Section.

Filter Rationale

The rationale of the proposed adaptive SB-PPB filter is presented in the following. From the DEM of the sensed scene, the local incidence angle map can be easily computed from 5.11. In order to insert the a priori knowledge in the proposed filter, the local incidence angle map has to be projected into the SAR system geometry and coregistered to the noisy SAR image. This step is by now standard in SAR processing, and it can be easily performed by most of the available commercial software tools. The local incidence angle map is then divided in fixed-size blocks: each block undergoes a binary flat–nonflat classification process. A block is classified as flat if the standard deviation of the local incidence angle is less than a fixed threshold. SAR image blocks corresponding to nonflat regions undergo the non-iterative scheme of the proposed filter, i.e., filter weights defined by 5.18 are used. This corresponds to applying the PPB filter as introduced in [26] with a proper initial estimate provided by 5.20, in which the incidence angle computed via 5.11 is inserted. Conversely, in SAR image blocks corresponding to flat regions, the iterative scheme is employed, in order to refine weights in regions with non topography-related SAR intensity variations, such as edges, man-made features, etc., and improve the edge and feature preservation capability of the filter. In this case, after the first iteration, the a priori knowledge about topography is no more used, and it is substituted by the previous intensity estimate, exactly as in [26], i.e., the weights defined in 5.9 are used. The flowchart of the algorithm is shown in Fig. 5.5.

Finally, it is worth noticing that, apart from the H estimation and coregistration steps, whose computing time requirements are analyzed in the following sections, the adaptive SB-PPB filter has a complexity comparable to that of the PPB filter, the execution time depending on the flatness of the analyzed surface. In particular, the adaptive scheme allows for time saving in nonflat regions w.r.t. the iterative PPB, avoiding further iterations.

5.5 Experimental Results

Due to the lack of speckle-free SAR images, assessing the performance of despeckling algorithms is a difficult task. For this reason, numerous no-reference measures have been introduced to objectively evaluate the quality and accuracy of despeckling algorithms without resorting to reference images. Speckle rejection is easily measured through the Equivalent number of looks (ENL), computed in homogeneous areas of the image, but detail preservation is typically evaluated only qualitatively through visual inspection. However, on one hand, no-reference measures do not provide a complete understanding of the algorithm behavior and, on the other hand, actual SAR images are not useful to analyze algorithm performances in some meaningful canonical situations. Quantitative measures, however, can be obtained through simulation. To this end, a common approach is to inject speckle on optical images, but these simulated SAR images differ profoundly from the real-world ones, leading to measures that may have little sense. To solve these problems, a benchmarking framework for despeckling was recently proposed in [145], where a physical-based SAR raw signal and image simulator [157] is used to generate realistic SAR images. For some selected canonical scenes, an arbitrary number of single-look realizations can be generated, allowing one to obtain a virtually speckle-free reference by temporal multilooking. We will follow this approach, here, and consider three relevant scenes, computing for each one several objective measures of performance. These simulated scenes enable the numerical comparison between different techniques, providing solid insight into the main advantages and disadvantages of each one. Therefore, we will use them in the next Section to analyze the improvements granted over the original SARBM3D and PPB filters by the proposed scattering-based ver-

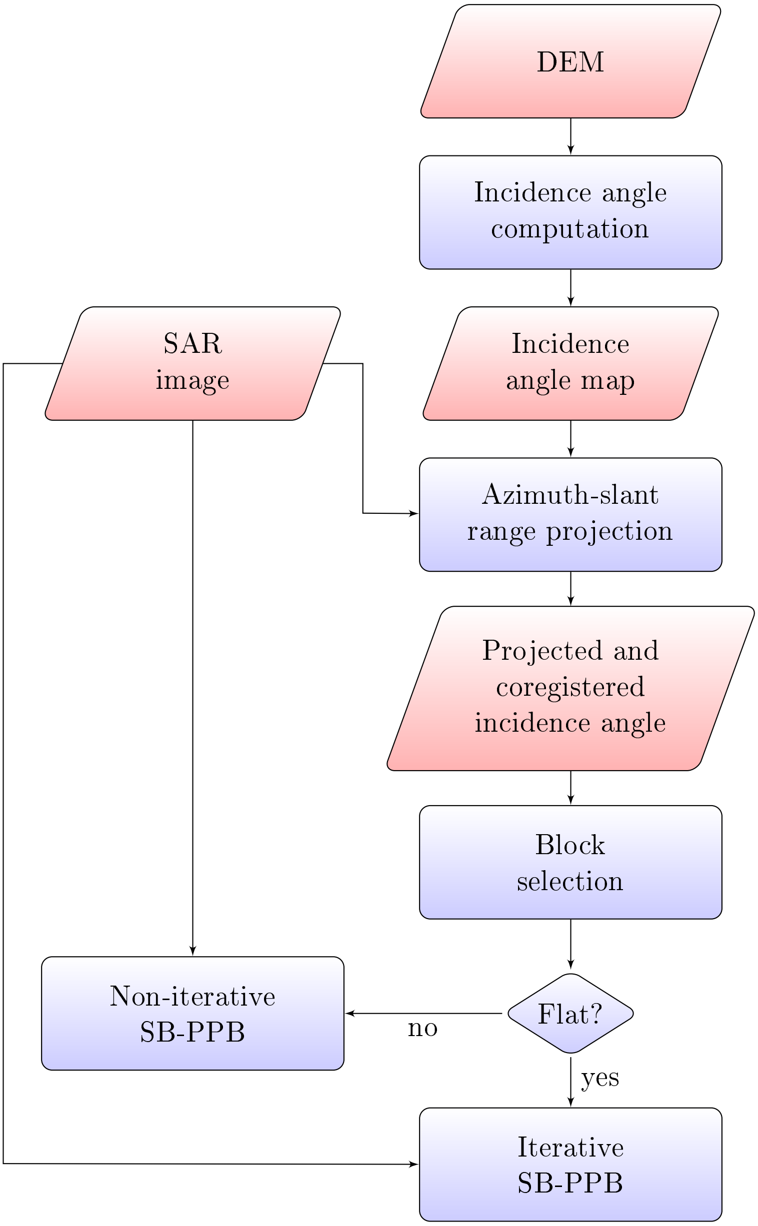

Figure 5.5. Flowchart of the proposed SB-PPB filter. Iterations are adaptively performed only on flat areas, identified through a binary classification method based on the local incidence angle map.

sions. Regarding the PPB filter, both the non-iterative and 4-iterative versions are used for comparison. Then, in the last part of the Section, we will analyze performance using real-world SAR images. In this case, apart from some basic numerical measures, we will rely mostly on visual inspection to assess despeckling quality.

Default filter parameters defined in [24] and [26] are used for PPB and SARBM3D, respectively. For the proposed SB-PPB filter we use the same values of the parameters used for PPB, apart from the T_{fil} parameter that, only in the first iteration, assumes a different values in order to take into account the different kind of a priori information. In this case, best results are obtained setting it equal to 1.3. Whenever iterations are performed, the default PPB value for T_{fil} is used. The binary classification is performed subdividing the image in distinct blocks of 256×256 pixels size and evaluating the standard deviation of the local incidence angle map: a region is classified as flat if the standard deviation of the incidence angle is sufficiently low. We empirically set a threshold of 2°. Furthermore, a search window size of 21×21 and a patch size of 7×7 are used both for the SB-PPB and PPB filters, while a search window size of 39×39 is used for the SARBM3D filter.

Performance evaluation is carried out by computing some of the objective measures proposed in [145]. In particular, besides the well-known ENL, the mean of intensity (MoI) accounts for possible biases in the output, the variance of ratio (VoR) gives indication on under- and over-smoothing phenomena, edge smearing (ES) and correlation index (C_x) provide information on the preservation of edges and textures, respectively, while the SNR, and the mean structure-similarity index (MSSIM) are well-known global measures of distortion (the reader is referred to [145] and [158] for the definition and detailed description of these performance parameters). Since each parameter is intended to evaluate performance w.r.t. specific aspects of the algorithm or the scene, in each experiment a subset of the aforementioned parameters is used, as explicitly indicated both in the text and in the Tables. Finally, in order to provide information about the computational load of the proposed algorithms, the runtime is computed. All experiments have been carried out on a 3 GHz dual-core workstation equipped with a 8 GB RAM.

5.5.1 Canonical Study Cases

In order to test the proposed scattering-based despeckling algorithms in different scenarios, three suitable scenes are defined, and the corresponding SAR images are generated by means of the SARAS simulator [157]. The first one is a sinusoidal DEM, with constant geometrical and electromagnetic parameters (Fig. 5.6). The second scenario (Fig. 5.7) is characterized by a cone-shaped DEM with an aperture angle of 160°.

In order to test the effectiveness of the adaptive procedure of SB-PPB and the weight evaluation in SB-SARBM3D, the proposed algorithms are also applied to a more realistic scenario in which both topography- and non-topography-induced SAR intensity variations are present. This mixed scene is considered in the third case characterized by a fractal DEM with constant parameters on the right-side, and four square patches with flat DEM and different electromagnetic parameters on the left-side (Fig. 5.8).

For the entire simulated dataset, the following parameter values have been used: $H = 0.8$, $T = 10^{-4}$ m, $\varepsilon_r = 4$, $\sigma_c = 10^{-2}$ S/m. The four flat patches of the mixed scenario, instead, have electromagnetic parameters (clockwise from top-left): $\varepsilon_r = 10$, $\sigma_c = 10^{-2}$ S/m; $\varepsilon_r = 4$, $\sigma_c = 10^{-3}$ S/m; $\varepsilon_r = 4$, $\sigma_c = 10^{-3}$ S/m; $\varepsilon_r = 80$, $\sigma_c = 4$ S/m, the second and the third patches sharing the same electromagnetic parameters. The fBm DEM presents the same fractal parameters values also at macroscopic scales. The parameters of the SARAS simulator are set so as to generate images with the same characteristics as those acquired by the COSMO-SkyMed sensor [159]. Consistently with the proposed theoretical approach, the backscattered signal has been simulated using the SPM option of SARAS.

Performance evaluation is carried out computing proper metrics in each case. In particular, MoI, VoR, SNR, and MSSIM are evaluated in all cases; the ENL is properly evaluated in the cone and mixed cases, while the coefficient of variation C_x is computed in the fractal and sinusoidal cases to evaluate the textural preservation capability of the despeckling filters. Finally, the edge smearing parameter is evaluated in the mixed scenario since sharp edges occur in this case.

All test images have a size of 512×512 pixels, and for each scene 512 independent single-look realizations are generated. By averaging them, a 512-look image is obtained, which is almost speckle-free and represents therefore a good basis to compute full-reference quality measures.

Experimental results are depicted in Figs. 5.6-5.8, in which it is shown the single-look SAR image (a), the 512-look reference (b), the local incidence angle (c), the despeckled images using non-iterative PPB (d), PPB with four iterations (e), SARBM3D (f), SB-PPB (g), SB-SARBM3D (h), and the SB-SARBM3D weight map (i).

The proposed algorithms rely on the prior scattering information evaluated via Eq. 2.15 from the local incidence angle map and used for the first-step estimate in SB-SARBM3D (see Eq. 5.13) and for the filter weights computation in SB-PPB (see Eq. 5.18).

Finally, it is worth underlining that, although the scattering model in Eq. 2.15 is able to take into account also non-topographic inhomogeneities of the sensed surface, such as changes of the dielectric constant or the microscopic roughness, this information is not taken into account in the proposed scattering-based filters. In this way, we simulate a more realistic configuration characterized by the lack of prior knowledge on such parameters. To summarize, for the entire simulated dataset, the a priori scattering information is estimated from the local incidence angle map and assuming the following parameter values: $H = 0.8$, $T = 10^{-4}$ m, $\varepsilon_r = 4$, $\sigma_c = 10^{-2}$

S/m. Then, the inhomogeneities of the relative dielectric constant in the mixed scenario are not accounted for in the proposed despeckling filters.

In presence of a continuously varying SAR image intensity, as in the sinusoidal and cone cases, SARBM3D exhibits some clear artifacts [see Figs. 5.6(f) and 5.7(f)] that greatly affect the output image quality. The prior information about scattering reduces dramatically these artifacts [see Figs. 5.6(h) and 5.7(h)], improving significantly the image quality. In fact, these artifacts are due to random speckle patterns in the input image that are reinforced by nonlocal filtering. Of course, no such patterns exist in the local incidence angle map. Consequently, the scattering contribution in Eq. 5.13 prevails in the first-pass estimate, since the homogeneity of geometrical and electromagnetic parameters, and the absence of man-made structures, give rise to a weight map [Fig. 5.6(i)] with values uniformly close to zero. The objective performance indicators reported in Table 5.1 confirm these considerations. The proposed SB-SARBM3D filter improves significantly w.r.t. the original version in terms of VoR and SNR (more than 3 dB in the first scenario), while very close values are observed for C_x, which makes sense given the absence of texture, and MSSIM, which is little affected by local artifacts.

The slow-varying topography justifies the similarity in the performances of the proposed SB-PPB technique [Fig. 5.6(g)] and the PPB filter [Fig. 5.6(d)-(e)], as shown both visually and quantitatively (see Table 5.1), in preserving the continuous spatial variation of the SAR image intensity. The absence of rapid variations in the image ensures an extremely fast convergence of PPB, i.e. iterations do not provide a significant improvement w.r.t. the non-iterative PPB.

In the more realistic mixed scene, both topography- and non-topography-related variations in SAR intensity are present. This scene was designed to evaluate the behavior of the proposed algorithms in different situations, such as homogeneous areas, edges and topography. As expected, SARBM3D provides a very good edge and texture preservation [see Fig. 5.8(f)] thanks to the nonlocal approach, while visible artifacts appear, again, in the homogeneous areas, especially in regions close to the edges. In these areas, the DEM-based prior information allows for a much better speckle suppression, increasing the ENL from about 300 for SARBM3D to over 1900 for SB-SARBM3D (see Table 5.3). Because of the assumed lack of information about the variations of electromagnetic parameters, the scattering-based contribution in SB-SARBM3D does not "see" the edges in the left side of the image. This might potentially cause a significant edge smearing. However, these edges are well captured by the ratio edge detector operating on the input SAR image, leading to large values of the weight in correspondence of the edges [see Fig. 5.8(i)]. Therefore, the first-step estimate of SARBM3D greatly contributes to the first-step estimate of SB-SARBM3D in correspondence of the edges, leading to a similar ES value (see Table 5.3). The SNR figure confirms the overall improvement of the proposed filter w.r.t. SARBM3D, thanks to the a priori scattering information.

The knowledge of the underlying topography is responsible for a huge improvement of the despeckling capability of the PPB filter, as Fig. 5.8(d) and Fig. 5.8(g) show, also considering its iterative version [Fig. 5.8(e)]. As shown in Table 5.3, thanks to the a priori knowledge of the local incidence angle map, the proposed SB-PPB filter provides better results, in terms of SNR, w.r.t. the original PPB filter and SARBM3D as well. It provides also a preservation of the textural content of the sensed scene that is better w.r.t. the non-iterative PPB and comparable to the SARBM3D, as demonstrated by the coefficient of variation and the structural similarity index. This scenario clarifies the key role of the adaptive scheme proposed in the SB-PPB algorithm in retrieving the edge preservation capabilities ensured by iterations. In the left part, where non-topography-induced intensity variations are present, the lack of a priori knowledge about electromag-

Table 5.1. Performance parameters for the sinusoidal DEM

	MoI	VoR	SNR	C_x	MSSIM	Runtime (s)
Reference	1.000	0.997	∞	0.860	1.000	-
Noisy	1.000	-	-3.693	1.572	0.970	-
PPB nonit.	0.998	0.819	17.192	0.848	0.999	14.04
PPB 4-it.	0.999	0.820	16.921	0.852	0.999	54.60
SARBM3D	0.985	0.858	16.045	0.862	0.999	136.65
SB-PPB	0.998	0.823	17.286	0.849	1.000	15.13
SB-SARBM3D	0.986	0.993	19.155	0.852	1.000	512.76

netic parameters variations makes the edges to be largely smoothed if no iterations would occur in the SB-PPB filter: in this case, iterations are needed to enhance edge preservation capability. To this aim, the proposed adaptive scheme introduces iterations in a smart and adaptive way only in those regions where non-topography-related SAR intensity variations are present. In this case, the adaptive scheme performs iterations only in the left part of the image [Fig. 5.8(g)], thus greatly reducing the execution time w.r.t. a pure iterative scheme, in which iterations are performed on the whole image. The adaptive scheme allows the SB-PPB to outperform the non-iterative PPB in terms of edge preservation, thus providing results similar to the iterative PPB (see the ES parameter in Table 5.3). In particular, the adaptive SB-PPB ensures the same detail preservation as the non-iterative SB-PPB in the non-flat region (see the C_x parameter) and a comparable edge preservation as the iterative SB-PPB in the flat one (see the ES parameter).

5.5.2 Actual Cases

The proposed algorithms have also been applied to two subsets of an actual single-look stripmap COSMO-SkyMed SAR image acquired over the Vesuvius-Mt. Somma complex close to Naples, Italy, on August 3, 2011. The first image is 2000 × 2000 pixels and is relevant to a natural

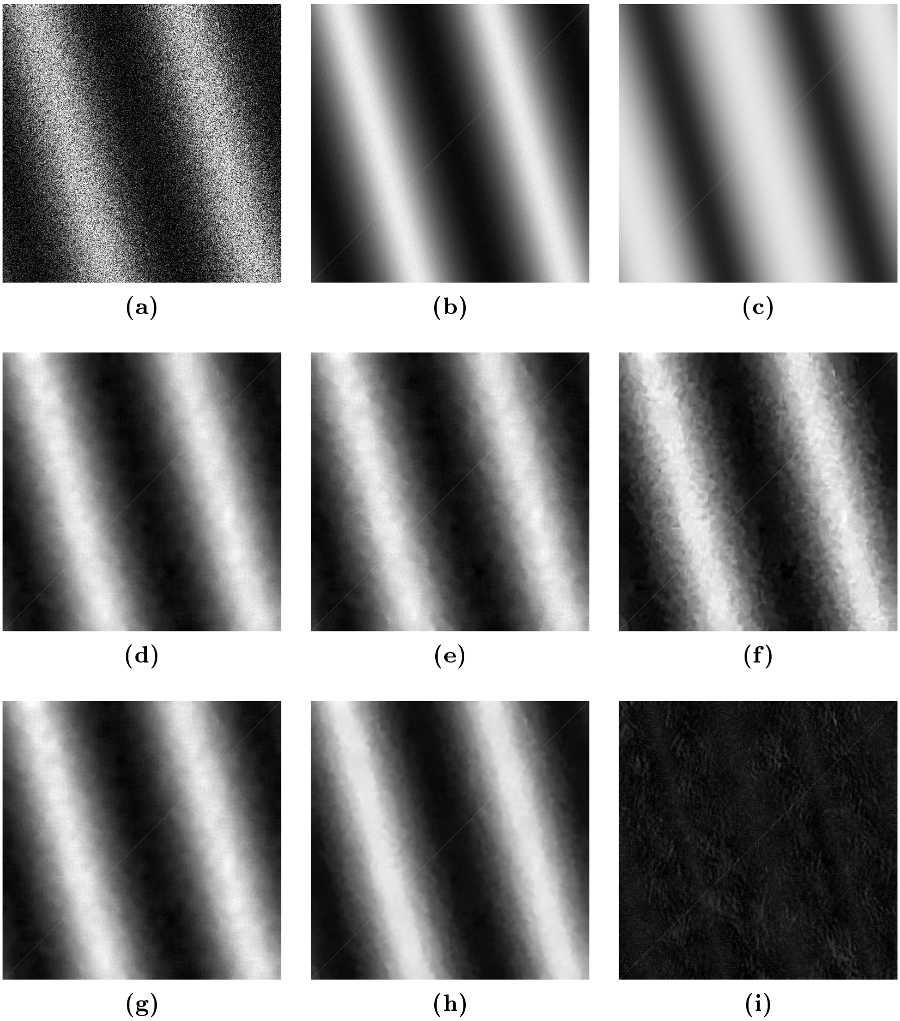
(a) (b) (c)

(d) (e) (f)

(g) (h) (i)

Figure 5.6. (a) 512×512 simulated single-look SAR image in presence of a sinusoidal topography, microscopic roughness of fractal parameters $H = 0.8$ and $T = 10^{-4}$ m, and electromagnetic parameters $\varepsilon_r = 4$ and $\sigma_c = 10^{-2}$ S/m; (b) 512-look reference image; (c) local incidence angle map; (d) PPB nonit.; (e) PPB 4-it.; (f) SARBM3D; (g) SB-PPB; (h) SB-SARBM3D; (i) weight map in the range 0-1.

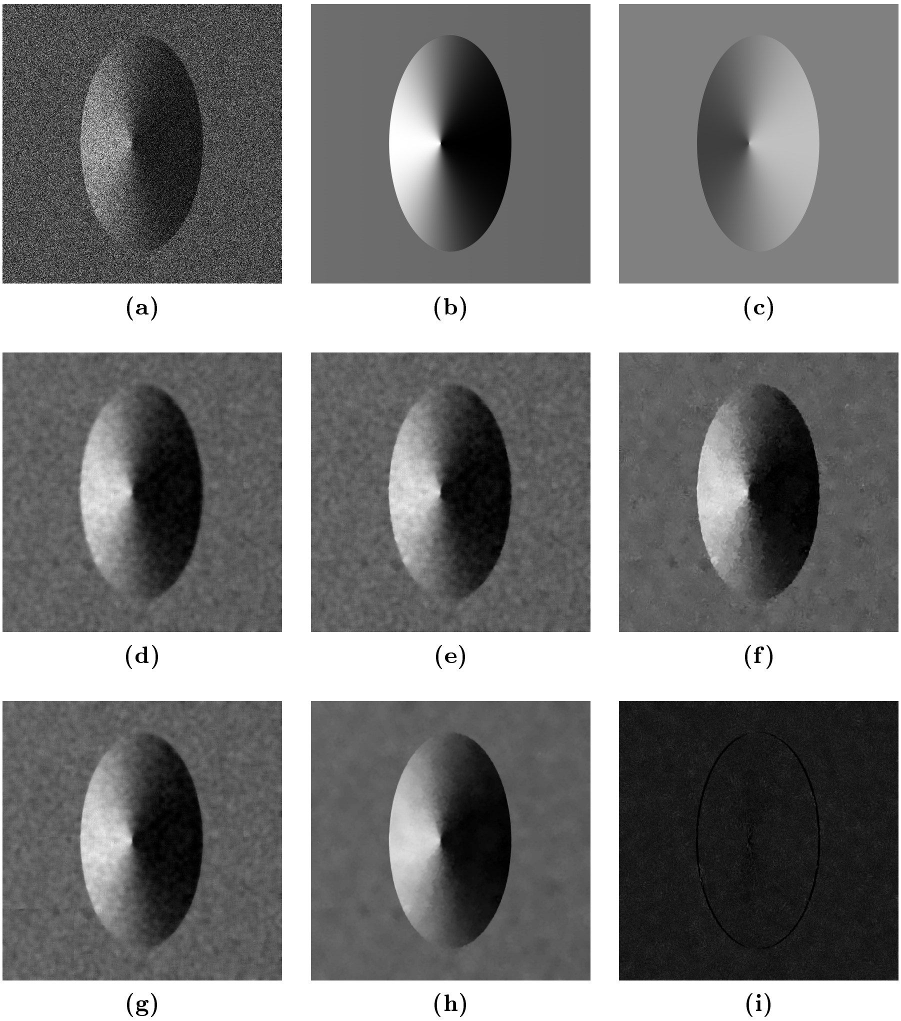

Figure 5.7. (a) 512×512 simulated single-look SAR image in presence of a conical topography with microscopic roughness of fractal parameters $H = 0.8$ and $T = 10^{-4}$ m, and electromagnetic parameters $\varepsilon_r = 4$ and $\sigma_c = 10^{-2}$ S/m; (b) 512-look reference image; (c) local incidence angle map; (d) PPB nonit.; (e) PPB 4-it.; (f) SARBM3D; (g) SB-PPB; (h) SB-SARBM3D; (i) weight map in the range 0-1.

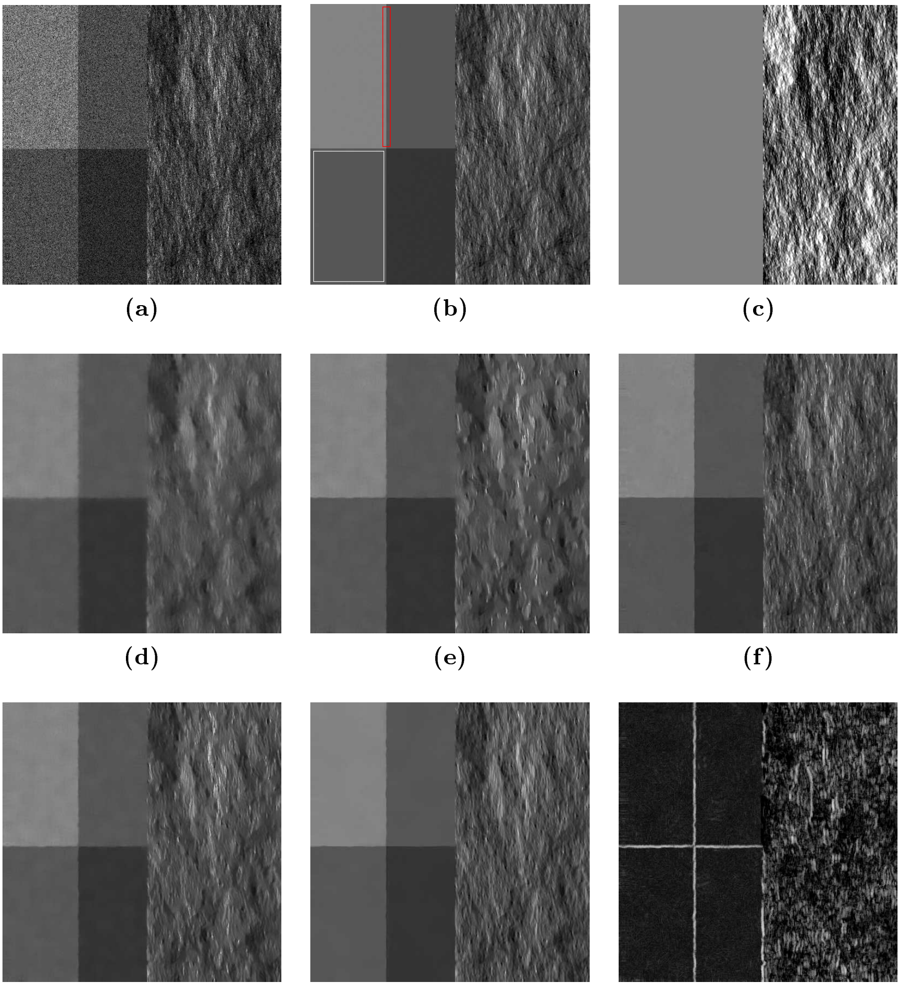
(a) (b) (c)

(d) (e) (f)

(g) (h) (i)

Figure 5.8. (a) 512 × 512 simulated single-look SAR image in presence of a fBm topography of fractal parameters $H = 0.8$ and $T = 10^{-4}$ m, and electromagnetic parameters $\varepsilon_r = 4$ and $\sigma_c = 10^{-2}$ S/m (right) and patches of different electromagnetic parameters - in particular, the brightest square simulates damp soil ($\varepsilon_r = 10$, $\sigma_c = 10^{-2}$ S/m), the middle gray-level squares dry soil ($\varepsilon_r = 4$, $\sigma_c = 10^{-3}$ S/m) and the darkest one sea ($\varepsilon_r = 80$, $\sigma_c = 4$ S/m); (b) 512-look reference image; (c) local incidence angle map; (d) SARBM3D; (e) PPB nonit.; (f) PPB 4-it.; (g) SB-SARBM3D; (h) SB-PPB; (i) weight map in the range 0-1. White box indicates the region where the ENL is computed; ES evaluation is performed in the red marked area consisting of 240 horizontal profiles.

Table 5.2. Performance parameters for the cone DEM

	MoI	VoR	SNR	ENL	MSSIM	Runtime (s)
Reference	1.000	0.856	∞	47713.988	1.000	-
Noisy	0.903	-	-7.343	1.012	0.980	-
PPB nonit.	0.902	0.830	7.542	176.143	0.998	51.07
PPB 4-it.	0.903	0.829	7.671	173.390	0.998	206.77
SARBM3D	0.889	0.888	7.609	442.865	0.998	529.47
SB-PPB	0.903	0.832	7.695	171.473	0.998	86.40
SB-SARBM3D	0.891	1.012	7.942	1562.597	0.998	1681.47

Table 5.3. Performance parameters for the mixed DEM

	MoI	VoR	SNR	C_x	ES	MSSIM	ENL	Runtime (s)
Reference	1.000	1.003	∞	1.899	0.000	1.000	503.79	-
Noisy	0.997	-	-1.874	2.777	0.025	0.965	0.98	-
PPB nonit.	0.966	1.104	4.583	0.861	0.291	0.989	180.82	14.28
PPB 4-it.	0.979	0.943	6.365	1.569	0.092	0.993	178.78	55.69
SARBM3D	0.967	0.724	6.919	1.778	0.060	0.995	319.91	134.52
SB-PPB	0.978	0.817	7.457	1.625	0.101	0.995	176.06	31.65
SB-SARBM3D	0.963	0.892	7.813	1.390	0.075	0.996	1901.47	464.14

area with some sparse man-made objects [Fig. 5.9(a)]; the second subset is 1000 × 1000 pixels and is relevant to a partly urbanized area at the foot of the Vesuvius mountain [Fig. 5.12(a)]. The radar look-angle is 44°, while the pixel spacing is 2.07 m and 1.17 m in azimuth and slant range, respectively; the operating frequency is 9.6 GHz.

For what concerns the natural scenario, a 42-look SAR image obtained via temporal multilook is used as reference [Fig. 5.9(b)], while the mixed scenario in Fig. 5.12 deserves a specific comment. Indeed, due to the fast temporal changes characterizing an urban scenario (mainly due to the presence of vehicles) and the high resolution of the COSMO-SkyMed sensor, some differences - likely not related to speckle - between the single-look and the 42-look images are present, as in the red circles in the zoomed region in Fig. 5.13(a),(b). Consequently, the 42-look image is not a suitable reference image and no synthetic parameters are evaluated for this scenario. Indeed, only a visual inspection is conducted for the quality assessment of the filters.

The local incidence angle maps [Fig. 5.9(c) and Fig. 5.12(c)] are obtained from a DEM acquired with a Lidar system. The DEM employed is publicly available at no cost at the Naples (Italy) local authority website [160].

Figure 5.9(d)-(f) and Fig. 5.12(d)-(f) show the PPB nonit., PPB with four iterations, and SARBM3D, respectively; the proposed filters outputs for the natural and urban scenarios are shown in Fig. 5.9(g)-(h) and Fig. 5.12(g)-(h), respectively; Figures 5.9(i) and 5.12(i) show the weight maps relevant to the SB-SARBM3D algorithm.

The Hurst exponent has been evaluated through the algorithm proposed by Di Martino in [28]. In order to evaluate the texture preservation capability for the natural scenario, the coefficient of variation is computed on a uniformly textured region of the Mt. Somma [black box in Fig. 5.9(b)].

For what concerns the natural scenario, despite the absence of non-topographic edges, the image presents some brilliant points to be preserved. As the weight map shows, the proposed ratio detector correctly identifies most of them, penalizing the scattering model with a high weight. Due to the strong topography and geometric distortion (layover and shadowing), the ratio detector provides some false alarms identifying also topographic edges in correspondence of the crater and the Mt. Somma ripples.

Despite an overall similarity between the SARBM3D and its scattering-based version outputs, zooms in Fig. 5.10 and Fig. 5.11 show the better reliability of SB-SARBM3D result especially in terms of removal of the artifacts that affect the SARBM3D filter. In particular, the SARBM3D despeckled image presents repetitive horizontal and vertical structures not present in the reference that could significantly affect a correct data interpretation. The a priori scattering information allows for a significant reduction of these artifacts. Unfortunately, synthetic parameters are not yet able to reward artifacts removal. A better smoothing is reached by the SB-SARBM3D filter, as witnessed by the VoR parameter in Table 5.4.

Finally, the SB-SARBM3D filter presents better speckle reduction in homogeneous areas as shown by the higher ENL computed in the white box of Fig. 5.10(a).

The a priori knowledge on the scattering behavior of the resolution cell allows a better speckle rejection in SB-PPB w.r.t. PPB without losing details. Hence, as shown in the two subsets in Fig. 5.10 and Fig. 5.11, the PPB filter provides an oversmoothed image, in which many features and details are strongly attenuated. A simple visual inspection clarifies the benefits derived from an accurate modelization of the electromagnetic properties of the illuminated surface. A good texture preservation of SB-PPB, as well as the oversmoothing performed by PPB, is confirmed by the C_x parameter in Table 5.4.

The suburban scenario depicted in Fig. 5.12 shows the behavior of the proposed despeckling algorithms in a partly man-made scenario in which, together with the single-bounce diffusion, other scattering phenomena - not taken into account within the proposed scattering model - occur, such as multiple-bounce scattering. Reasonably, in such a scenario, the SB-SARBM3D filter assigns a major weight to the SARBM3D first-step estimate, except the natural area in the right-up corner, as the weight map in Fig. 5.12(i) shows. Consequently, SB-SARBM3D inherits most of the detail preservation capability of SARBM3D in the urban area [see Fig. 5.13(h)], in which the proposed scattering model is not adequate.

Even in this case, SB-PPB provides a more detailed image w.r.t. the original PPB filter, as clearly visible in the zoomed area in Fig. 5.13(f).

In conclusion, this scenario preannounces some robustness properties of the proposed scattering-based filters against the scattering behavior of the illuminated surface. A deeper sensitivity analysis is conducted in the next Section.

A last remark about computational complexity of SB-SARBM3D is in order. Due to the additional steps of weights evaluation, DEM projection and Hurst coefficient evaluation, the proposed SB-SARBM3D presents a computational load larger than the original SARBM3D filter. In particular, for all the experiments run, the proposed SB-SARBM3D requires about four times the computational time of SARBM3D. The increase of computational time is mainly due to the weight evaluation phase.

5.6 Sensitivity Analysis of SB-SARBM3D and SB-PPB

In this Section, a comprehensive experimental sensitivity analysis of the proposed scattering-based despeckling algorithms is carried out and the main results are presented and discussed. First, in Section 5.6.1, the influence of the scattering behavior of the surface is analyzed by applying

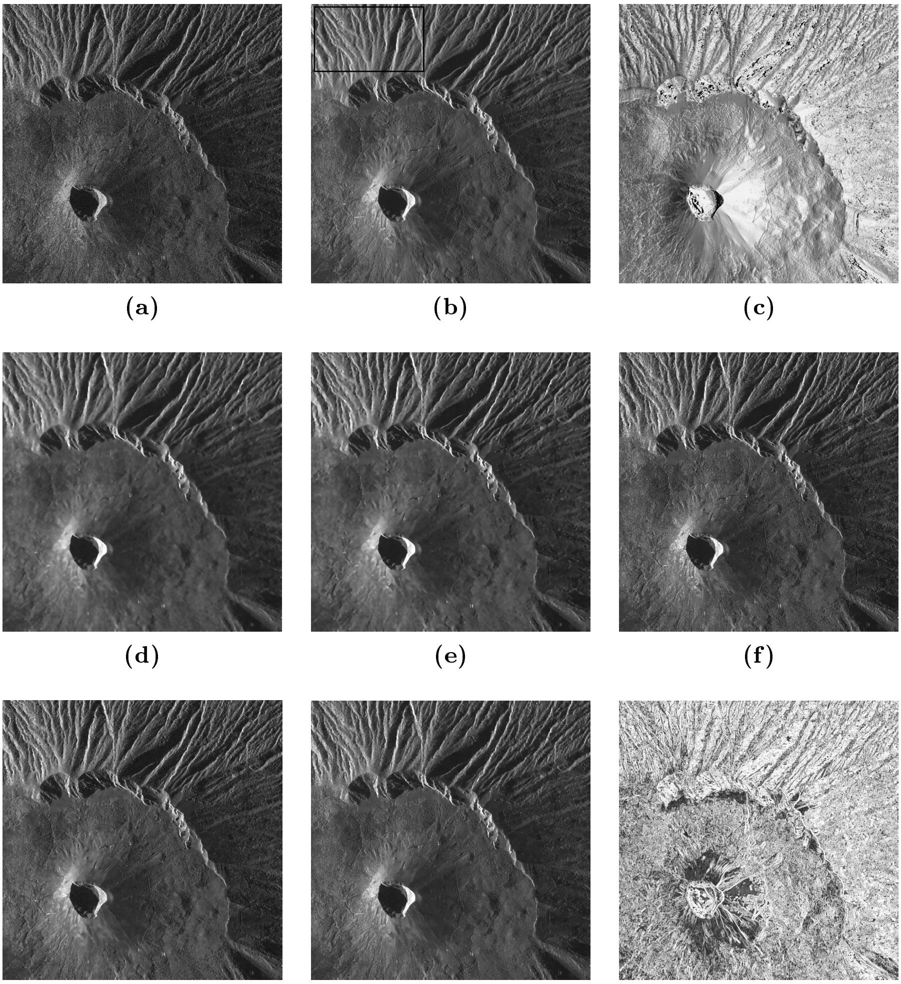
(a) (b) (c)

(d) (e) (f)

(g) (h) (i)

Figure 5.9. (a) 2000 × 2000 subset of a COSMO-SkyMed single-look stripmap SAR image of the Vesuvius volcano close to Naples (Italy); (b) reference image obtained via a temporal multilook of 42 SAR images. The black box indicates the area selected for coefficient of variation computation; (c) local incidence angle in azimuth-slant range derived from a DEM obtained with a Lidar system; (d) PPB nonit.; (e) PPB 4-it.; (f) SARBM3D; (g) SB-PPB; (h) SB-SARBM3D; (i) weight map in the range 0-1;

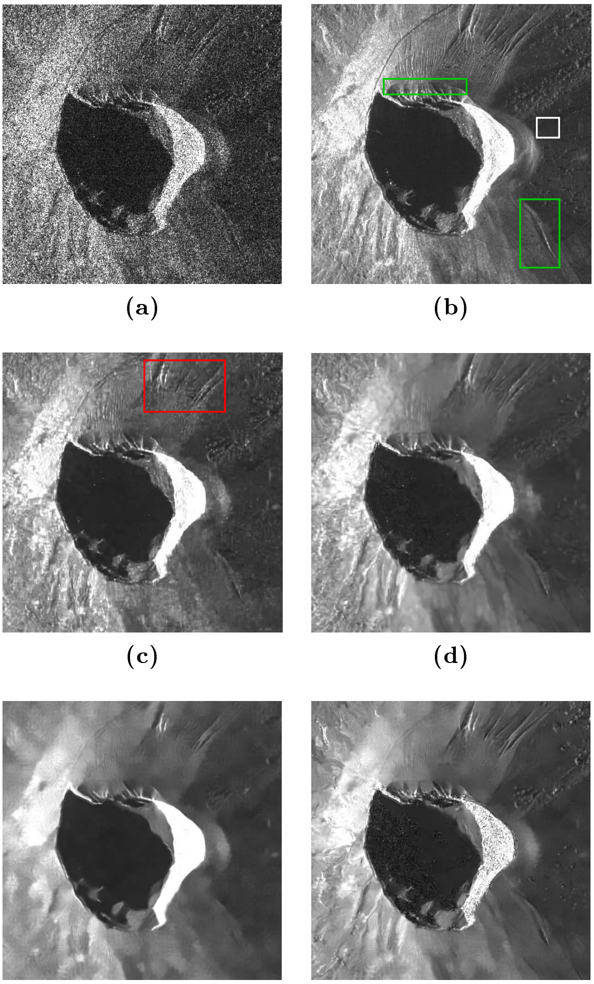

(a) (b) (c) (d) (e) (f)

Figure 5.10. 500×500 zoom of the Vesuvius crater: (a) Noisy; (b) reference; (c) SARBM3D. Red box indicates some artifacts removed or attenuated in SB-SARBM3D. (d) SB-SARBM3D; (e) PPB with four iterations; (f) SB-PPB. Green boxes indicate some features better preserved thanks to the a priori scattering information; white box indicates the region where the ENL is computed.

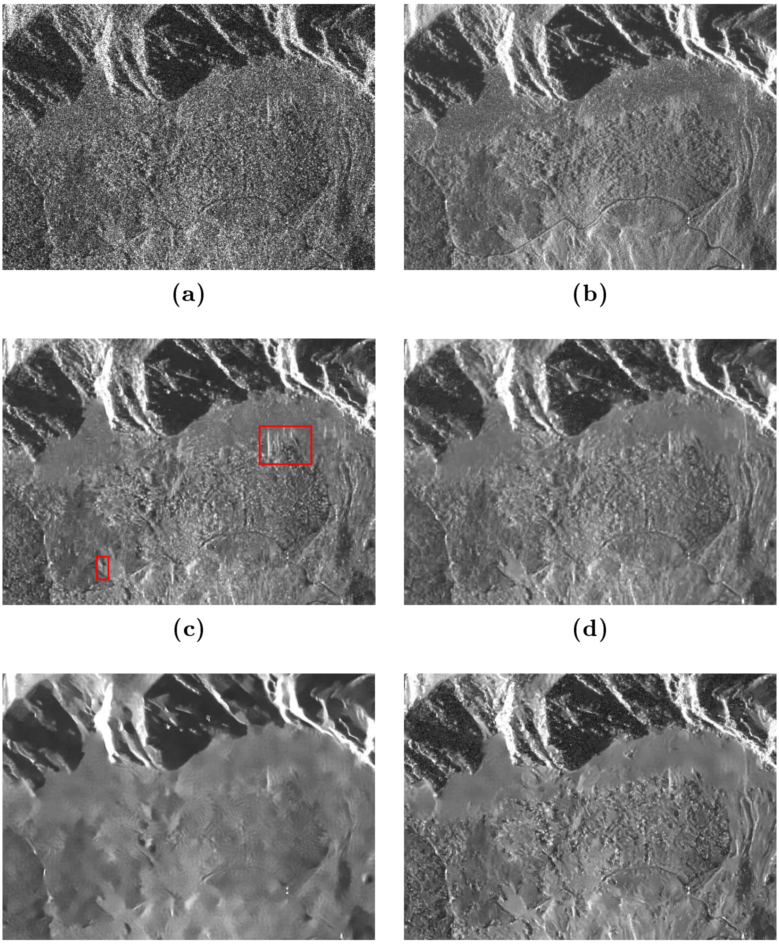
(a) (b)

(c) (d)

(e) (f)

Figure 5.11. 500 × 700 zoom of a flat region at the foot of the Vesuvius: (a) Noisy; (b) reference; (c) SARBM3D. Red boxes indicate some artifacts removed or attenuated in SB-SARBM3D. (d) SB-SARBM3D; (e) PPB with four iterations; (f) SB-PPB.

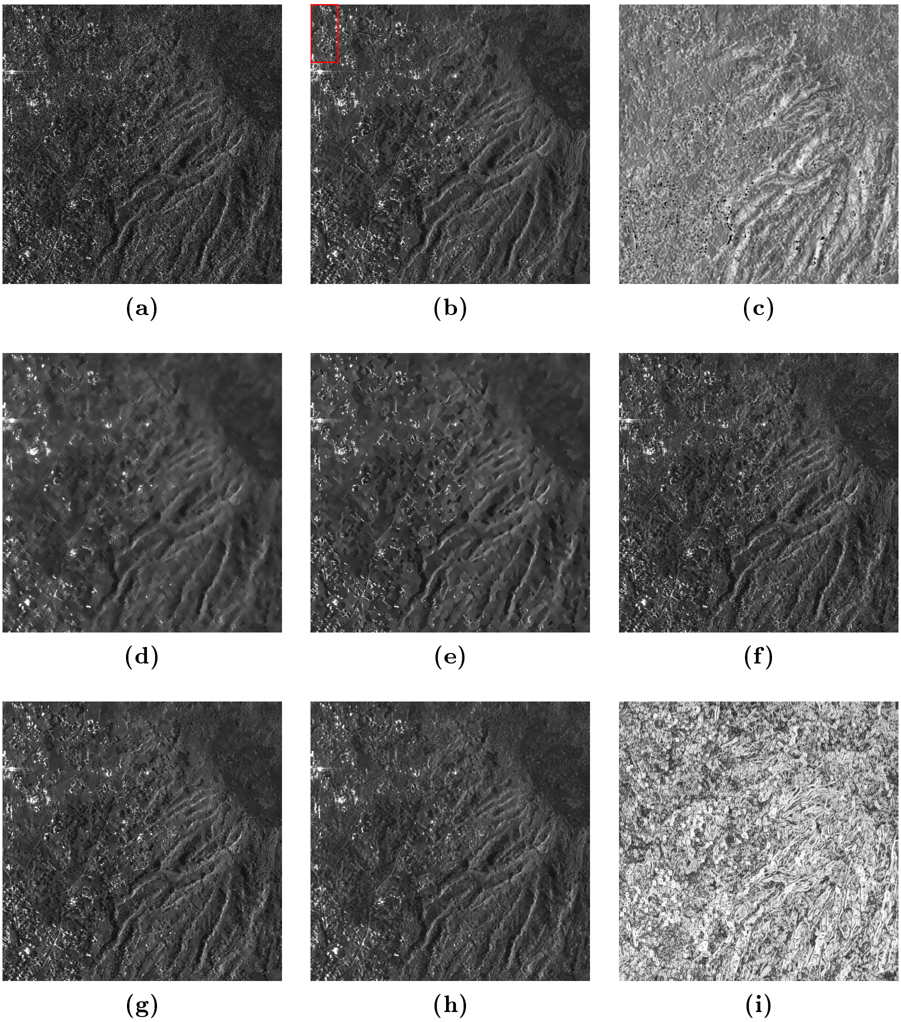

Figure 5.12. (a) 1000 × 1000 subset of a COSMO-SkyMed single-look stripmap SAR image of the Vesuvius volcano close to Naples (Italy) and relevant to a partly urbanized area; (b) image obtained via a temporal multilook of 42 SAR images. (c) Local incidence angle in azimuth-slant range derived from a DEM obtained with a Lidar system. (d) PPB nonit.; (e) PPB 4-it.; (f) SARBM3D; (g) SB-PPB; (h) SB-SARBM3D. (i) Weight map in the range 0-1. Red marked area is zoomed in Fig. 5.13.

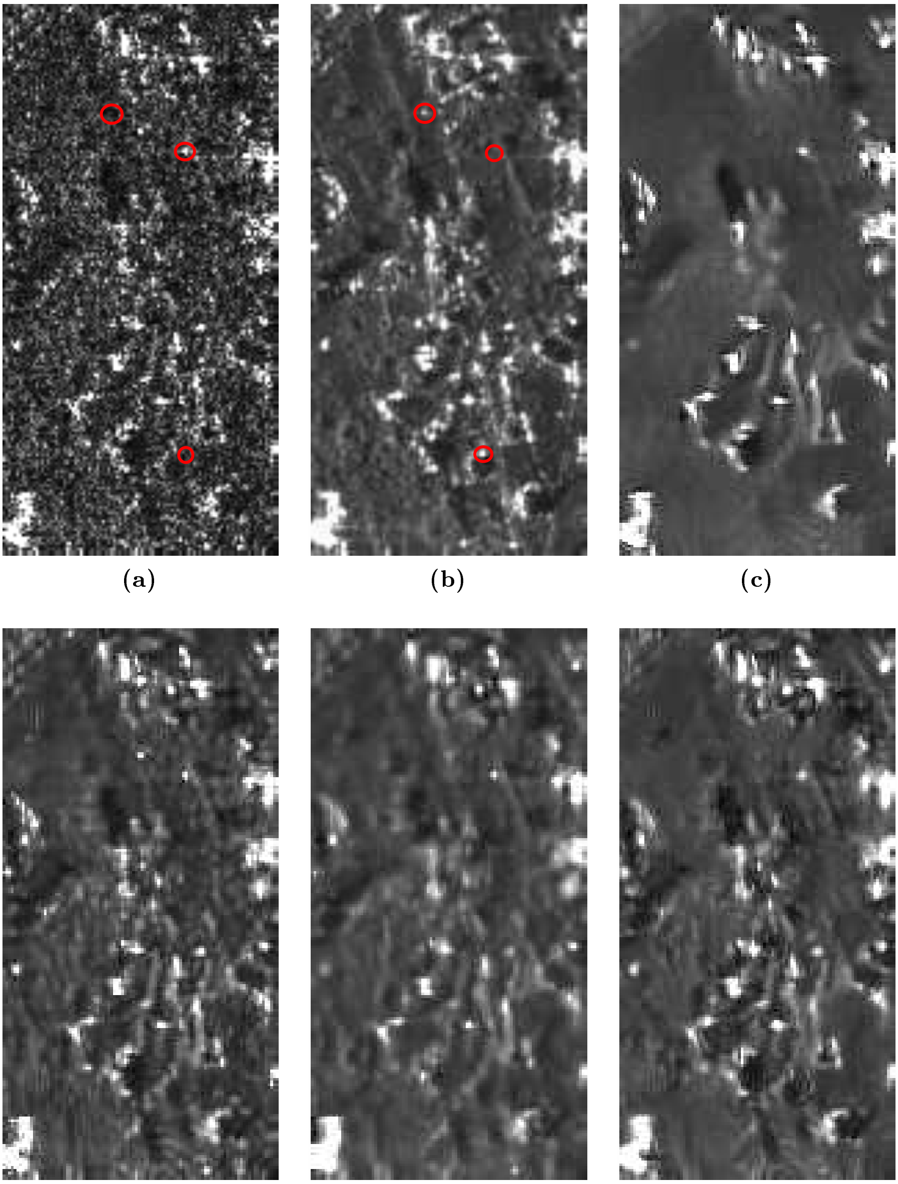
(a) (b) (c)

(d) (e) (f)

Figure 5.13. Zoom of the red marked area in Fig. 5.12(b). (a) Single-look; (b) 42-look image; (c) PPB 4-it.; (d) SARBM3D; (e) SB-SARBM3D; (f) SB-PPB. Differences between the single and the multilook images are red circled.

Table 5.4. Performance parameters for the actual image of a natural scene

	MoI	VoR	SNR	C_x	ES	MSSIM	ENL	Runtime (s)
Reference	1.000	1.312	∞	1.054	0.000	1.000	19.70	-
Noisy	1.000	-	-1.470	1.795	0.600	0.962	0.93	-
PPB nonit.	0.980	1.077	4.437	0.784	0.455	0.991	66.29	204.24
PPB 4-it.	0.984	1.026	5.747	0.902	0.357	0.991	66.02	839.98
SARBM3D	0.970	0.607	5.131	1.052	0.293	0.989	52.18	2082.85
SB-PPB	0.997	0.728	3.861	1.075	0.555	0.989	66.63	264.26
SB-SARBM3D	0.973	0.818	5.139	0.958	0.237	0.991	72.44	8597.62

SB-SARBM3D and SB-PPB to SAR images simulated via different scattering models. Section 5.6.2 deals with the influence of surface parameters on the despeckling capability of the filters. To this aim, the proposed despeckling algorithms are applied to a single-look SAR image with different values for the input surface parameters. Then, the role of the spatial resolution of the DEM is investigated and evaluated by applying the algorithms with a priori scattering information estimated from DEMs with different resolutions. Finally, the role of coregistration errors between the DEM and the SAR image is analyzed for different DEM resolutions. For the entire sensitivity analysis, the scene topography is simulated via the 2-D fBm surface of fractal parameters $H = 0.8$ and $T = 10^{-5}$ m and electromagnetic parameters $\varepsilon_r = 4$ and $\sigma_c = 10^{-2}$ S/m shown in Fig. 5.14(a), while in Fig. 5.14(b) the corresponding local incidence angle map is depicted. Otherwise stated, all the surface parameters, namely, ϑ, H, T, ε_r, and σ_c are assumed to be known in the filters. SAR images are simulated via the SARAS simulator described in [157] with the COSMO-SkyMed sensor parameters [159]. The scattering behavior of the surface is simulated via the SPM option of SARAS, unless otherwise stated. The simulated single-look SAR image corresponding to the DEM in Fig. 5.14(a) is displayed in Fig. 5.15(a). The despeckling capabilities of the filters are quantitatively evaluated computing both no-reference and full-reference synthetic parameters.

In particular, the VoR, C_x, SNR, and MSSIM parameters are computed. Concerning SNR and MSSIM, the graphs reported in the following show both the absolute value and the relative value normalized to the maximum. For full-reference measures computation, reference (i.e., speckle-free) SAR images are computed via average of 512 sample single-look images. In order to quantitatively establish the quality of the despeckling algorithm, the reader is referred to the reference image measures in Tables 5.5-5.8. The reference image corresponding to the SAR image in Fig. 5.15(a) and to the DEM in Fig. 5.14(a) is shown in Fig. 5.15(b). For a better understanding of the key role of the a priori scattering information, the SB-PPB and SB-SARBM3D filters are also compared with original PPB with four iterations and SARBM3D.

The T_{fil} parameter of SB-PPB and the corresponding parameter of PPB (named T in the original paper [26]) have been optimized in terms of SNR for the SAR image in Fig. 5.15(a). In particular, T_{fil} equals 0.31 and 0.06 in SB-PPB and PPB, respectively.

5.6.1 Sensitivity Against the Scattering Behavior of the Surface

Several models concerning with single-bounce surface scattering have been developed so far. Depending on the surface model used, they can be categorized in “classical models” – in which the surface height is assumed to be normally distributed – and in “fractal models” – in which the fractal geometry is used. For more details the reader is referred to Chapter 2 of this Ph.D. Thesis and [45]-[49]. It is noteworthy that the accuracy of the scattering-based despeckling algorithms depends on the scattering behavior of the scene. For instance, the accuracy of the pilot image in SB-SARBM3D strictly depends on the accuracy of the SPM scattering model. In particular, one may reasonably expect that the more accurate the SPM model, the better the results. In order to assess the robustness of the SB-SARBM3D filter against the scattering behavior of the surface, the algorithms are applied to SAR images of the fractal scene previously described simulated assuming different scattering models. In particular, besides the SPM model, the $\cos\vartheta$, $\cos^2\vartheta$ and $\cos^4\vartheta$ scattering models are used for simulation purposes. Single-look SAR images are shown in Figs. 5.15-5.18, while synthetic performance parameters are reported in Tables 5.5-5.8.

Coherently with the theoretical framework developed in Sections 5.4.2 and 5.4.3, the most accurate results are obtained if the scattering behavior of the surface is correctly described by the SPM model [Fig. 5.15(a)-(f)]. If this is not the case, the more isotropic the scattering, the worse the results. For the considered scattering models, the worst results in terms of SNR are provided with the $\cos\vartheta$ scattering model, while with the $\cos^2\vartheta$ and $\cos^4\vartheta$ models intermediate results are obtained. The poor performance in the $\cos\vartheta$ case in terms of SNR can be partially due to the inadequacy of the Lambertian model to describe the scattering mechanisms at microwaves frequencies [45], [73], [161]. Nevertheless, we consider it for its widespread use in some specific applications of SAR imagery, e.g., shape from shading [162], [163], [164], [165]. However, a good texture preservation is provided by the scattering-based algorithms whatever the scattering model, as witnessed by the coefficient of variation in Tables 5.5-5.8. Indeed, the exploitation of the a priori scattering information provides better results - a better pilot image in SB-SARBM3D w.r.t. SARBM3D - even if the SPM model is not accurate, as shown by the performance improvement over the original filters. However, SB-SARBM3D exhibits a more significant sensitivity against the scattering behavior of the surface w.r.t. SB-PPB. In order to improve performance of SB-PPB, a suitable value for the T_{fil} parameter is needed, due to its link with the scattering distance decay. This is confirmed by the performance of the PPB filter, whose despeckling capabilities depend on the used scattering model also.

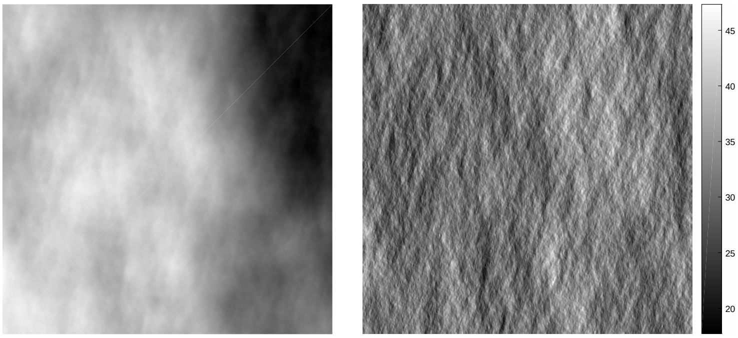

(a) (b)

Figure 5.14. (a) Fractal DEM with fractal parameters $H = 0.8$, $T = 10^{-5}$ m in the azimuth-slant range coordinate system; resolution is 2.58 m and 2.29 m in azimuth and slant-range respectively; (b) local incidence angle map in the azimuth-slant range coordinate system.

Table 5.5. Performance parameters for the SPM scattering model

	SNR	VoR	C_x	MSSIM
Reference	∞	0.98	0.67	1.000
PPB	3.47	0.95	0.51	0.993
SARBM3D	4.84	0.76	0.57	0.990
SB-PPB	5.67	0.78	0.57	0.996
SB-SARBM3D	6.80	0.81	0.55	1.000

Table 5.6. Performance parameters for the $\cos\vartheta$ scattering model

	SNR	VoR	C_x	MSSIM
Reference	∞	1.01	0.15	1.000
PPB	0.68	0.84	0.12	0.999
SARBM3D	1.31	0.89	0.11	1.000
SB-PPB	-0.084	0.75	0.18	0.999
SB-SARBM3D	0.93	0.77	0.17	1.000

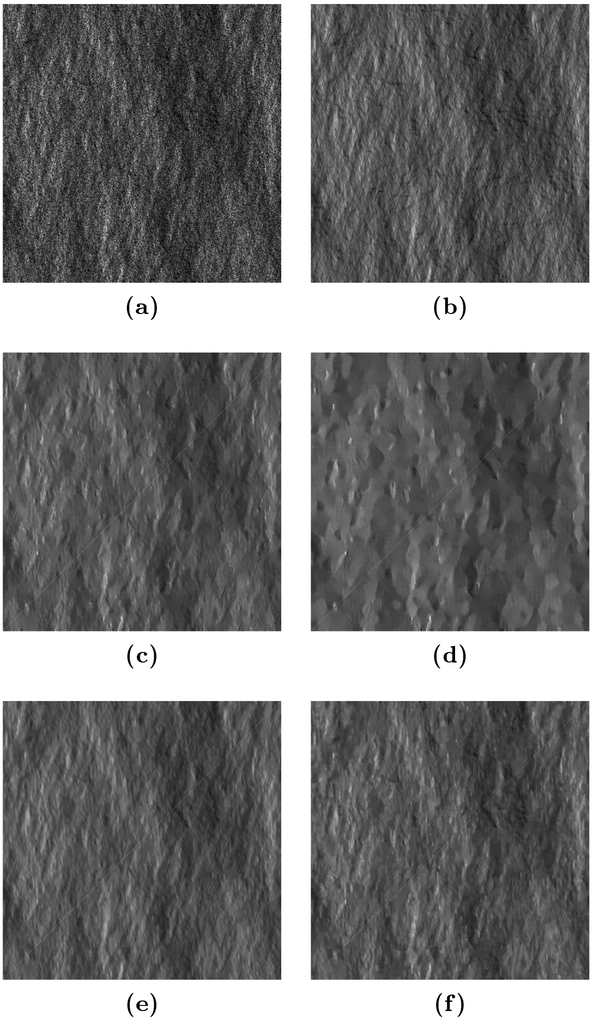

Figure 5.15. (a) 512 × 512 single-look SAR image corresponding to the scene in Fig. 5.14(a) with electromagnetic parameters $\varepsilon_r = 4$ and $\sigma_c = 10^{-2}$ S/m; (b) reference image obtained by averaging 512 single-look sample images; (c) SB-PPB with a priori scattering information estimated from the local incidence angle in Fig. 5.14(b) and assuming the right values for the surface parameters; (d) PPB with four iterations; (e) SB-SARBM3D; (f) SARBM3D.

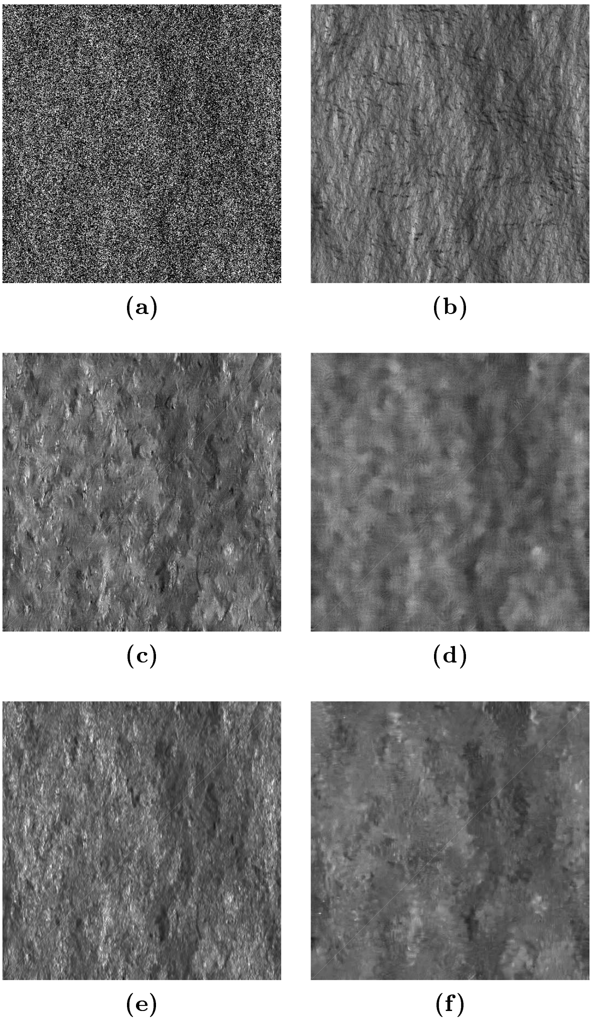

Figure 5.16. (a) Simulated and despeckled SAR images relevant to the DEM in Fig. 5.15(a) and assuming the $\cos\vartheta$ scattering model. (a) Noisy; (b) reference SAR image; (c) SB-PPB; (d) PPB; (e) SB-SARBM3D; (f) SARBM3D.

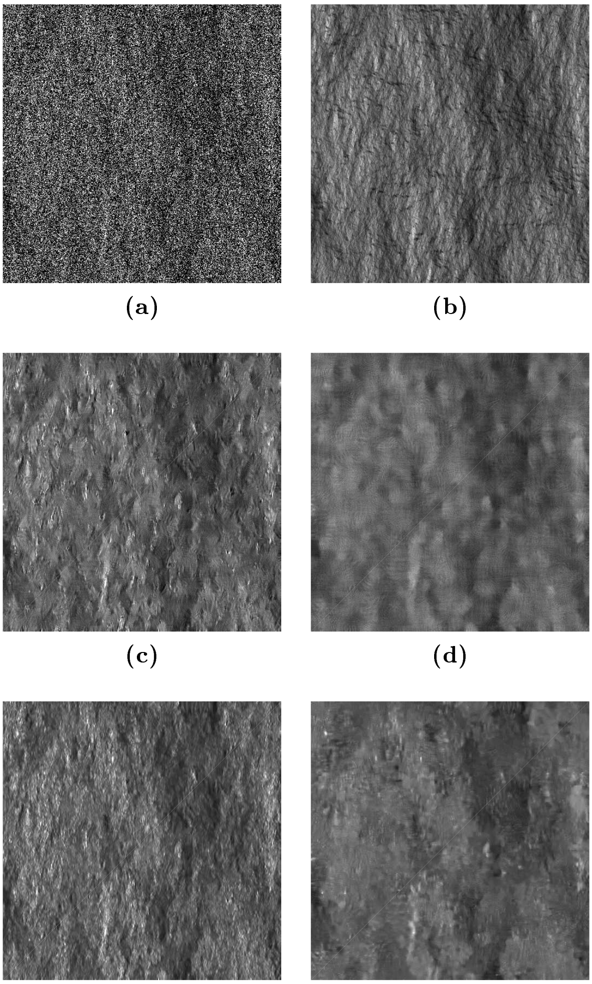

(a) **(b)**

(c) **(d)**

(e) **(f)**

Figure 5.17. (a) Simulated and despeckled SAR images relevant to the DEM in Fig. 5.15(a) and assuming the $\cos^2\vartheta$ scattering model. (a) Noisy; (b) reference SAR image; (c) SB-PPB; (d) PPB; (e) SB-SARBM3D; (f) SARBM3D.

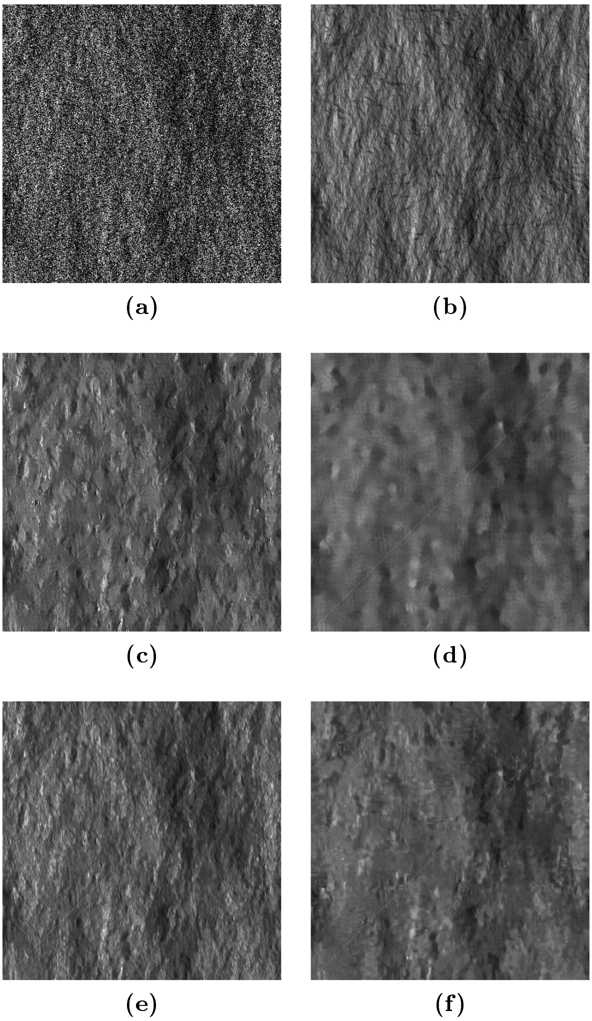

(a) (b)

(c) (d)

(e) (f)

Figure 5.18. (a) Simulated and despeckled SAR images relevant to the DEM in Fig. 5.15(a) and assuming the $\cos^4\vartheta$ scattering model. (a) Noisy; (b) reference SAR image; (c) SB-PPB; (d) PPB; (e) SB-SARBM3D; (f) SARBM3D.

Table 5.7. Performance parameters for the $\cos^2 \vartheta$ scattering model

	SNR	VoR	C_x	MSSIM
Reference	∞	1.02	0.21	1.000
PPB	1.29	0.87	0.14	0.998
SARBM3D	1.84	0.90	0.14	1.000
SB-PPB	1.17	0.76	0.20	0.999
SB-SARBM3D	2.19	0.78	0.19	1.000

Table 5.8. Performance parameters for the $\cos^4 \vartheta$ scattering model

	SNR	VoR	C_x	MSSIM
Reference	∞	1.01	0.26	1.000
PPB	1.98	0.87	0.18	0.998
SARBM3D	2.62	0.89	0.19	1.000
SB-PPB	2.90	0.76	0.25	0.999
SB-SARBM3D	4.02	0.78	0.25	1.000

5.6.2 Sensitivity Against Surface Parameters

The SPM model presented in Section 2.2, suitable for bare soil natural surfaces, properly accounts for both electromagnetic and geometrical characteristics of the surface [45]. As a consequence, the estimation of the a priori scattering information (see Eq. 2.15) requires, at least in principle, the knowledge (or estimation) of numerous parameters, namely the local incidence angle ϑ, the Hurst coefficient H, the topothesy T, the relative dielectric constant ε_r, and the electrical conductivity σ_c. It is noteworthy that an accurate knowledge of all these parameters is not available, at least where SAR data are of interest. However, as demonstrated in Section 5.4.1, a scattering-based approach for the despeckling problem is still applicable since the scattering mechanisms do not exhibit the same sensitivity to the different surface parameters. In particular, the sensitivity analysis conducted in Section 5.4.1 shows that the local incidence angle has the major influence on the energy backscattered from the surface. A key role is also played by the Hurst coefficient, while the remaining parameters exhibit a minor influence. Consequently, a reliable estimation of the a priori scattering information is still possible by assuming the availability of the local incidence angle map, i.e., a DEM of the underlying topography is required. For what concerns the Hurst coefficient, the angle-independent [166] method in [28] for the retrieval of the Hurst coefficient from a single-look SAR image is used; concerning the remaining parameters, typical values for most bare soil surfaces are used in the proposed filters. However, the proposed scattering-based algorithms are able to take into account the knowledge of whatever surface parameter. For example, in [167] a method to retrieve the soil surface parameters from polarimetric SAR data is presented; in [61], a general framework for surface parameters estimation from backscattered data is discussed.

In this Section, the sensitivity of SB-PPB and SB-SARBM3D against surface parameters is evaluated by means of an experimental analysis. In particular, the robustness of the proposed algorithms w.r.t. errors in the Hurst coefficient, relative dielectric constant, and the conductivity is assessed. It is noteworthy that, despite the influence on the backscattering coefficient, the topothesy simplifies in the SB-PPB filter weight evaluation (see Section 5.4.3). Consequently, a sensitivity analysis against the topothesy is conducted for the SB-SARBM3D algorithm only. To this aim, the algorithms are applied to the single-look SAR image in Fig. 5.15(c) relevant to the DEM shown in Fig. 5.15(a) in azimuth-slant range and the backscattering coefficient is estimated by using different values of the surface parameters. An accurate knowledge of the local incidence angle shown in Fig. 5.15(b), whose key role is investigated further in this Ph.D. Thesis, is assumed for the a priori scattering information estimation.

To assess the sensitivity of SB-SARBM3D and SB-PPB against inaccuracy in the Hurst coefficient estimation/knowledge, the algorithms are applied to the single-look SAR image in Fig. 5.15(c) with different values of the input parameter H in the range [0, 1]. The performance parameters of the despeckled images against H are depicted in Fig. 5.19 and Fig. 5.20 for SB-PPB and SB-SARBM3D, respectively. They show a non-negligible influence of the Hurst coefficient on the filter performance, thus confirming its non-negligible influence on the backscattered energy from the surface (see Section 5.4.1). In particular, in this scenario, a performance degradation up to 20% and 22% is experienced with SB-PPB and SB-SARBM3D respectively, in correspondence of very gross errors on H estimation. However, with typical values of actual natural surfaces ($0.6 \leq H \leq 0.9$) [73], a smaller degradation (up to 2% and 8% respectively) is experienced. High H values provide less smoothing and a better texture preservation, as witnessed by the VoR and the C_x parameters. Thus, the higher H, the higher the surface NRCS dynamic, the stronger the decay of the scattering distance in SB-PPB, and lower the weight in SB-SARBM3D. Best performance of SB-PPB in terms of SNR are ensured with $H = 0.8$, i.e., if an accurate knowledge/estimation of H is available.

It is noticeable that the non-negligible influence of the H parameter is faced via a proper estimation procedure [28]. However, owing to the a priori scattering information, the scattering-based filters provide better results w.r.t. the original ones for every value of H (performance parameters of PPB and SARBM3D are reported in Table 5.5).

Figures 5.21-5.24 show the sensitivity of SB-PPB and SB-SARBM3D against the relative dielectric constant and the electrical conductivity, respectively. In Fig. 5.25, the sensitivity of SB-SARBM3D against the topothesy is shown. The minor influence of these parameters on the energy backscattered from the surface reflects itself in the robustness of the proposed despeckling filters, whose performances are negligibly affected by an accurate knowledge of their actual values. Therefore, for such parameters, reference values can be used without incurring in a significant performance degradation, if an estimation/knowledge of these parameters is not available. For example, typical values for dry soil and damp soil at the microwaves are $\varepsilon_r = 4, \sigma_c = 10^{-2}$ S/m and $\varepsilon_r = 10, \sigma_c = 10^{-3}$ S/m, respectively. This allows the applicability of the algorithms even if an estimation/knowledge of the electromagnetic parameters is not available.

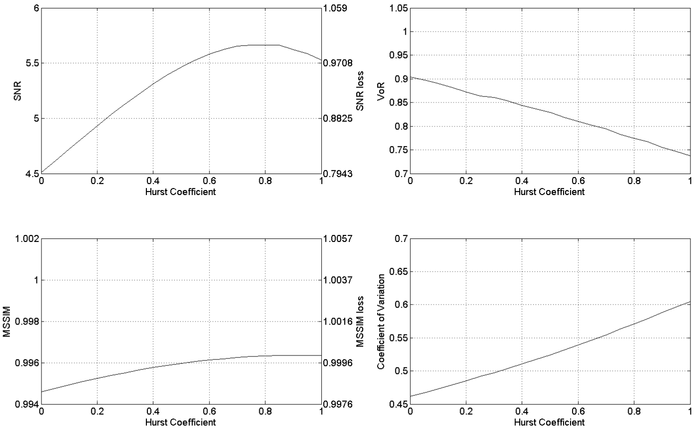

Figure 5.19. Sensitivity of SB-PPB against the Hurst Coefficient. Clockwise from top-left: SNR; VoR; Coefficient of Variation; MSSIM.

5.6.3 Sensitivity Against the DEM Resolution

In order to apply the proposed filters, a DEM of the scene is required. As previously stated, the ratio maps r_I and r_ϑ are aimed at properly weigh the pilot image provided by the original SARBM3D filter and the a priori scattering information by distinguishing topography-related and non-topography-related SAR intensity variations. It is noticeable that the higher the resolution of the DEM, the higher the probability to correctly detect topographic features. In this Section, the robustness of SB-SARBM3D and SB-PPB against the DEM spatial resolution is analyzed by applying the algorithms to the single-look SAR image shown in Fig. 5.15(c) with the a priori scattering information evaluated from DEMs with differ-

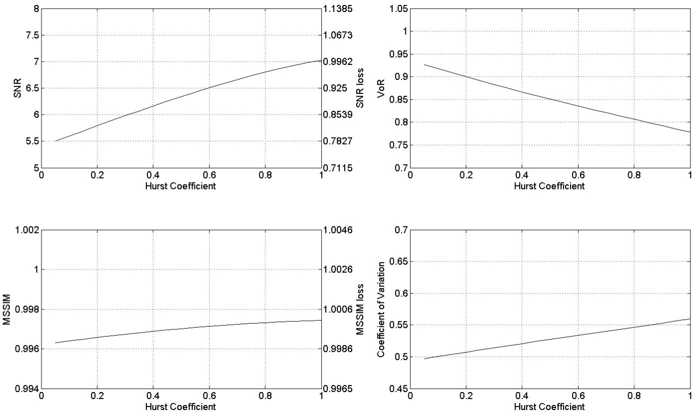

Figure 5.20. Sensitivity of SB-SARBM3D against the Hurst Coefficient. Clockwise from top-left: SNR; VoR; Coefficient of Variation; MSSIM.

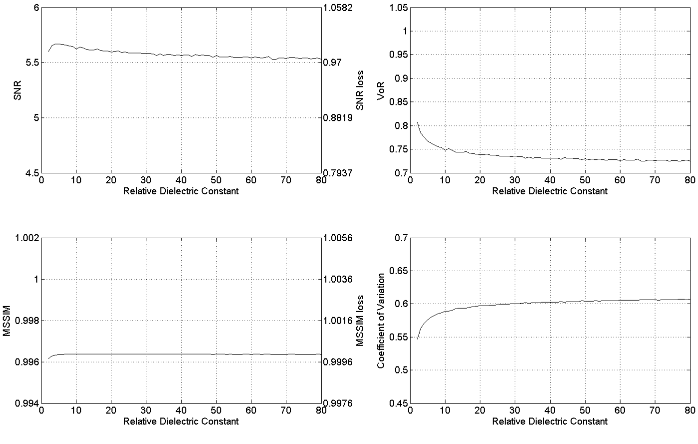

Figure 5.21. Sensitivity of SB-PPB against the relative dielectric constant. Clockwise from top-left: SNR; VoR; Coefficient of Variation; MSSIM.

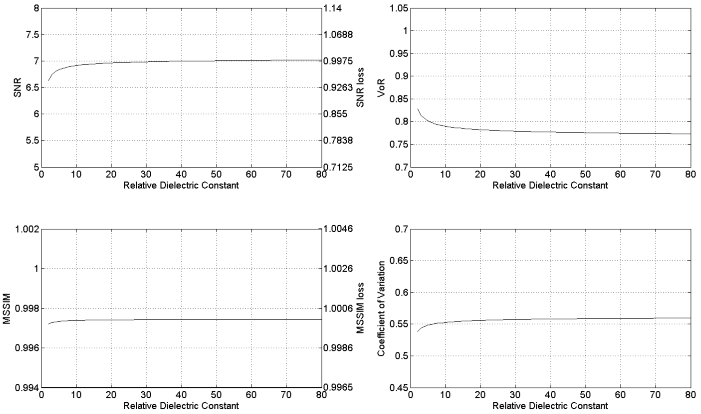

Figure 5.22. Sensitivity of SB-SARBM3D against the relative dielectric constant. Clockwise from top-left: SNR; VoR; Coefficient of Variation; MSSIM.

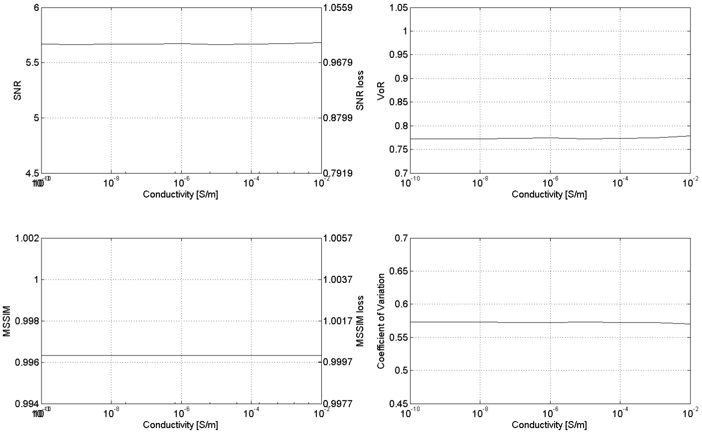

Figure 5.23. Sensitivity of SB-PPB against the electrical conductivity. Clockwise from top-left: SNR; VoR; Coefficient of Variation; MSSIM.

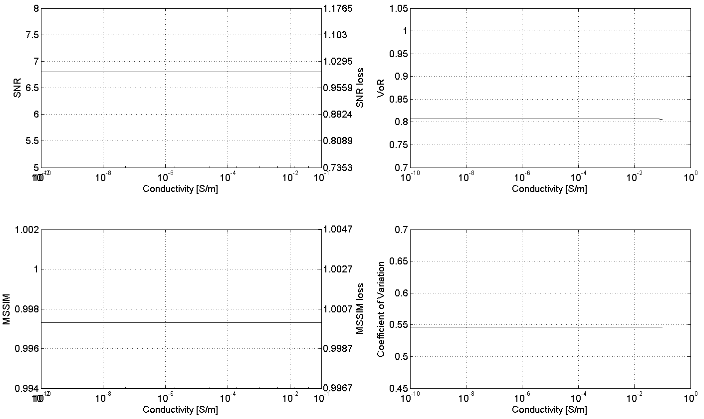

Figure 5.24. Sensitivity of SB-SARBM3D against the electrical conductivity. Clockwise from top-left: SNR; VoR; Coefficient of Variation; MSSIM.

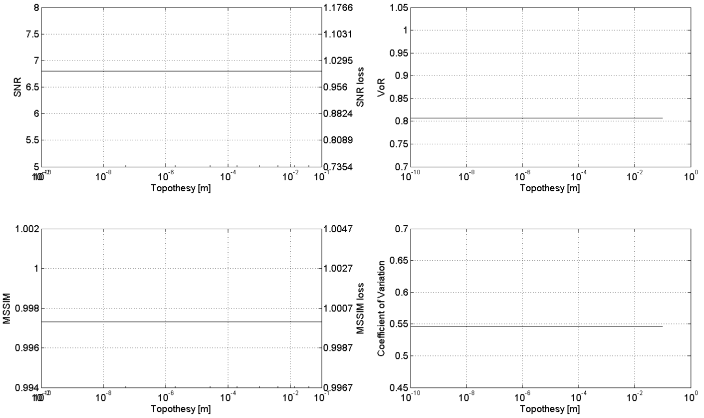

Figure 5.25. Sensitivity of SB-SARBM3D against the Topothesy. Clockwise from top-left: SNR; VoR; Coefficient of Variation; MSSIM.

ent resolutions. The highest-resolution DEM used [Fig. 5.15(a)] shares the same spatial resolution of the simulated SAR image in Fig. 5.15(c), i.e., 2.58 m in azimuth and 2.29 m in slant-range. The spatial resolution of the DEM in Fig. 5.15(a) is then reduced with an increasing power of two up to 512, which corresponds to a spatial resolution of about 1300 m in azimuth and 1170 m in slant-range. A gross DEM with a similar resolution is provided by the Global 30 Arc-Second Elevation (GTOPO30) DEM [168], while DEMs with very high-resolution up to 1 m are provided by Lidar systems.

The highest-resolution DEM ensures the best performance as shown in Figs. 5.27 and 5.28, providing a SNR improvement of more than 60% and 40% with SB-PPB and SB-SARBM3D respectively, over the original filters. A high-resolution DEM allows a significant speckle rejection without losing fine details, thanks to the richly detailed a priori scattering information. Lowering the resolution of the DEM causes a smoother a priori scattering information, as well as a smoother despeckled image, and a significant detail loss is visible with the lowest resolutions (Fig. 5.26), as witnessed by the VoR increasing with the DEM spatial spacing. With sufficiently low resolution, the a priori scattering information provides worse results than the original filters. In the considered scenario, with a resolution loss greater than 16, corresponding to a resolution of about 40 m in azimuth and 35 m in slant-range, the SB-PPB provides an overall worse result than PPB. With a further increasing of the resolution loss, the a priori scattering information becomes more and more homogeneous; consequently, SB-PPB tends to PPB. Concerning SB-SARBM3D, the a priori scattering information allows for performance improvements over the original SARBM3D up to a resolution loss of four, corresponding to a resolution of about 10 m in azimuth and 9 m in slant-range in the considered scenario. With lower resolutions, the absence of non-topographic features prevents the assignment of a high weight to the pilot image provided by the SARBM3D; consequently, an increasingly smoothed pilot image is estimated due to the high weight assigned to the a priori scattering term. Therefore, a smoother despeckled image is obtained with lowering DEM resolutions.

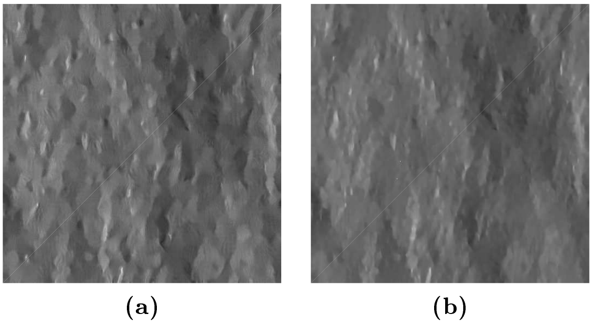

Figure 5.26. (a) SB-PPB and (b) SB-SARBM3D with a priori scattering information estimated from the local incidence angle map in Fig. 5.15(b) filtered with a 512×512 moving average filter and assuming the right values for the surface parameters.

5.6.4 Sensitivity Against the DEM Coregistration

In this latter Section, the sensitivity of the proposed algorithms against coregistration accuracy between the DEM and the SAR image is assessed. To provide a comprehensive understanding of the analysis, the sensitivity of the algorithms is evaluated for different DEM resolutions. For each DEM resolution, coregistration errors between the DEM and the SAR image are simulated via an increasing displacement of the local incidence angle map in Fig. 5.15(b) w.r.t. the SAR image in Fig. 5.15(c). Although possible coregistration errors can occur both in azimuth and range directions, in this work, for the sake of simplicity, only errors along the range axis are considered. Similar comments apply to (translation/rotation) errors in other directions.

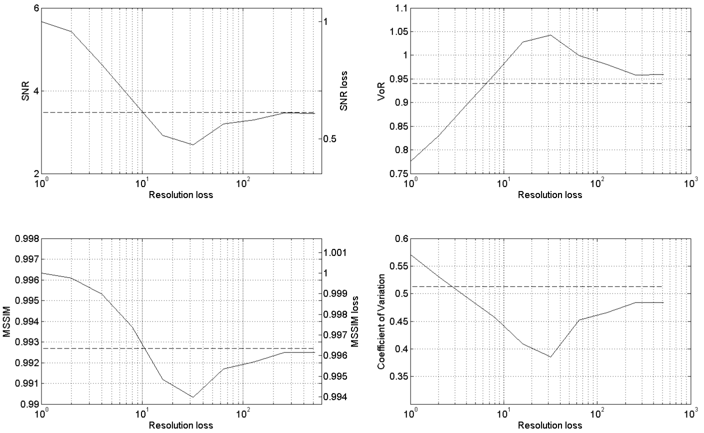

Figure 5.27. Sensitivity of SB-PPB against the DEM resolution loss. Clockwise from top-left: SNR; VoR; Coefficient of Variation; MSSIM. The highest resolution ensures the best performance; with very low-resolution DEMs, SB-PPB tends to PPB (dashed lines).

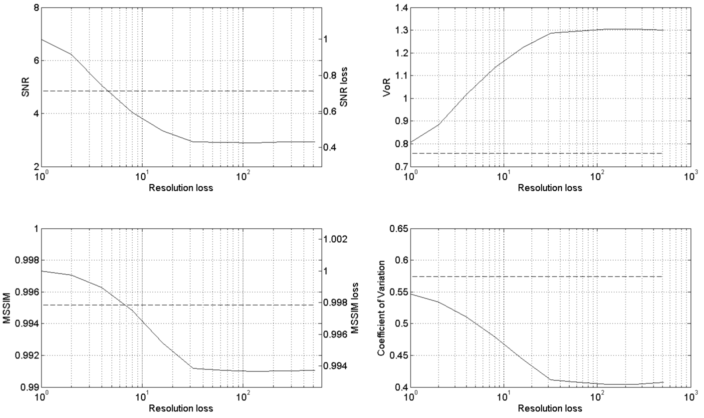

Figure 5.28. Sensitivity of SB-SARBM3D against the DEM resolution loss. Clockwise from top-left: SNR; VoR; Coefficient of Variation; MSSIM. The highest resolution ensures the best performance; SARBM3D (dashed lines).

The performance parameters shown in Figs. 5.29 and 5.30 indicate that the lower the DEM resolution, the stronger the robustness of the proposed scattering-based filters against coregistration displacements. Consequently, a particular attention to the coregistration step should be paid in presence of a high-resolution DEM. In this case, a significant performance degradation can be experienced if the coregistration step is not accurate. This is due to the significant spatial high-frequency content of the a priori scattering information in the case of high-resolution DEMs. On the contrary, the more homogeneous scattering information estimated from low-resolution DEMs causes a higher robustness of the performance even in presence of gross coregistration errors. However, with high-resolution DEMs, better performance is provided at the cost of a precise coregistration step. As shown in Fig. 5.30, an accurate coregistration step can compensate a low-resolution of the DEM, since in presence of a sufficiently high displacement, a high-resolution DEM may provide worse results than a fine-coregistered low-resolution one. Indeed, an homogeneous a priori information is invariant to translation. However, for a fixed mismatch, the higher the DEM resolution, the better the despeckling performance of SB-PPB. This occurs for SB-SARBM3D up to a resolution loss of 16. In conclusion, the highest-resolution DEM should be used, unless robustness of the filter is of interest. In the latter case, a significant smoothing (resolution loss not smaller than 16) of the DEM can be useful to provide less sensitivity against coregistration displacements.

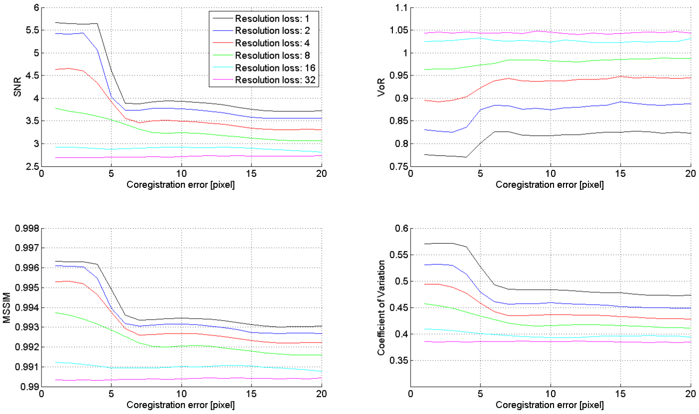

Figure 5.29. Sensitivity of SB-PPB against coregistration errors (in pixels) between the local incidence angle map and the SAR image for different DEM resolutions. Clockwise from top-left: SNR; VoR; Coefficient of Variation; MSSIM. Low-resolution DEMs provide smooth a priori scattering information. Consequently, the lower the DEM resolution, the stronger the sensitivity of SB-PPB against coregistration displacements.

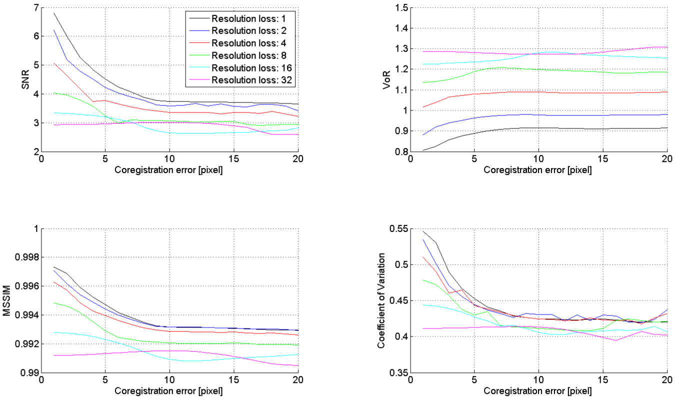

Figure 5.30. Sensitivity of SB-SARBM3D against coregistration errors (in pixels) between the local incidence angle map and the SAR image for different DEM resolutions. Clockwise from top-left: SNR; VoR; Coefficient of Variation; MSSIM. Low-resolution DEMs provide smooth a priori scattering information. Consequently, the lower the DEM resolution, the stronger the sensitivity of SB-SARBM3D against coregistration displacements.

Chapter 6

Sea Target Detection from Spaceborne GNSS-R Imagery

Sea target monitoring is of key importance in the field of global monitoring of environment, maritime security and surveillance. Accurate monitoring, continuous mapping and large-scale analysis of sea surface, sea ice sheets, and ship traffic are essential for activities as diverse as engineering, safety, travel, agriculture, recreation, and commerce. Real-time maritime surveillance and ship monitoring are relevant in a wide range of applications, such as clandestine activities contrast, naval warfare, traffic surveillance, oil discharge and sea pollution monitoring [31], [169]. In particular, in recent years, because of the decrease in fishery resources in the world, ship detection has become much more important for effective and efficient ship monitoring to prohibit illegal fishing activities in time. During the last years, sea surface monitoring has experienced a growing interest [31], [169].

Ice sheet mapping is fundamental in analyzing climate dynamics and evaluating human-induced climate changes. Currently, most of such information is gathered with very high accuracy by means of ground-based stations and networks. Despite the high accuracy provided and the well-assessed technology, in-situ measurements only provide local information. The spatial coverage provided by ground-based networks is generally limited to low elevation regions of the Northern Hemisphere midlatitudes and to snow course in mountainous regions [30]. In order to address accurate ice sheet mapping on a global scale, space-borne measurements from satellite constellations come into play. Detailed daily mappings of polar ice coverage derived from remote sensors are now publicly available on the web site of the US National Snow and Ice Data Center (NSIDC) [170].

Concerning international trades, more than 80% of the global trade and almost 90% of freight trade external to the European Union are seaborne [171], [172]. The civilian seaborne traffic transports more than 400 million passengers in European ports each year [171]. The large density of worldwide maritime traffic in 2015 is shown in Fig. 6.1. AIS is commonly used for coastal-traffic monitoring and it provides a comphrehensive information on the ship traffic, such as position, velocity, route and a unique reference, such as the International Maritime Organization (IMO) number. However, coastal AIS are limited in their coverage, thus covering up to 40 km off the coast [31]. To overcome this limitation, very recently, the AIS technology has been mounted onboard of spaceborne platforms, such as the SatAIS launched in 2011 by the German Aerospace Centre or the planned UK NovaSAR-S to be launched in the next years [171]. However, the main drawback of the AIS protocol in the field of maritime security and surveillance is the need for collaborating ships and ships equipped with correctly operating AIS facilities onboard. Remote sensing imagery gives the possibility to overcome these limits, thus allowing for the detection and tracking of non-cooperative ships and small ships without an AIS system on board [173].

During the last three decades, remote sensing has acquired an increasing appeal in the international scientific community owing to its wide potentialities. An increasing number of applications has been conceived and developed after the launch of new high-resolution sensors. Among them, optical and SAR systems have been intensively exploited in the ship detection field. An extensive literature on sea target detection and classification from optical and SAR data exists [31], [33], [34], [169]; a comprehensive state-of-the-art review report about ship detection from SAR data can be found in [32]. Although a comprehensive information, such as unique code, position, course, and speed can be acquired about the target state by means of AIS technology, the International Maritime Organization's International Convention for the Safety of Life at Sea only requires AIS to be fitted aboard international voyaging ships with gross tonnage of 300 or more, and all passenger ships regardless of size [32]. Therefore, detection of small ships and ships in open sea is currently a compelling application of remote sensing systems. Owing to their all-day, and all-weather imaging capabilities, SAR systems represent the most exploited remote sensing technology for ship detection, arousing even more interest after the launch of the new-generation high-resolution sensors, such as TerraSAR-X, RADARSAT-2, and the Sentinel-1 and COSMO-SkyMed constellations. Very accurate detection rate and positioning are currently addressed by most existing state-of-the-art ship detection techniques. However, the time resolution, i.e., revisit time, of SAR and optical sensors represents the main limitation for ship/ice sheet detection applications. With a limited number of satellites, the revisit cycle is quite long and cannot meet the requirements for real-time sea target monitoring [33], [35]. A time resolution on the order of hours is required for ship detection [35]. The World Meteorological Organization indicates a revisit time on the order of hours for sea-ice cover concerning the Global Numerical Weather Prediction, climate monitoring and ocean applications [36].

A revisit time on the order of days is provided by current optical and

SAR sensors but the COSMO-SkyMed constellation that ensures a revisit time up to 12 hours. However, the End of Life of COSMO-SkyMed is expected to be at the end of 2017 [159]. On the contrary, a temporal resolution on the order of hours is required for ship detection [35]. Another limitation for continuous sea mapping is related to the high spatial resolution typical of the new generation of satellites, which can prevent the exploitation of SAR and optical data to perform a real-time mapping due to the large amount of data to be processed. GNSS-R represents a relatively new remote sensing technology, firstly discussed in the early 1990s for mesoscale altimetry applications [119]. It is based on the acquisition and processing of GNSS signals of opportunity scattered from the Earth's surface. So far, one of the main applications of GNSS-R is the sea state estimation and monitoring, and several approaches and techniques to estimate the local wind speed from GNSS-R observables have been developed in the very last years [37], [123], [174]. Other very recent applications of the GNSS-R technology concern the surface scattering coefficient retrieval [175], [176], ocean topography [177], oil slick detection [38], [178], and tsunami detection [179], [180]. Due to the absence of a transmitter module, GNSS-R payloads can be mounted on nano- or small-satellites - as the recently launched ^{3}Cat-2 satellite by UPC [181] - with the potentiality to be grouped in wide constellations. Consequently, as shown later in this Chapter, spaceborne GNSS-R systems gives the chance to dramatically reduce the revisit time with respect to other remote sensing technologies, such as SAR and optical satellites, thus fulfilling the time resolution requirements for real-time maritime traffic surveillance and ship detection. A partial list of advantages and drawbacks of the aforementioned remote sensing technologies for sea target detection purposes is presented in Table 6.1.

GNSS signals reflected from ice were correctly identified and measured using the UK Disaster Monitoring Constellation (DMC) experiment on

February 4, 2005 over the Kuskowkwim Bay Alaska [182], [183]. Earth-reflected GPS L-band signals exploited by GNSS-R systems deeply penetrate in ice, allowing for analysis of snowpack internal structures and characteristics, such as thickness and accumulation rates [184]. In contrast with the typical Ku- and C-bands used in ice sheets analysis from SAR data, the low-frequency GNSS signals can penetrate up to 100 m in the ice, allowing for ice investigation on the millennium scale [184].

As already mentioned in Chapter 1, very few works dealing with the ship detection from GNSS-R observables can be found in literature [39], [40], [41], [42], [43]. In [39] the possibility to detect ships from GNSS reflected signals is analyzed by means of an experimental airborne mission. GNSS raw data instead of DDM is used in this work. In [40] the intriguing chance to detect sea targets from DDMs acquired in a backscattering configuration is sketched. However, some limiting hypothesis are required due to the particular geometric configuration between target, transmitter and receiver. In [41] the feasibility of sea target detection from spaceborne GNSS-R DDMs is demonstrated for different target sizes and sea state conditions. A spatial filter based on steerable antenna beams is proposed to solve for the mapping ambiguity. The work in [42] introduces a new method for ship detection from GPS-R correlation power spectra. However, few details are provided about the ship detection algorithm and the algorithm validation. Finally, the feasibility of detection of stationary ground targets from a GPS-Forward Scatter Radar system is analyzed and validated by means of an experimental mission and a Constant False Alarm Rate (CFAR) algorithm. Several ideas and hints, such as backscattering configuration, sea clutter compensation and CFAR approaches, have been proposed so far in the literature to perform sea target detection from GNSS-R observables; however, an organic and systematic proposal and validation of a sea target detection algorithm from DDMs represents the current main gap of the state of the art.

The revisit time achievable with spaceborne GNSS-R systems is analysed and presented by means of software simulations. The Satellite Tool Kit (STK®) software is used for simulating the orbit information in three different scenarios. The revisit time is then evaluated as a function of the number of satellites and channels and guideline graphs are provided and discussed. Furthermore, a sea target detection algorithm from spaceborne GNSS-R observables is presented, described and validated with actual UK TDS-1 data. The performance of the technique is assessed through the Receiver Operating Characteristic (ROC) curves.

To summarize, the main contributions presented in this Chapter are as follows:

- Numerical analysis of the revisit time provided by GNSS-R constellations by means of realistic simulated missions (Section 6.1).
- Derivation and implementation of a sea target detection algorithm from spaceborne GNSS-R DDMs (Section 6.2).
- Validation of the algorithm using actual GNSS-R data (Section 6.3).

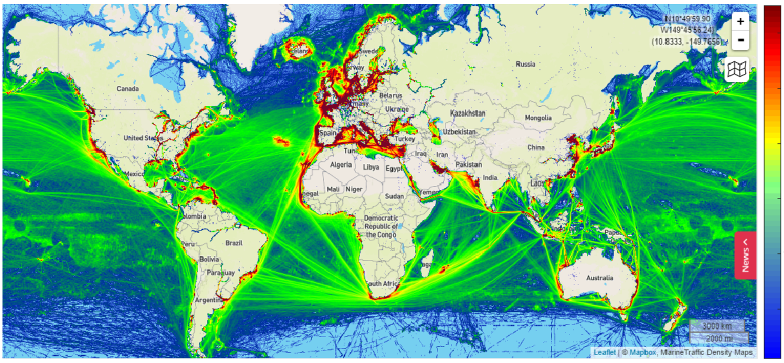

Figure 6.1. 2015 worldwide maritime traffic density map. The density is evaluated as the number of ships per grid cell per day. Taken from www.marinetraffic.com.

Table 6.1. Advantages and drawbacks of SAR, Optical and GNSS-R systems for sea target detection

	Pros	Cons
SAR	Independence on weather and light conditions.	Active systems (huge cost and size)
	Potential exploitation of multi-polarization, multi-frequency data.	Sensitivity to speckle and sea state, with increasing frequency [185].
	Very high spatial resolution (up to 1 m).	Difficult visual interpretation.
		Relatively long (for ship detection purposes) coherent integration time (up to 1 s).
		High revisit time[a].
Optical	Very high spatial resolution (up to 0.5 m).	Sensitivity to sea clutter.
	Relatively cheap.	Unavailable during night and cloudy days.
	Suited to hyperspectral imaging.	High revisit time[a].
	Easy to interpret (no expert user needed).	The large amount of data prevent the use in real time.
GNSS-R	Worldwide coverage on nearly real time.	Low spatial resolution (on the order of km).
	Compact, low-power, light-weight and cheap.	Not yet extensively studied and assessed.
	Independence on weather and light conditions.	Sensitivity to speckle.
	Ability of counter the attack of anti-radiation missiles.	
	Exploitation of pre-existing transmitters.	
	Very low revisit time.	

[a] TerraSAR-X: 11 days [186]. COSMO-SkyMed: up to 12 hours (4.5 hours on average); End of Life expected at the end of 2017 [159]. Sentinel-1: 1-3 days [187]. SPOT: 1-3 days (in cloud-free condition) [188]. LANDSAT: 16 days [189]. Sentinel-2: 5 days [190]. Required update time for ship detection on the order of hours [35].

6.1 Revisit Time

The major limit for the practical application of both SAR and optical imagery in the field of maritime surveillance comes from the relatively high revisit time as shown in Table 6.1. Currently, the COSMO-SkyMed constellation can provide a revisit time up to 12 hours on average [159], which is still not enough to guarantee a continuous monitoring of sea surfaces. Real-time operations in sea traffic control requires a revisit time on the order of few hours [35]. Owing to low weight, low size and low power consumption, GNSS-R can be launched in constellation formations at a relative low cost. This allows GNSS-R offering a revisit time sufficiently low for real-time ship monitoring purposes.

In contrast to other remote sensing approaches and systems, GNSS-R offers a significant flexibility in terms of costs, weight and performance, as well as a much faster mission design phase. Revisit time requirements for nearly real-time maritime surveillance can be much easily fulfilled with GNSS-R small satellites and several constellations can be put into orbit at contained costs. The very recent NASA Cyclone GNSS (CYGNSS) mission devoted to hurricane forecasting consists of eight small satellites and will provide frequent and accurate measurements of ocean surface winds with a revisit time of 2.8 hours (median) and 7.2 hours (mean) over the full $\pm 35°$ using only four parallel measurements [191].

Many variables influence the revisit time of a GNSS-R system. Some of them, such as the glistening zone size and the specular reflection point position, cannot be determined deterministically without a complete knowledge of the actual sea state and of the transmitter/receiver geometry. This will invoke for a statistical modeling of the revisit time, since some influencing parameters need to be statistically described. Alternatively, time resolution of such systems can be analyzed by means of mission simulation studies. Under appropriate hypotheses primarily regarding the duration of the time period simulated, some statistical descriptors can be inferred from the numeric simulation as well.

In this Ph.D. Thesis, we follow the second approach. The revisit time provided by GNSS-R systems is evaluated by means of the commercial software STK. In this simulation study, the dependency of the revisit time of GNSS-R constellations on the number of satellites, and the parallel channels is considered. In particular, three different scenarios have been analyzed. In each scenario, (up to) four eight-satellite constellations of GNSS-R instruments on a 98°-inclined equatorial circular orbit at 500 km altitude have been considered; each GNSS-R satellite is equipped with (up to) 16 parallel tracking channels acquiring signals from the GPS only (Scenario 1), GPS and Galileo (Scenario 2), GPS, Galileo, GLONASS, and BeiDou-2 (Scenario 3). Such constellations provide a global coverage to allow for sea target detection at high latitudes and can be implemented based on small satellite platforms, such as ^{3}Cat-2 [181], [192]. Table 6.2 lists the main orbital parameters for the four considered GNSS constellations, while Table 6.3 lists the main parameters of the three considered scenarios. The revisit time has been evaluated by simulating four-days missions with a time step of 120 seconds, successively interpolated to 60 seconds in Matlab. Earth's surface has been divided in a regular grid in Lat-Lon with a one-degree spacing in both latitude and longitude, corresponding to a 120×120 km^2 cell at the Equator and a 120×40 km^2 cell at 70 N. The specular point position is evaluated from the transmitter and receiver positions by means of the Newton-Raphson method, where the WGS-84 is used to model Earth's surface [181], [192]. The revisit time achieved in the three considered scenarios is shown in Fig. 6.2-Fig. 6.4 respectively, where (a) the average, (b) the median, and (c) the standard deviation of the revisit time computed in the covered areas are shown as a function of the following variables: the number of tracking channels (1 to 16) mounted on board GNSS-R instruments; the number of GNSS-R satellites (1, 8, 16, 24,

32) considered. Using few GNSS-R satellites leads to time resolution not far from that provided by the most recent SAR and optical missions (see Table 6.1), especially in the case of only few parallel tracking channels (see Fig. 6.2). In order to lower the revisit time, two solutions are achievable, namely increasing the GNSS-R constellation size, and/or increasing the number of receiving channels per receiver. A minimum mean revisit time of 5 hours and 36 minutes can be achieved in scenario 1 when using 32 GNSS-R satellites equipped with 16 receiving channels. In both solutions, a reduction of the revisit time is achieved by a higher number of glistening zones simultaneously tracked. The fundamental difference between the two solutions lies in the revisit time improvement allowed. Indeed, regarding the first solution, any desired time resolution can be achieved, at least in principle, by considering a sufficiently large GNSS-R constellation size. However, the improvement of the revisit time allowed by additional GNSS-R satellites diminishes as the constellation size increases, as shown in Fig. 6.2 in which a relative improvement of about 42% and 23% is experienced in the average revisit time when passing from 8 to 16 GNSS-R satellites and from 24 to 32 GNSS-R satellites, respectively. On the other side, the limited number of GNSS stations accessible by the GNSS-R satellite at the same time leads to a limited improvement of the revisit time by increasing the number of parallel measurements. In other words, a further increase of a sufficiently high number of parallel tracking channels would not imply the acquisition of new Earth-reflected signals. As a result, the revisit time exhibits a plateau as a function of the number of parallel measurements for any fixed GNSS-R constellation size and scenario. For instance, in scenario 1, in which only the GPS stations can be tracked, the revisit time does not exhibit any further significant improvement when using more than six receiving channels (see Fig. 6.2). If further reductions of the revisit time are required/desirable, the capability to track more GNSS transmitters instead of the introduction of further parallel channels should

Table 6.2. Orbital parameters for GPS, Galileo, GLONASS, and BeiDou-2 GNSSs

	GPS	Galileo	GLONASS	BeiDou-2
Number of orbital planes	6	3	3	3
Number of Satellites	24	27	24	35 (5 GEO)
Satellite Altitude [km]	20,180	23,222	19,100	21,150
Orbit inclination [degree]	55°	56°	64.8°	55.5°

be taken into account in the design phase of the GNSS-R. Indeed, the higher the efficiency in the exploitation of the parallel channels. In scenario 2, the possibility to track also Galileo satellites leads to a minimum mean revisit time of 3 hours and 13 minutes with an improvement of 42% w.r.t. scenario 1; up to 8 GNSS transmitters are accessed on average at the same time. The higher number of GNSS transmitters accessible simultaneously allows for a more homogeneity of the revisit time as well, as shown in Fig. 6.3(c). Even lower revisit time can be achieved on average by tracking GPS, Galileo, GLONASS, and BeiDou-2 as in scenario 3, in which a minimum mean revisit time of 2 hours and 13 minutes is achieved with an improvement of about 60% with respect scenario 1. In this scenario, no further lowering of the revisit time is experienced when using more than 12 receiving channels. However, the benefits of tracking multiple GNSSs are appreciable in the case of a sufficiently high number of tracking channels, as shown in Fig. 6.5 in which the average revisit time in scenario 1 (solid lines) and 3 (dash-dotted lines) is shown as a function of the receiving channels for one (black), sixteen (blue), and thirty-two (red) satellites. The graph also reveals that revisit time can be lowered even with a smaller constellation size by tracking more GNSSs (see the red solid line and the blue dash-dotted one). Finally, it is interesting to note that all the mentioned solutions can also address a higher homogeneity of the revisit time in the coverage area as confirmed by the statistics of the revisit time shown in Fig. 6.2-Fig. 6.4.

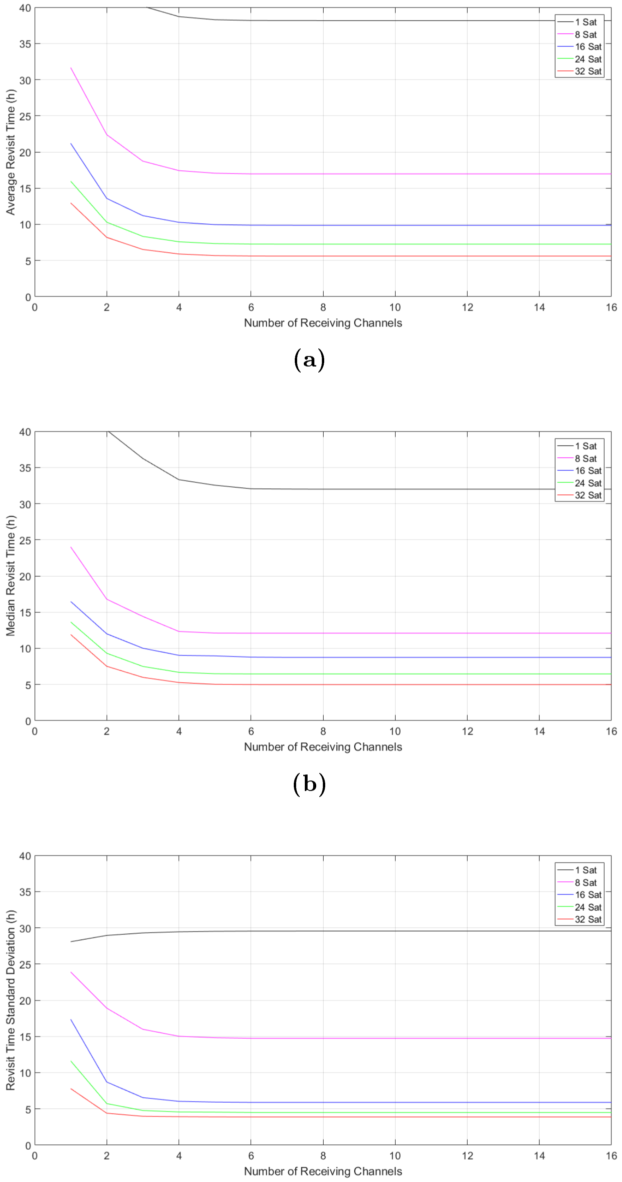

(a)

(b)

(c)

Figure 6.2. (a) Mean, (b) Median, and (c) standard deviation of the revisit time in hours vs. number of receiving channels considering one (black line), eight (magenta line), sixteen (blue line), twenty-four (green line), and thirty-two (red line) satellites. Only GPS stations are tracked.

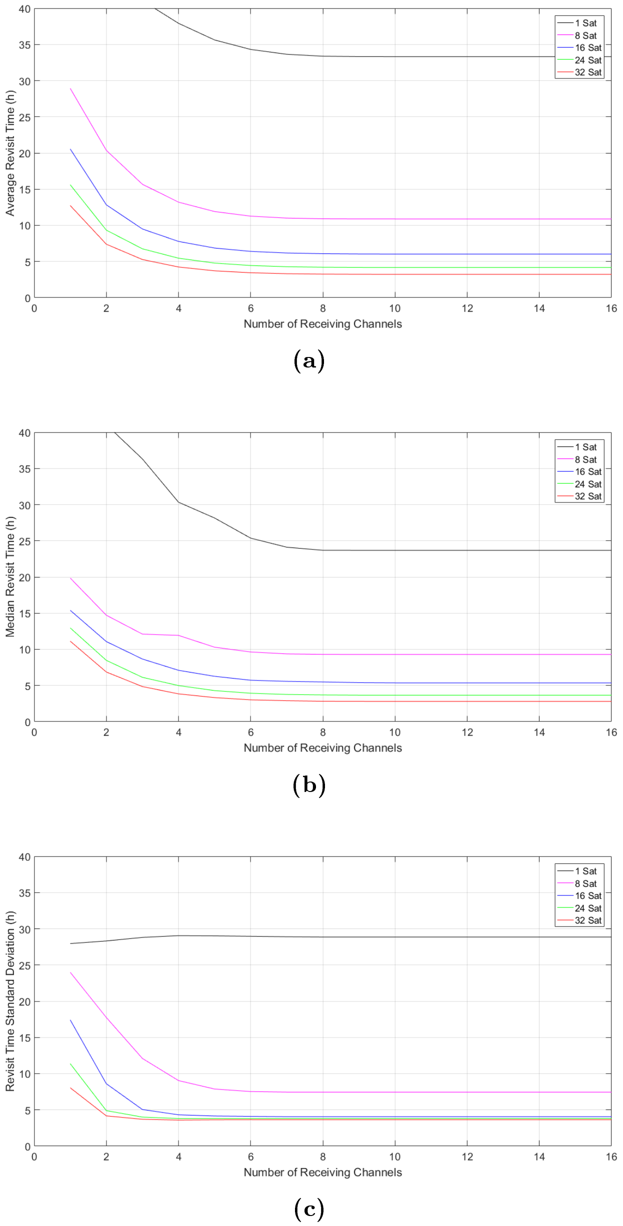

Figure 6.3. (a) Mean, (b) Median, and (c) standard deviation of the revisit time in hours vs. number of receiving channels considering one (black line), eight (magenta line), sixteen (blue line), twenty-four (green line), and thirty-two (red line) satellites. GPS and Galileo stations are tracked.

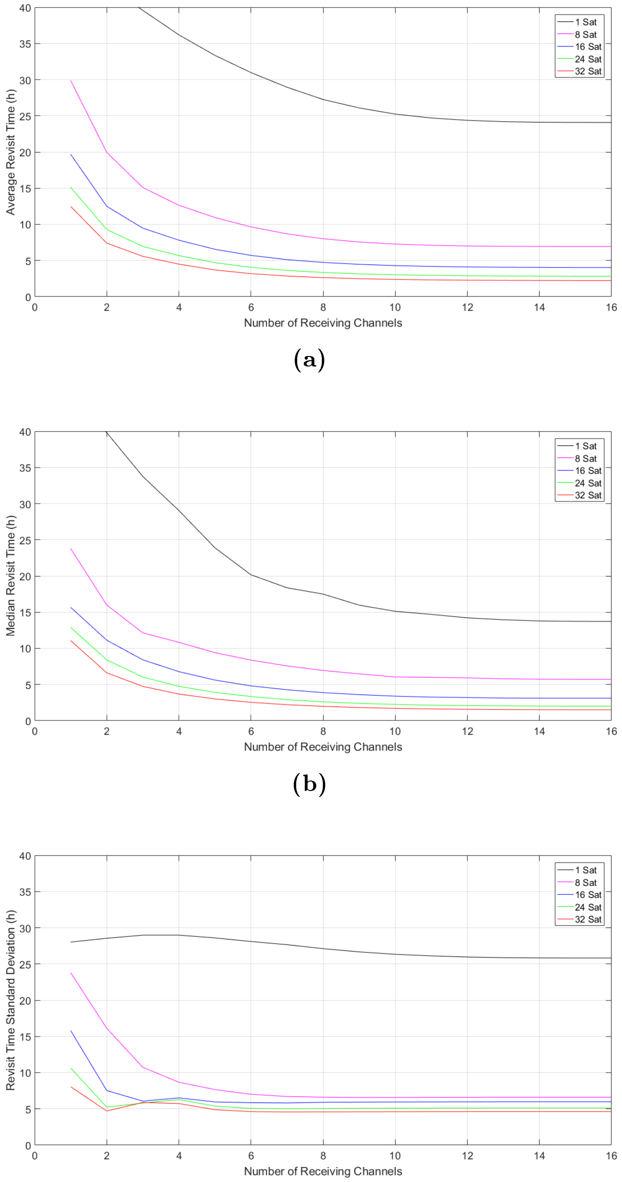

(a)

(b)

(c)

Figure 6.4. (a) Mean, (b) Median, and (c) standard deviation of the revisit time in hours vs. number of receiving channels considering one (black line), eight (magenta line), sixteen (blue line), twenty-four (green line), and thirty-two (red line) satellites. GPS, Galileo, GLONASS, and BeiDou-2 stations are tracked.

Table 6.3. Orbital parameters for the considered scenarios

	Scenario 1	Scenario 2	Scenario 3
Altitude [km]	500	500	500
Inclination [degree]	98°	98°	98°
Orbit type	Circular	Circular	Circular
Number of satellites	32	32	32
Number of parallel channels	16	16	16
GNSS systems tracked	GPS	GPS, Galileo	GPS, Galileo, GLONASS, BeiDou-2

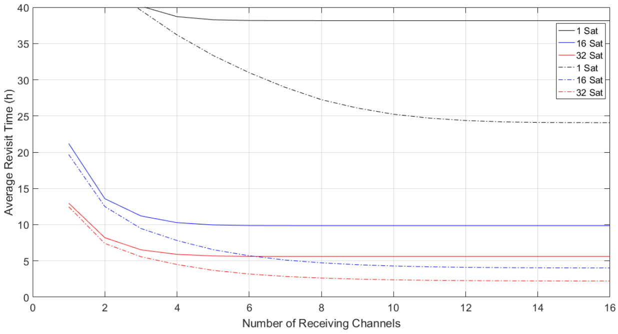

Figure 6.5. Mean revisit time as a function of the number of receiving channels in scenario 1 (solid lines) and scenario 3 (dash-dotted lines) using one (black lines), sixteen (blue lines), and thirty-two (red lines) satellites.

6.2 Sea Target Detection

In this Section, a constant false alarm rate (CFAR) sea target detection system from spaceborne GNSS-R imagery is derived and described. Performance are provided via the ROC of the algorithm. Generally, ship detection algorithms from remote sensing data share a common four-step scheme: land masking, pre-processing, pre-screening, and selection [32]. Land masking is aimed at canceling out the land contributions in the image, in order to focus the algorithm to sea surface only. This step is very important since ship detectors can produce numerous false alarms in land areas [31], [32]. However, this is a standard preliminary stage typically accomplished by applying a land mask derived from shoreline database [31], [193] and we do not focus on this step. The pre-processing step is aimed at making the detection stages easier. Typically, this stage is carried out by emphasizing the target-to-background ratio by means of targets and/or scene features, e.g., speckle filtering in SAR-based detectors [169], [194]. The pre-processing step can also include calibration and geolocation of the data [31], [32]. As a result, an enhanced image is then derived from the original one. Targets candidates are selected in the pre-screening stage by hard thresholding the pre-processed image. The threshold can be fixed over all the image or adaptively evaluated (CFAR approach). In the latter case, sea clutter characteristics are accounted for in order to adaptively estimate the local threshold. Threshold has to be designed by taking into account the tradeoff false alarms-detected targets, i.e., the ROC of the detector. If targets are associated to high (low) value of the enhanced image, a high (low) threshold produces low false alarms, but also a low detection rate; vice versa, a low (high) threshold provides a high detection rate and numerous false alarms as well. The last selection stage aims at reducing the false alarms (or ambiguities as in the SAR case) produced in the pre-screening step, thus improving the overall performance of the detector. Target features (size, shape) are commonly accounted for in the final target candidates' selection. A detailed description of the proposed sea target detector follows.

6.2.1 Proposed Sea Target Detection Algorithm

A detailed description of the proposed sea target detection follows. It consists of four steps: pre-processing, pre-screening, selection and geolocation. An overall flowchart of the detector is shown in Fig. 6.6.

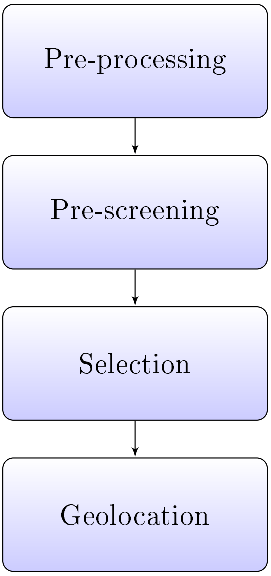

Figure 6.6. Overall flowchart of the proposed sea target detection algorithm.

Pre-processing

The backscattering configuration typical of SAR sensors makes sea surfaces backscattered energy weaker than that scattered by complex-shaped man-made objects, like ships [195]. Dihedral structures, typical of ships, cause a significant amount of energy backscattered to the sensor, while quite flat sea surfaces are characterized by a weak backscattering [171]. This causes ships to be represented as brilliant points in a dark background in the SAR imagery. Similar comments deserve the ship detection from optical data, in which the greater energy reflected by the ship w.r.t. water is related to its materials. Quite flat surfaces and targets, e.g., ships and ice sheets, are expected to appear as bright features or points in the DDM as they cause most of energy to be scattered in the specular direction. Therefore, the signal coming from quite flat surfaces is expected to be strong enough for target detection purposes and consistent without the power spreading in the delay-Doppler domain. Very recently, the appearance of coherent scattering phenomena in DDMs of sea ice sheets has been demonstrated [183]. The coherent scattering component represents the dominant contribution and makes the sea ice sheet appear as a bright feature in the DDM.

The bistatic configuration typical of GNSS-R systems makes the sea clutter a non-negligible contribution in the DDMs, so that a clutter compensation step is a desirable step to enhance the presence of potential targets over the sea. In this work, the pre-processing step consists of a clutter estimation and cancelation stage by means of DDM simulation. The main aim of this step is to cancel out the sea clutter contribution within the glistening zone in order to bring the target out of the background. In this Ph.D. Thesis, the P^{2}EPS (PAU/PARIS End to end Performance Simulator) tool has been used for simulation purposes [196], while the simulated DDM has been obtained by Least Square Fitting (LSF) with the measured one. The LSF step is performed assuming an unknown elevation angle, i.e., angle γ in Fig. 3 in [197]. Although there are others unknown parameters, such as α_R and α_T as defined in Fig. 3 in [197], we disregarded their role and performed the LSF w.r.t. γ only. This choice leads also to a simplified LSF step since only one parameter has to be tuned. To ensure an unbiased clutter compensation, the measured DDM is compensated for the thermal noise power as well. The noise power is estimated as the mean value of the pixels in the forbidden zone, i.e., the area of the Delay-Doppler domain not corresponding to any physical area. Indeed, in this area, no signal coming from neither sea or targets is measured, and the thermal noise is the only contribution. Noise power-compensated DDM and the simulated one are then normalized to their peak; the pre-processed image is then defined as the pixel-wise difference between the normalized actual and simulated DDMs. The output of this stage is a difference map of the glistening zone in which the horseshoe pattern, i.e., sea clutter, typical of spaceborne DDM over the sea, has been canceled out. A flowchart of the pre-processing step is shown in Fig. 6.7.

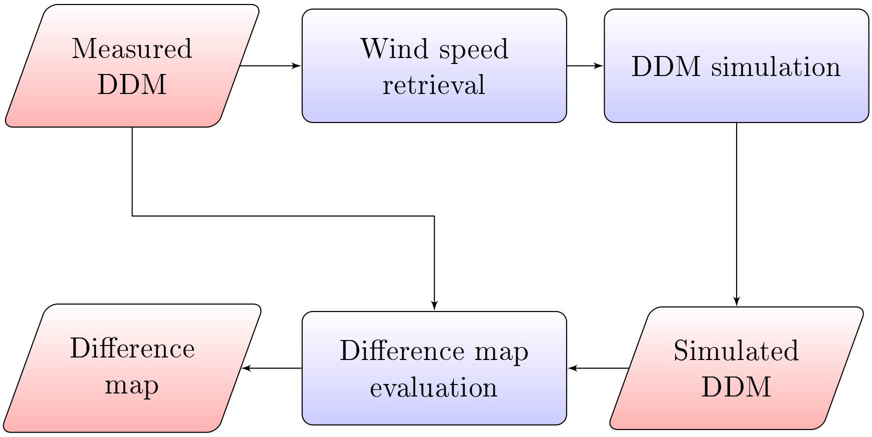

Figure 6.7. Flowchart of the pre-processing step.

Pre-screening

In the pre-screening stage, bright features in the difference map are associated to possible targets; therefore, a hard-thresholding is applied to the difference map to provide the target candidates. In order to account for clutter inhomogeneity and thermal noise, a CFAR approach is used at this stage. The pixel under test is then compared with a threshold adaptively evaluated by means of a sliding-moving window as explained in more details in Section 6.2.2. A flowchart of the pre-screening step is shown in Fig. 6.8.

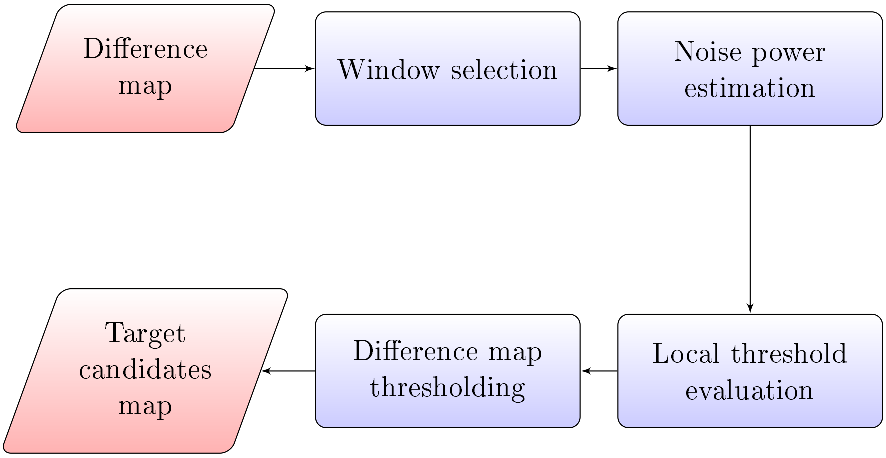

Figure 6.8. Flowchart of the pre-screening step.

Selection

In the selection stage, isolated targets, i.e., single-pixel targets, are supposed to be likely false alarms caused by noise. Hence, isolated bright pixels are likely to be spike noise randomly exceeding the local threshold. In support of this assumption, the power spreading effect caused by the PSF function comes into play. In presence of large features on the sea surface (large ships, sea ice sheets), the PSF spreads the received power on neighboring pixels, thus increasing their correlation. In presence of noise only, it is more unlikely to observe neighboring pixels exceeding the threshold and, then, single-pixel targets appear. Isolated, i.e., single-pixel, targets are removed from the pre-screened candidates map by means of a morphological operation. False alarms caused by small-to-medium isles, airplanes, speckle noise, are still possible. A flowchart of the selection stage is shown in Fig. 6.9.

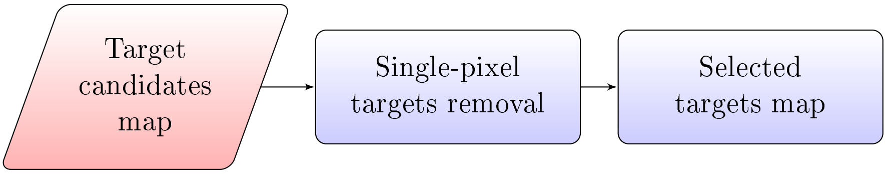

Figure 6.9. Flowchart of the selection step.

Geo-location

In the geolocation stage, the geographic location of the detected targets in the delay-Doppler domain are identified. In order to find the geographic coordinates of the detected targets, the observation geometry should be reconstructed in the geographic reference frame, i.e., the positions and velocities of transmitter, receiver, and the specular reflection points are needed. Those data are available from the auxiliary of spaceborne GNSS-R mission, e.g., TDS-1 case from MERRByS website (http://www.merrbys.co.uk/). Once the observation geometry is reconstructed, the positions in the delay-Doppler domain can be linked to the position in the geographic coordinate system. One consideration in the geolocation process is ambiguity of bi-static reflection geometry. In fact, a single position in delay-Doppler domain corresponds to two different points in the spatial domain (see Fig. 1 in [198]). It means that the detected targets from DDM can be assigned to two different geographic locations. To solve the ambiguity, the multi-beam method has been proposed [38], [178], [199]. However, the multi-beam (or beam steering) method is not suitable for small (nano-, cube-) satellite platforms because of the system complexity and the power, size, and weight constraints. In the fixed single beam case, the multiple overpasses can be used. A false location can be filtered out from the DDMs acquired from multiple overpasses on the target area. This multi-shot and multi-pass process also increases the accuracy of geolocation. For the other method, the auxiliary images from the other type of sensors can be used to overcome the ambiguity problem. A flowchart of the geolocation stage is shown in Fig. 6.10.

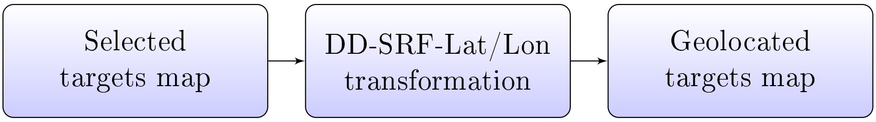

Figure 6.10. Flowchart of the geolocation step.

6.2.2 Performance Assessment

The performance of the proposed algorithm is theoretically assessed by evaluating the ROCs of the detector. These curves allow a fair performance assessment since they are not based on specific thresholds values. To this aim, the following hypothesis testing is considered for any pixel inside the glistening zone:

$$\begin{cases} H_1 : y = s + c + n, \\ H_0 : y = c + n, \end{cases} \tag{6.1}$$

where y is the pixel intensity of the incoherently averaged DDM, s is the target signal intensity, c stands for the sea clutter, and n represents the thermal noise. Supposing the thermal noise to be modeled as a normally-distributed random variable in the coherently-averaged DDM, the noise term n in Eq. 6.1 follows a chi-squared distribution in the incoherently-averaged DDM, i.e., $n \sim \chi^2(k)$, k being the number of incoherently-averaged DDMs, i.e., the ratio between the incoherent and coherent integration times, respectively; typical GNSS-R systems, such as TDS-1, CYGNSS, performs a 1 ms coherent acquisition and 1 s incoherent averaging [129], [200] so that in practical cases, $k \gg 1$ can be assumed. Recalling the central limit theorem, a normally distribution can be assigned to the noise term in Eq. 6.1, i.e., $n \sim N(\mu_n, \sigma_n)$. The noise power compensation reads as

$$y' = y - \mu_n, \tag{6.2}$$

and the hypothesis testing becomes

$$\begin{cases} H_1 : y' = s + c + n, \quad n \sim N(0, \sigma_n), \\ H_0 : y' = c + n, \end{cases} \tag{6.3}$$

the thermal noise being a zero-mean normally-distributed random variable at this stage. The pre-processing step is aimed at removing the sea clutter contribution in the hypothesis testing in Eq. 6.3, i.e., the new observable is the difference map $d = y' - \hat{c}$, where $\hat{c}$ is the estimated sea clutter. To simplify the mathematical derivation of the ROCs, we assume a perfect sea clutter suppression, i.e., $\hat{c} = c$; consequently, the hypothesis testing reads as

$$\begin{cases} H_1 : d = s + n, \quad n \sim N(0, \sigma_n), \\ H_0 : d = n. \end{cases} \tag{6.4}$$

In the pre-screening stage, a CFAR detector is applied, i.e., an adaptive threshold T is estimated in the neighboring of the pixel under test, once assigned a probability of false alarms P_{FA}. The probability P_{FA} can be written as follows:

$$P_{FA} = Pr\left(d > T | H_0\right) = Q\left(\frac{T}{\sigma_n}\right), \tag{6.5}$$

where $Q(\cdot)$ denotes the Q-function defined as:

$$Q(x) = \frac{1}{\sqrt{2\pi}} \int_{x}^{+\infty} \exp\left(-\frac{u^2}{2} \right) du. \tag{6.6}$$

Consequently, the local threshold reads as:

$$T = \sigma_n Q^{-1} \left(P_{FA} \right) \tag{6.7}$$

where $Q^{-1}(\cdot)$ stands for the inverse Q-function defined in 6.6. In order to compute the local threshold, the noise standard deviation needs to be estimated. In order to account for different error source in the difference map, such as residual sea clutter, speckle noise, imperfect coregistration, etc., the σ_n parameter is adaptively evaluated through the image, i.e., a CFAR approach is applied. In particular, σ_n is estimated within a $K \times K$ window centered in the pixel under test. Once σ_n has been estimated, the local threshold is then evaluated from Eq. 6.7. However, the σ_n estimation deserves a specific comment. To take into account potential extended targets and the spreading effects of the PSF in the delay-Doppler domain, a $L \times L$ guard window $(L < K)$ centered in the pixel under test is considered and not used for the σ_n estimation. Therefore, the guard window size influences the size of detectable targets, and its value has to be chosen as the maximum between one and the ratio between the target maximum size and the mean spatial resolution of the GNSS-R system. To avoid missing targets due to the PSF energy spreading effect, this value has to be incremented in both delay and Doppler directions of a number of pixels equal to the ratio between the length of the PSF and the delay-Doppler resolutions of the sensor, where the PSF lengths in delay and Doppler are $\tau_c \left(1 + \tau_c / T_i\right)$ and $1/T_i$ respectively, τ_c and T_i being the chip length and integration time respectively. The probability of detection P_D is by definition:

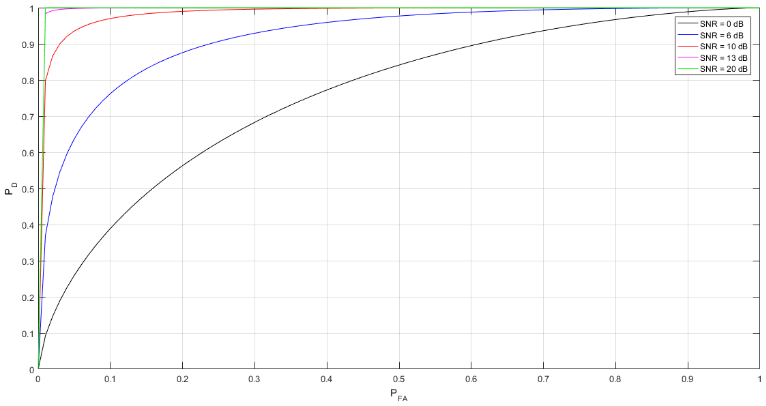

Figure 6.11. ROC of the detector. For any fixed P_{FA}, the detection rate increases with the SNR. The tradeoff between probability of detection and probability of false alarms is evident: an improvement of the detection rate can be achieved at a cost of an increased probability of false alarms.

$$P_D = Pr\left(d > T|H_1\right), \tag{6.8}$$

and can be related to the probability of false alarms and the SNR to provide the ROC curve of the detector. For the proposed detector, the ROC reads as:

$$P_D = Q\left(Q^{-1}\left(P_{FA}\right) - SNR\right), \tag{6.9}$$

where $SNR = s/\sigma_n$ is the signal-to-noise ratio. The ROC curve of the detector is shown in Fig. 6.11 for different values of the SNR. The tradeoff between probability of detection and probability of false alarms is evident: an improvement of the detection rate can be achieved at a cost of an increased probability of false alarms. In Fig. 6.12 the threshold is shown as a function of the P_{FA} for different values of σ_n as stated in Eq. 6.7.

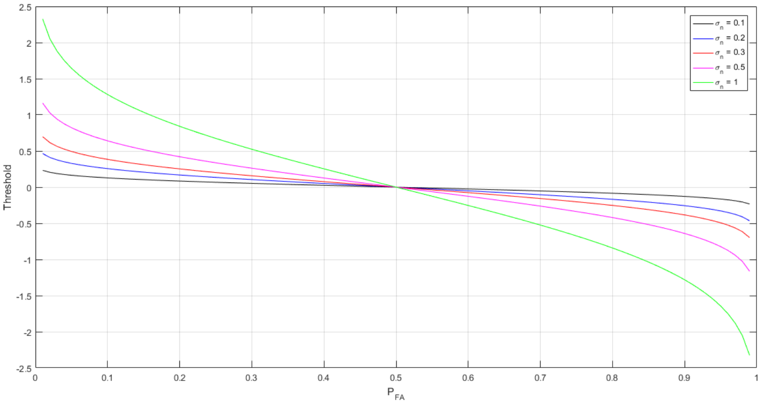

Figure 6.12. Threshold vs. P_{FA}. For P_{FA} close to zero ($P_{FA} < 0.5$), the threshold increases with increasing standard deviation of noise.

6.3 Experimental Results

In this Section, the proposed sea target detection algorithm is tested with actual UK TDS-1 DDMs and some preliminary results are shown. Orbital and sensor parameters are listed in Table 6.4. In the pre-processing step, the LSF step is performed on unknown scene parameters, namely the incidence angle in the UK TDS-1 data. Remaining orbital and sensor parameters, as well as wind speed, are taken from ancillary data. The difficulties to find a proper ground-truth regarding historical ship position and routes free of charge, together with the difficulty to visually assess the presence of ship targets within GNSS-R observables, have been partially compensated by applying and testing the detector on actual DDM data acquired close to offshore oil and gas platforms. Such platforms are static man-made objects, whose location is available for free in many cases. Therefore, they represent suitable sea targets to test the proposed detector in open seas scenarios.

The oil platform considered here is the Hibernia Platform (Fig. 6.13), located on the Hibernia oilfield in the North Atlantic Ocean, 315 km off St. John's, Newfoundland at 46.75°N, 48.78°W [201]. For the local threshold evaluation, a probability of false alarms equal to 0.01 has been considered. The first TDS-1 dataset used to test the algorithm, shown in Fig. 6.14(a) was acquired on April 1, 2015, at 00:19:37 UTC; the nominal specular point is at 46.83°N, 47.53°W. The Hibernia platform is 95 km off the specular point and is visible as an extended bright feature in the measured DDM due to the PSF. The pre-processing step (Fig. 6.14(c)) suppresses the sea clutter estimated in the simulated DDM in Fig. 6.14(b)); the Hibernia oil rig emerges from sea clutter and appears like a quite bright extended feature in Fig. 6.14(c) due to the PSF. In the pre-screening stage the oil rig is correctly detected; other two sea targets are detected as well: a single-pixel target and an extended target. The isolated target is rejected as noise in the successive selection stage (Fig. 6.14(e)), while the extended target is relevant to a region with a sea-ice concentration greater than zero, as reported in the NSIDC sea-ice concentration map relevant to the same day (Fig. 6.16) [202]. Detection of the same region is shown in Fig. 6.15. The actual DDM shown in Fig. 6.15(a) was acquired on April 1, 2015 at 00:19:49 UTC, i.e., 13 seconds after the previous actual case. The nominal specular is at 47.47°N, 47.84°W, and the sea ice sheet is visible as an extended target at about 1.34 C/A chips and 500 Hz in the delay-Doppler domain in both the measured DDM and the difference map in Fig. 6.15(c). The pre-screening stage correctly detects the target (Fig. 6.15(d)); an isolated target is removed in the selection stage since it is likely to be due to noise as previously explained (Fig. 6.15(f)).

In the second study case, the proposed sea target detector is applied to two consecutive DDMs acquired in the Gulf of Mexico on February 28, 2015 at 16:18:33 UTC [Fig. 6.17(a)] and 16:18:32 UTC [Fig. 6.18(a)] respectively. The nominal specular points, at 27.40°N, 89.47°W and 27.45°N, 89.45°W respectively, are about 180 km off the New Orleans, LA, coast, so

Table 6.4. UK TDS-I Parameters

Parameter	Value
Receiver altitude	640 km
Delay resolution	244.39 ns
Doppler resolution	500 Hz
Sampling frequency	16.37 MHz
Coherent integration time	1 ms
Incoherent integration time	1 s

that no significant contributions from land areas are expected in the considered dataset. The estimated sea clutter contribution in the delay-Doppler domain is shown in Fig. 6.17(b) and Fig. 6.18(b) and it is subtracted from the measured DDMs in the difference maps shown in Fig. 6.17(c) and Fig. 6.18(c). The pre-screening stage detects four (Fig. 6.17(d)) and three (Fig. 6.18(d)) target candidates respectively; two of which are rejected in the selection stage as shown in the selected target maps in Fig. 6.17(e) and Fig. 6.18(e). Gulf of Mexico is a major source of oil and gas in the United States [203]; indeed, the area is occupied by more than 200 of oil and gas platforms [204] and a huge maritime traffic takes place every day in the area [172]. Consequently, the detected targets are presumably actual sea targets (ships, oil platforms). The detection of a target on both DDMs in quite the same position reinforces this chance.

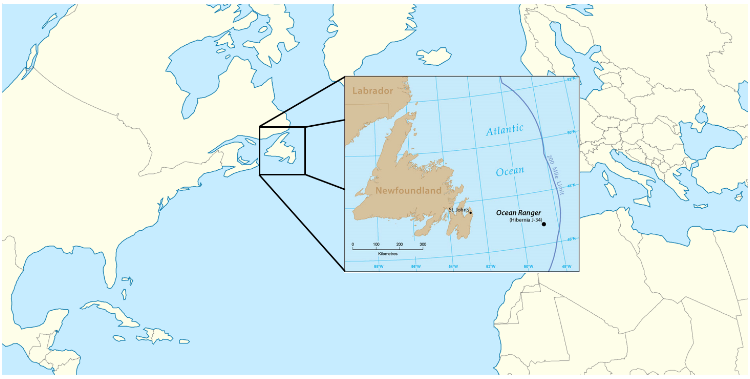

Figure 6.13. The Hibernia oil rig is situated on the Hibernia oilfield in the North Atlantic Ocean, 315 km off St. John's, Newfoundland at 46.75°N, 48.78°W.

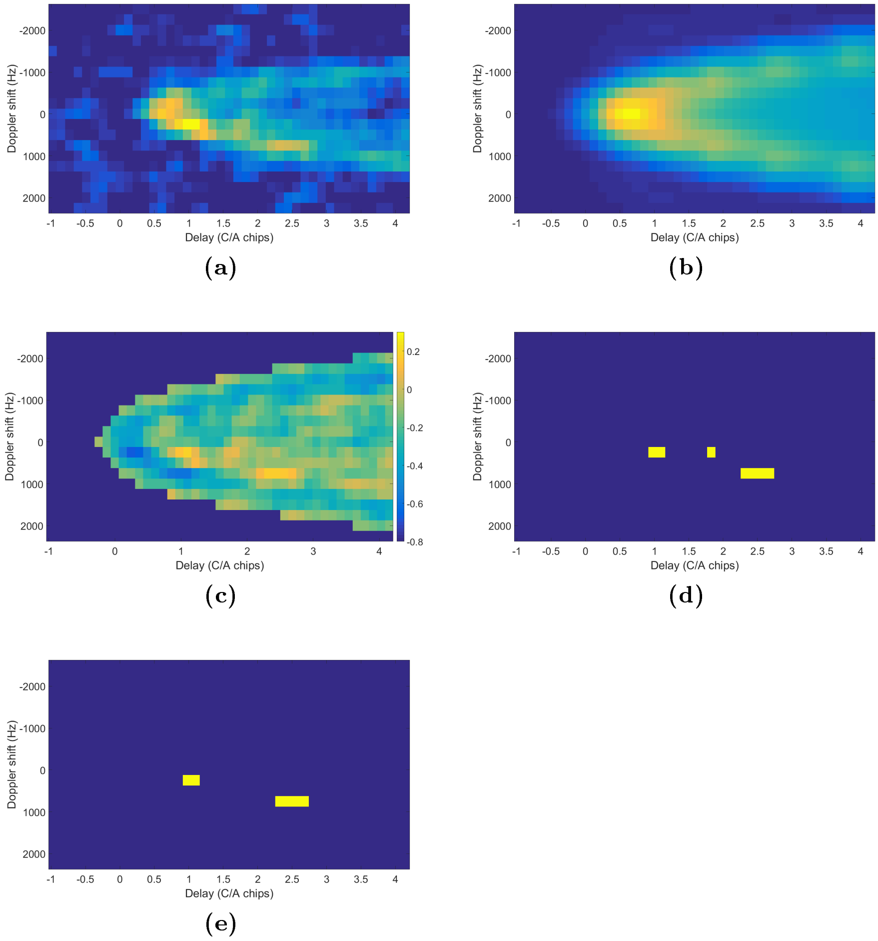

Figure 6.14. (a) TDS-1 DDM acquired on April 1, 2015 at 00:19:37 UTC. Nominal specular point at 46.83°N, 47.53°W. The visible bright feature is the Hibernia platform situated at about 95 km off the specular point. (b) Simulated sea clutter contribution. (c) Difference map. (d) Pre-screening; (e) Selection. The Hibernia platform is detected on the right. A sea ice sheet is detected on the left and validated using NSIDC data.

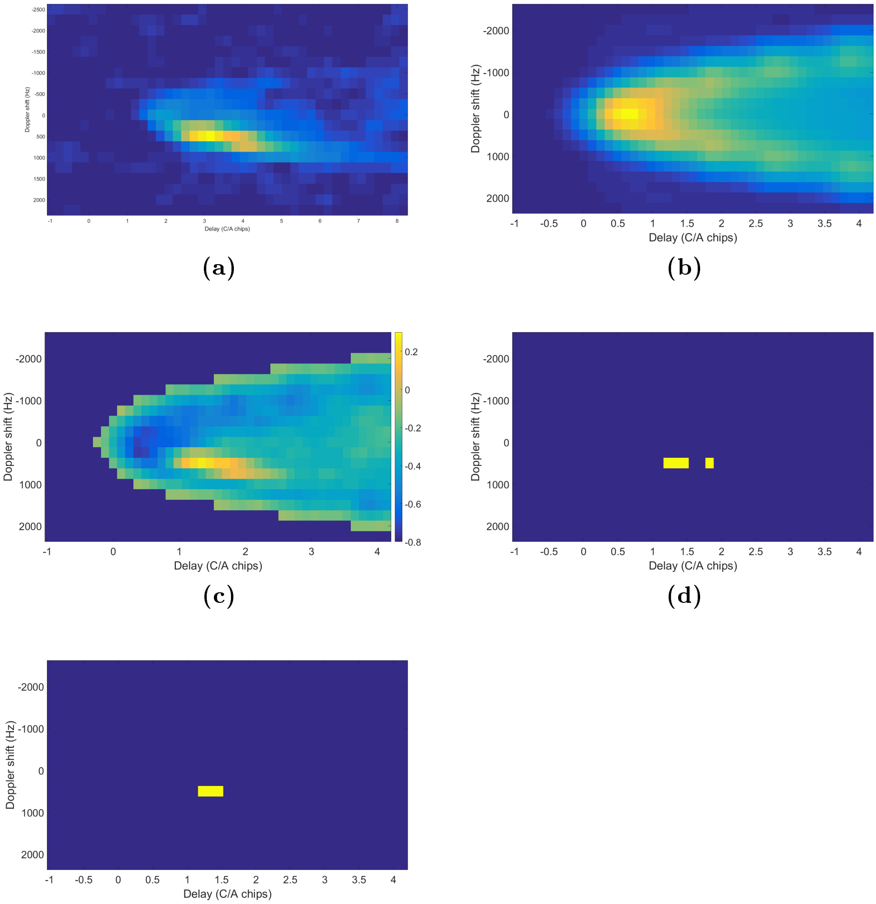

(a)

(b)

(c)

(d)

(e)

Figure 6.15. (a) TDS-1 DDM acquired on April 1, 2015 at 00:19:49 UTC. Nominal specular point at 47.47°N, 47.84°W. The visible bright feature is a sea ice sheet. (b) Simulated sea clutter contribution. (c) Difference map. (d) Pre-screening; (e) Selection. The detected target is a sea ice sheet validated using NSIDC data.

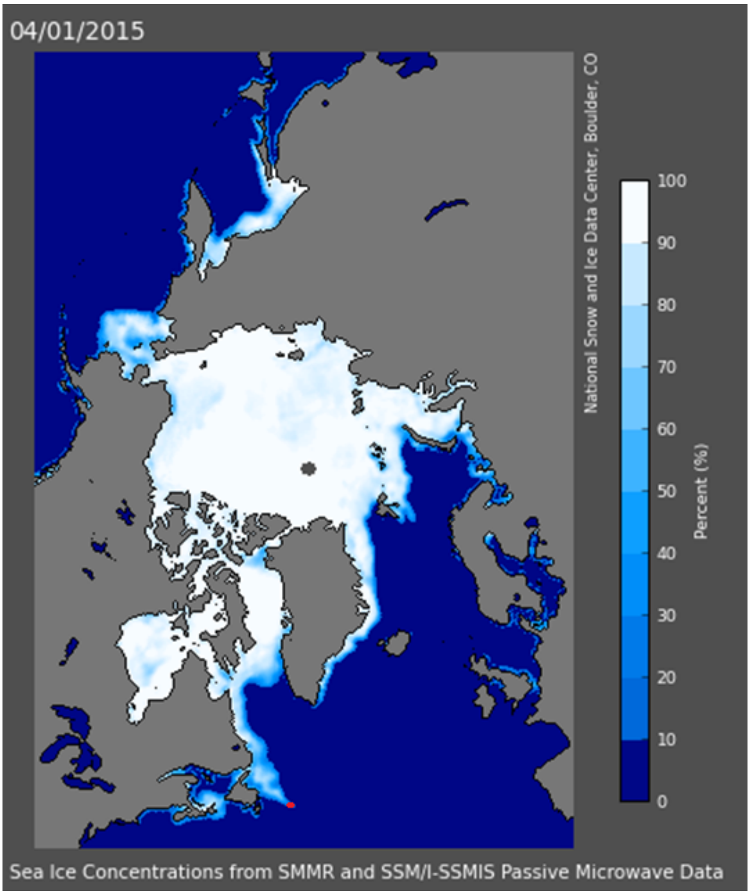

Figure 6.16. Image representation of the NSIDC sea ice concentrations data used for validation of sea ice sheets detection. The red point indicates the target detected by the algorithm.

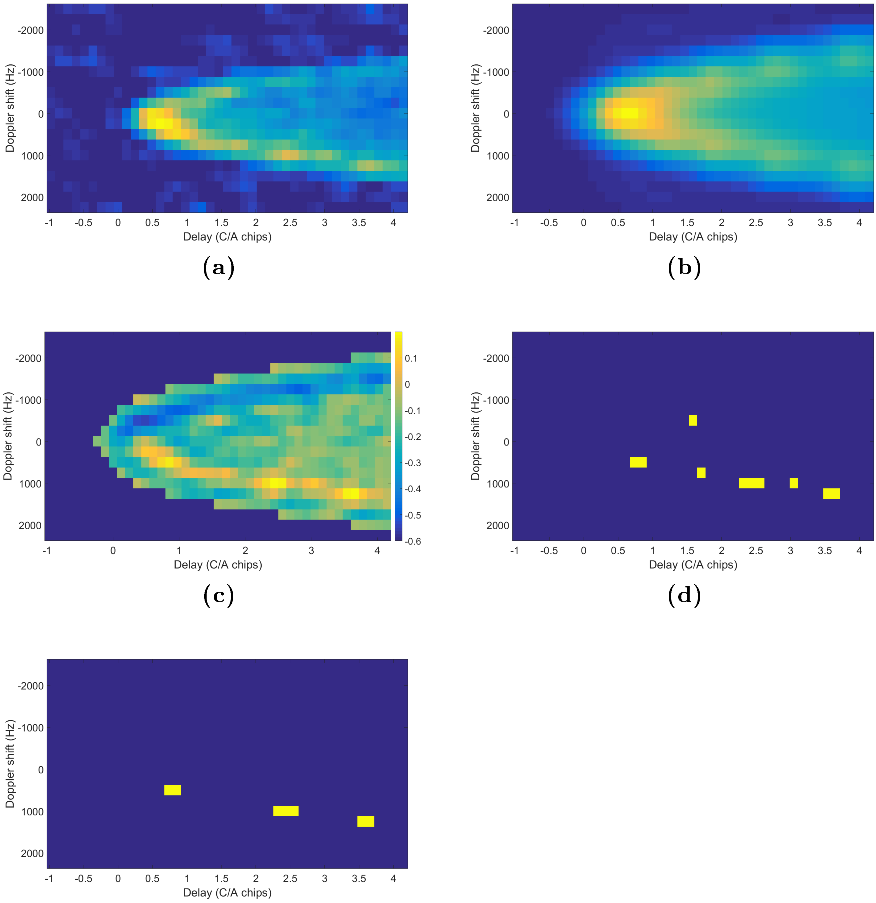

(a) (b) (c) (d) (e)

Figure 6.17. (a) TDS-1 DDM acquired on February 28, 2015 at 16:18:32 UTC. Nominal specular point at 27.45°N, 89.45°W. (b) Simulated sea clutter contribution. (c) Difference map. (d) Pre-screening; (e) Selection.

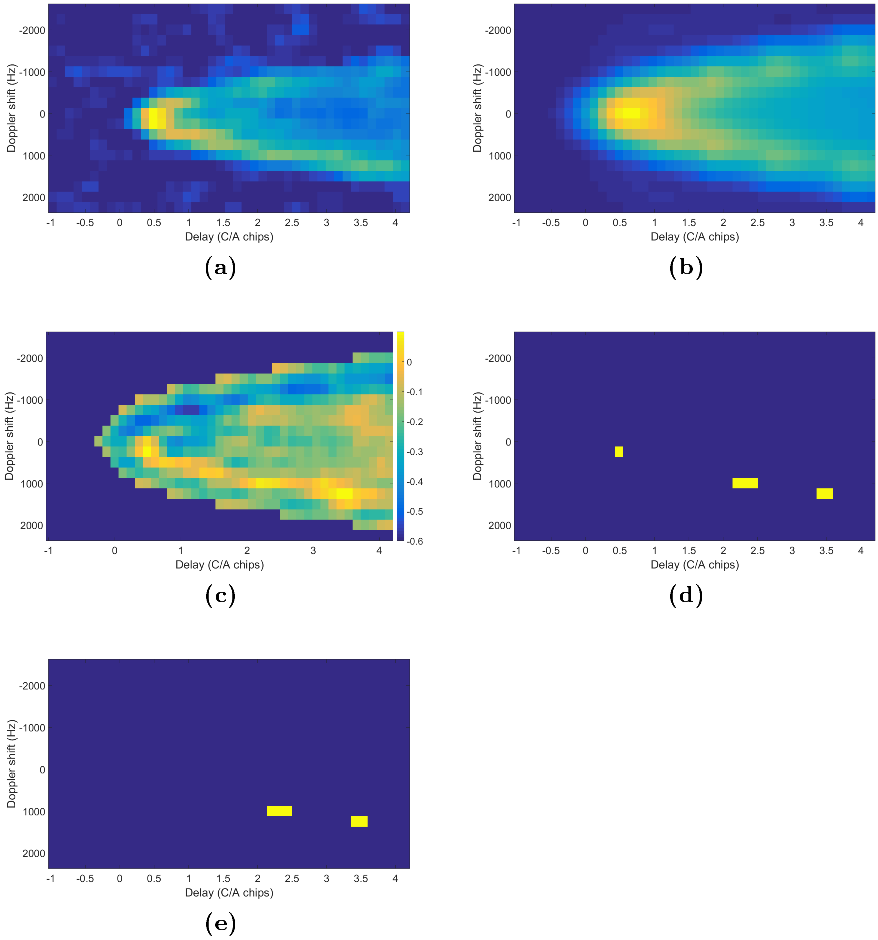

(a) (b) (c) (d) (e)

Figure 6.18. (a) TDS-1 DDM acquired on February 28, 2015 at 16:18:33 UTC. Nominal specular point at 27.40°N, 89.47°W. (b) Simulated sea clutter contribution. (c) Difference map. (d) Pre-screening; (e) Selection.

Chapter 7

Conclusions

This Ph.D. Thesis has studied the introduction of EM scattering concepts and models in remote sensing data in order to increase performance of state-of-the-art despeckling algorithms and allow for new applications of GNSS-R data. In particular, the exploitation of well-known scattering models has been investigated in two different applications:

- SAR Despeckling;
- Sea target detection and positioning using spaceborne GNSS-R DDM.

To allow for a more fruitful and deeper understanding of the concepts, ideas and models presented and discussed in the text, this Ph.D. Thesis has been divided into two parts: the first one, comprising Chapters 2 to 4, is an introductory part, providing the theoretical background to understand the techniques developed and described in the second part of this Ph.D. Thesis, including Chapters 5 and 6. In particular, Chapter 2 introduces the reader to the EM scattering models used further in the text, namely the SPM for fractal surfaces, and the GO model for normally-distributed surfaces. The chapter is aimed at deriving the NRCS for both scattering models as a closed-form function of the surface parameters.

Chapters 3 and 4 are devoted to present the remote sensing fundamentals exploited in the techniques developed in this Ph.D. Thesis. In particular, Chapter 3 has described the basic working principle of radar and the radar imaging system based on RAR. The core of the chapter discusses the SAR tool and how chirped waveforms and the synthetic aperture principle allow for a significant improvement of the spatial resolutions typical of RAR systems.

The exploitation of GNSS signals reflected from the Earth's surface for remote sensing applications is discussed in Chapter 4. First, the main GNSSs for global navigation services currently fully operational or under development have been presented and the navigation signals characteristics emphasized. Then, the possibility to acquire Earth-reflected GNSS signals to infer information on geophysical parameters has been explained, and the most diffuse GNSS-based remote sensing techniques, namely GNSS-RO and GNSS-R described.

The second part of this Ph.D. Thesis is described in the following sections.

7.1 SAR Despeckling

SAR despeckling is still a difficult task, even with single-polarized data. In this Ph.D. Thesis, the despeckling problem (Chapter 5) is treated in a physical framework via the introduction of scattering models in the filtering process. This is accomplished by introducing a priori information on the scattering mechanisms of the illuminated surface in the filter derivation. Two scattering-based despeckling algorithms have been conceived and implemented to apply to single-polarization SAR data. As suggested by their name (SB-PPB and SB-SARBM3D), they represent a modified version of pre-existing filters, namely PPB and SARBM3D, respectively. Despite being primarily designed for SAR images of natural scenes, some peculiarities of the original filters are exploited to enlarge their application to man-made scenarios as well. The a priori scattering information comes into play in slightly different ways within the two algorithms; however, in both cases, it aims at providing an estimation of the NRCS of the underlying natural surface by a proper modelization of both the surface roughness and its scattering behavior. To this aim, the surface roughness of natural surfaces has been modeled as a 2-D fBm stochastic process, while scattering phenomena have been modeled via an SPM formulation suitable for fractal surfaces. The NRCS estimation process starts from the consideration that in a natural scenario, topography, i.e., macroscopic roughness, if present, is the dominant contribution, whereas, other surface parameters play a minor rule, as emphasized in the sensitivity analysis conducted in Section 5.4.1. This permits a quite accurate estimation (for the considered purposes) of the NRCS of natural surfaces assuming the knowledge of the local incidence angle, which in turns requires a DEM of the underlying surface to be available. The way the a priori scattering information is exploited within the proposed algorithms is briefly summarized in the following.

As related to SB-PPB, starting from the PPB filter proposed in [26], it has been derived a new patch similarity measure introducing a fractal scattering model suitable for natural surfaces for the weight definition. Due to the strong dependence of the scattered field on the local incidence angle, the proposed distance reduces to a proper nonlinear distance in incidence angle. Owing to the scattering distance term, it has been shown that the SB-PPB performs better than the original PPB filter, even in cases in which scattering from the surface is not accurately described by the fractal scattering model employed. The proposed technique requires an a priori knowledge of the underlying topography, i.e., a DEM in the azimuth–slant range geometry of the SAR sensor coregistered with the noisy SAR image is required. The Hurst exponent describing the soil roughness can be easily estimated through the approach proposed in [28]. The proposed filter is originally designed for non-flat natural surfaces, i.e., for SAR images in which the intensity variations are mostly due to the topography. However, in order to deal also with flat regions and non-topography-induced backscattering variations, it has been implemented an iterative scheme that, in a smart and adaptive way, performs iterations only in flat regions in which the noniterative procedure does not provide a good reliability in terms of edge preservation if compared to the state of the art. To this aim, we have proposed a simple flat–non-flat binary classification method in order to discriminate topography-related from non-topography-related SAR intensity variations. The proposed binary classification technique is based on the DEM, and therefore, it does not require additional information. The adaptive scheme extends the applicability of the filter to different scenarios in which the single-bounce scattering is not the dominant scattering phenomenon, such as vegetated areas or suburban areas.

The modified version of the SARBM3D, originally presented in [24], the so-called SB-SARBM3D filter, improves the first-step estimate of SARBM3D by taking into account prior information about electromagnetic scattering of the sensed surface. Estimates provided by the first step of SARBM3D and by the assumed scattering model present complementary properties. In fact, SARBM3D provides good edge and detail preservation, while introducing visible artifacts in homogeneous and flat regions. Conversely, the scattering model with the assumed prior knowledge describes quite well the response of electromagnetically homogeneous natural areas, while it is inaccurate in describing scattering from nontopographic edges and man-made structures, unless additional information is available. Consequently, the new first step estimation is obtained by combining the prior scattering information and the first-step SARBM3D estimate with adaptive weights, related to the local reliability of the two terms. In particular, the weight map is computed using the ratio edge and line detectors developed in [155].

The filter weight evaluation is designed to assign a major weight to the a priori scattering information in regions with topography-related SAR intensity variations and, conversely, to assign a major weight to SARBM3D in regions with non-topograpy-related SAR intensity variations.

The effectiveness of the proposed filters and their capability to reduce speckle effects have been tested in an extensive experimental part, using both simulated and actual SAR images. Original filters are considered for comparison purposes.

The proposed SB-PPB filter exhibits objective performances comparable or superior to competing techniques on simulated single-look SAR images and satisfactory subjective quality on the actual SAR image considered. It is also noteworthy that the proposed algorithm "converges" to the iterative PPB in the presence of totally flat topography. The proposed adaptive scheme provides promising results especially in those cases in which topography is the main source of SAR intensity variations. With SAR images of non-flat surfaces, the proposed algorithm outperforms both the noniterative and iterative PPB filters, both in terms of speckle reduction and detail preservation, owing to the a priori topographic knowledge.

The new SB-SARBM3D filter exhibits promising results especially in homogeneous flat and gently sloped areas, providing a better speckle suppression than the original filter with the same good preservation of details.

In addition, the robustness of the proposed SB despeckling algorithms against different errour source has been evaluated by means of an experimental analysis. This is motivated by the fact that the a priori scattering information, modeled via the SPM model suitable for natural bare soil surfaces, requires, at least in principle, numerous surface parameters to be known/estimated. Although several retrieval algorithms exist in literature, an accurate knowledge of all the required surface parameters is not realistic. However, due the major contribution of the local incidence angle to the backscattered energy, a sufficiently accurate estimation (for the considered purposes) of the a priori scattering information is still possible if a DEM of the underlying topography is available. In particular, the influence of the following features on the filter performance is analyzed and discussed:

- scattering model;
- surface parameters errors apart from the local incidence angle;
- DEM resolution;
- errors in the coregistration step.

Concerning the first issue, different scattering models have been used to simulate the scattering behavior of the surface. Besides the SPM scattering model used in the filters, the $\cos\theta, \cos^2\theta$ and $\cos^4\theta$ models have been used. Best performance is ensured wherein the scattering behavior of the surface is well-described by the SPM model, whereas the $\cos\theta$ model causes the worst performance; in more general terms, the more accurate the SPM model, the better the performance of the proposed filters. Therefore, intermediate results are provided with the $\cos^2\theta$ and $\cos^4\theta$ models. However, both filters outperform the original ones for most scattering models considered.

The sensitivity analysis against surface parameters suggests that the huge knowledge required to estimate the a priori scattering information, modeled via the SPM model suitable for natural bare soil surfaces does not limit the applicability of the filter. Most of surface parameters, namely topothesy, relative dielectric constant and conductivity, influence very little the energy backscattered from the surface, at least in presence of a significant topography. Consequently, an accurate knowledge is not strictly required for such parameters, and reference values can be used.

Among the surface parameters, the Hurst coefficient has non-negligible influence on the filter performance, providing a significant performance degradation in the case of gross estimation errors. However, in the analyzed case, the proposed filters provide better results than original filters regardless of the estimation error. Indeed, the Hurst coefficient can be estimated via the algorithm proposed in [28]. If not the case, a reference value can be used. For typical values of H corresponding to actual natural surfaces ($0.6 \leq H \leq 0.9$) [73], a negligible performance degradation is experienced. The very minor influence of the electromagnetic surface parameters pointed out in this Ph.D. Thesis suggests the use of reference values.

The DEM resolution plays a key role on the despeckling capabilities of SB-PPB, especially concerning the detail preservation capability. Good performance is ensured by DEM with spatial resolution comparable with the SAR image, thanks to the very detailed a priori information. Therefore, the finer the topography details, the better the details preservation capability of the filter. With decreasing DEM resolution, a dramatic performance drop is experienced. With low-resolution DEMs, a significant performance drop is experienced: in presence of a significantly gross DEM, worse performance than SARBM3D may be provided by SB-SARBM3D; SB-PPB tends to the original PPB, the a priori scattering information tending to the homogeneous a priori information exploited in the PPB filter. For DEM resolutions up to a few times the SAR image resolution (16 for SB-PPB, four for SB-SARBM3D), the a priori scattering information ensures better performance than the homogeneous one.

The DEM resolution plays a key role even in the robustness of the filters against coregistration mismatches between the SAR image and the DEM. Thus, a high-resolution DEM, even if providing a richly detailed a priori scattering information, causes a significant performance drop in presence of coregistration errors, unless the topography is gentle enough. On the contrary, low-resolution DEMs (resolution loss w.r.t. SAR image not less than 32) allow a high robustness (relative variations of SNR up to 13%) of the filter performance against errors in the coregistration step, thanks to the smoother a priori information.

7.1.1 Future Research Lines

SB despeckling is a novel idea and there is much room for further investigations and analyses in terms of both theoretical studies and experimental results. A major issue for further research is the ability to take into account peculiar scattering mechanisms from both natural and urban areas. At the same time, the research in this field would benefit from better tools for the numerical assessment of performance, including, for example, a quantitative measure of despeckling artifacts. In addition, the proposed SB approach can be easily applied to other despeckling filters. The research in this field would also benefit from a scattering model selection algorithm for a suitable filter model-selection step. Furthermore, an approach similar to the one presented here for the scene topography may be used to take into account some additional a priori information about the sensed scene, in order to move a step further toward a more meaningful physical-based and object-oriented despeckling approach. Last, but not least, the possibility to estimate the local incidence angle map, needed by the filter, from a single SAR image would be useful not only in the proposed despeckling approach since the a priori knowledge could be estimated from the image itself without requiring extra information, but it would be also relevant per se since it could be useful in a number of applications, such as DEM generation and refinement. A DEM refinement procedure from SAR data will allow for the exploitation of higher-resolution topographic information, thus leading to a non-negligible performance improvement of the SB despeckling algorithms.

7.2 Sea Target Detection Using Spaceborne GNSS-R data

In Chapter 6, a feasibility study of real-time sea target detection from GNSS-R observables has been assessed. Owing to low cost and low size, small-satellite GNSS-R constellations can be developed at a much lower cost compared with competitive remote sensing techniques, giving the chance for a near real-time worldwide sea traffic monitoring and control. An experimental study of the revisit time provided by GNSS-R constellations has been conducted by means of mission simulations and analysis. This experimental study aims at providing some practical guidelines for the mission design, by analyzing the most relevant adjustable parameters influencing the time resolution and providing synthetic numerical results on realistic test missions. Three different scenarios have been defined and simulated in order to evaluate some first-order statistics of the revisit time, namely average, median and standard deviation. It has been shown that, even if single GNSS-R systems can provide time resolution similar to other remote sensing technologies, such as SAR and optical systems, the strength of GNSS-R systems lies in the actual chance to group them in cooperative formations, which can offer revisit times as low as 2 hours or even lower. The actual revisit time depends upon numerous parameters, such as the number of satellites, the number of parallel tracking channels, global coverage, and the GNSS stations tracked. Increasing the number of tracked signals allows for a limited improvement in the revisit time, this plateau lowering with increasing GNSS transmitters that can potentially be tracked. Increasing the constellation size represents the only method to reach an arbitrarily low revisit time. This potentiality paves the way to a spread array of Earth observation applications with strict revisit time requirements. One of the most interesting for its key role in worldwide economic and social activities, i.e., sea target detection, has been explored, theoretically assessed and also experimentally validated using UK TDS-1 data. The target detector consists of four processing stages: in the pre-processing stage the sea clutter contribution is estimated in the delay-Doppler domain by means of a least square approach via the P^{2}EPS tool [196]; the sea clutter term is then subtracted from the actual DDM to form the target enhanced image. A CFAR thresholding is applied to provide the target candidates map in the pre-screening step. The selection stage reduces the false alarms rate by rejecting isolated detected targets. The ROC curves of the detector have been derived for the performance assessment. The validation of the proposed algorithm using actual GNSS-R imagery represents another contribution of this Ph.D. Thesis. The difficulties to exploit a proper ground-truth information about location of ships has been circumvented by testing the detector on an oil platform owing to the exploitation of ground truth about its location at no cost. Two UK TDS-1 DDMs acquired on the North Atlantic have been used to assess the capability of the algorithm to detect the Hibernia oil platform. Another case study has been defined in the Gulf of Mexico, due to its key role in worldwide sea trades. This feasibility study is essential to understand the role of upcoming GNSS-R constellations in the framework of sea target detection and feature mapping and could promote innovative solutions in the integration of remotely sensed data acquired by different sources.

7.2.1 Future Research Lines

A valid guideline for future research in the sea target detection from GNSS-R observables comes from the exploitation of DDM deconvolution methods in order to take advantage from the application of target detector to deconvolved GNSS-R data, e.g., the bistatic scattering coefficient. False alarms caused by noise or fast-moving targets, such as airplanes, can be reduced by multiple-images approaches, for example by further processing target maps related to consecutively acquired DDMs. Target location ambiguity is expected to benefit from this multi-look approach as well by analyzing the two candidate target tracks in a geographic coordinate system. The future spaceborne GNSS-R missions, such as CYGNSS, and GEROS, are expected to allow for an additional performance assessment of the proposed algorithm and an evaluation of its competitiveness in the field of sea target detection from remote sensing imagery.

This page intentionally left blank.

Bibliography

[1] J. B. Campbell and R. H. Wynne, *Introduction to Remote Sensing,* 5th ed., London, UK: The Guildford Press, 2011.

[2] C. Oliver and S. Quegan, *Understanding Synthetic Aperture Radar Images*, Raleigh, NC, USA: SciTech, 2004.

[3] R. Touzi, "A review of speckle filtering in the context of estimation theory," *IEEE Transactions on Geoscience and Remote Sensing,* vol. 40, no. 11, pp. 2392-2404, Nov. 2002.

[4] F. Argenti, A. Lapini, T. Bianchi, and L. Alparone, "A tutorial on speckle reduction in synthetic aperture radar images," *IEEE Geoscience and Remote Sensing Magazine,* vol. 1, no. 3, pp. 6–35, Sep. 2013.

[5] C.-A. Deledalle, L. Denis, G. Poggi, F. Tupin, and L. Verdoliva, "Exploiting Patch Similarity for SAR Image Processing: The nonlocal paradigm," *IEEE Signal Processing Magazine,* vol. 31, no. 4, pp. 69-78, July 2014.

[6] M. Levesque and H. Arsenault, "Combined homomorphic and local statistics processing for restoration of images degraded by signal dependent noise," *Applied Optics,* vol. 23, no. 6, pp. 845–850, Mar. 1984.

[7] P. F. Yan and C. H. Chen, “An algorithm for filtering multiplicative noise in wide range,” *Traitement du Signal,* vol. 3, no. 2, pp. 91–96, 1986.

[8] S. Solbo and T. Eltoft, “Homomorphic wavelet-based statistical despeckling of SAR images,” *IEEE Transactions on Geoscience and Remote Sensing,* vol. 42, no. 4, pp. 711–721, Apr. 2004.

[9] S. Chitroub, A. Houacine, and B. Sansal, “Statistical characterisation and modelling of SAR images,” *Signal Processing,* vol. 82, no. 1, pp. 69–92, Jan. 2002.

[10] A. Frery, H.-J. Muller, C. Yanasse, and S. Sant’Anna, “A model for extremely heterogeneous clutter,” *IEEE Transactions on Geoscience and Remote Sensing,* vol. 35, no. 3, pp. 648–659, May 1997.

[11] J. Goodman, “Some fundamental properties of speckle,” *Journal of the Optical Society of America,* vol. 66, no. 11, pp. 1145–1150, 1976.

[12] Y. Yu and S. T. Acton, “Speckle reducing anisotropic diffusion,” *IEEE Transactions on Image Processing,* vol. 11, no. 11, pp. 1260–1270, Nov. 2002.

[13] J. S. Lee, “Digital Image Enhancement and Noise Filtering by Use of Local Statistics,” *IEEE Transactions on Pattern Analysis and Machine Intelligence,* vol. PAMI-2, no. 2, pp. 165-168, Mar. 1980.

[14] J. S. Lee, “Refined filtering of image noise using local statistics,” *Computer Graphics and Image Processing,* vol. 15, no. 4, pp. 380–389, Apr. 1981.

[15] V. S. Frost, J. A. Stiles, K. S. Shanmugan, and J. C. Holtzman, “A model for radar images and its application to adaptive digital filtering of multiplicative noise,” *IEEE Transactions on Pattern Analysis and Machine Intelligence,* vol. PAMI-4, no. 2, pp. 157-166, Mar. 1982.

[16] D. T. Kuan, A. A. Sawchuk, T. C. Strand, and P. Chavel, "Adaptive noise smoothing filter for images with signal-dependent noise," *IEEE Transactions on Pattern Analysis and Machine Intelligence,* vol. PAMI-7, no. 2, pp. 165-177, Mar. 1985.

[17] R. Touzi, A. Lopes, and P. Bousquet, "A statistical and geometrical edge detector for SAR images," *IEEE Transactions on Geoscience and Remote Sensing,* vol. 26, no. 6, pp. 764-773, Nov. 1988.

[18] A. Lopes, R. Touzi, and E. Nezry, "Adaptive speckle filters and scene heterogeneity," *IEEE Transactions on Geoscience and Remote Sensing,* vol. 28, no. 6, pp. 992-1000, Nov. 1990.

[19] M. Hebar, D. Gleich, and Z. Cucej, "Autobinomial Model for SAR Image Despeckling and Information Extraction," *IEEE Transactions on Geoscience and Remote Sensing,* vol. 47, no. 8, pp. 2818-2835, Aug. 2009.

[20] A. Lopes, E. Nezry, R. Touzi, and H. Laur, "Maximum a posteriori speckle filtering and first order texture models in SAR images," in *10th Annual International Symposium on Geoscience and Remote Sensing,* vol. 3, pp. 2409–2412, May 1990.

[21] F. Argenti, T. Bianchi, and L. Alparone, "Multiresolution MAP despeckling of SAR images based on locally adaptive generalized Gaussian pdf modeling," *IEEE Transactions on Image Processing,* vol. 15, no. 11, pp. 3385–3399, Nov. 2006.

[22] T. Bianchi, F. Argenti, and L. Alparone, "Segmentation-based MAP despeckling of SAR images in the undecimated wavelet domain," *IEEE Transactions on Geoscience and Remote Sensing,* vol. 46, no. 9, pp. 2728–2742, Sep. 2008.

[23] Q. Gao, Y. Zhao, and Y. Lu, "Despeckling SAR images using stationary wavelet transform combining with directional filter banks," *Applied Mathematics and Computation,* vol. 205, no. 2, pp. 517–524, Nov. 2008.

[24] S. Parrilli, M. Poderico, C. V. Angelino, and L. Verdoliva, "A Nonlocal SAR Image Denoising Algorithm Based on LLMMSE Wavelet Shrinkage," *IEEE Transactions on Geoscience and Remote Sensing,* vol. 50, no. 2, pp. 606-616, Feb. 2012.

[25] A. Buades, B. Coll, and J. M. Morel, "A review of image denoising algorithms, with a new one," *Multiscale Modeling & Simulation,* vol. 4, no. 2, pp. 490–530, 2005.

[26] C.-A. Deledalle, L. Denis, and F. Tupin, "Iterative weighted maximum likelihood denoising with probabilistic patch-based weights," *IEEE Transactions on Image Processing,* vol. 18, no. 12, pp. 2661–2672, Dec. 2009.

[27] C.-A. Deledalle, L. Denis, F. Tupin, A. Reigber, and M. Jager, "NL-SAR: A unified nonlocal framework for resolution-preserving (Pol)(In)SAR denoising," *IEEE Transactions on Geoscience and Remote Sensing,* vol. 53, no. 4, pp. 2021–2038, Apr. 2015.

[28] G. Di Martino, D. Riccio, and I. Zinno, "SAR imaging of fractal surfaces," *IEEE Transactions on Geoscience and Remote Sensing,* vol. 50, no. 2, pp. 630–644, Feb. 2012.

[29] G. Franceschetti and R. Lanari, *Synthetic Aperture Radar (SAR) Processing,* New York, NY, USA: CRC Press, 1999.

[30] D. Robinson, K. Dewey, and R. Heim, "Global Snow Cover Monitoring: An Update," *Bulletin of American Meteorological Society,* vol. 74, no. 9, pp. 1689-1696, 1993.

[31] S. Brusch, S. Lehner, T. Fritz, M. Soccorsi, A. Soloviev, and B. van Schie, “Ship Surveillance With TerraSAR-X,” *IEEE Transactions on Geoscience and Remote Sensing,* vol. 49, no. 3, pp. 1092-1103, Mar. 2011.

[32] D. J. Crisp, “The state-of-the-art in ship detection in synthetic aperture radar imagery,” Aust. Gov., Dept. Def., Def. Sci. Technol. Org. (DSTO), Australia, Tech. Rep. DSTO-RR-0272, May 2004.

[33] C. Zhu, H. Zhou, R. Wang, and J. Guo, “A Novel Hierarchical Method of Ship Detection from Spaceborne Optical Image Based on Shape and Texture Features,” *IEEE Transactions on Geoscience and Remote Sensing,* vol. 48, no. 9, pp. 3446-3456, Sep. 2010.

[34] G. Yang, B. Li, S. Ji, F. Gao, and Q. Xu, “Ship Detection From Optical Satellite Images Based on Sea Surface Analysis,” *IEEE Geoscience and Remote Sensing Letters,* vol. 11, no. 3, pp. 641-645, Mar. 2014.

[35] P. Lombardo and M. Sciotti, “Segmentation-based technique for ship detection in SAR images,” in *IEE Proceedings - Radar, Sonar and Navigation,* vol. 148, no. 3, pp. 147-159, June 2001.

[36] “Sea-ice cover requirements,” OSCAR Observing Systems Capability Analysis and Review Tool, World Meteorological Organization, Geneva, Switzerland, [Online]. Available: `https://www.wmo-sat.info/oscar/variables/view/135`. [Accessed Jan. 16, 2017].

[37] V. Zavorotny and A. Voronovich, “Scattering of GPS signals from the ocean with wind remote sensing applications,” *IEEE Transactions on Geoscience and Remote Sensing,* vol. 38, no. 2, pp. 951-964, Mar. 2000.

[38] E. Valencia, A. Camps, N. Rodriguez-Alvarez, H. Park, and I. Ramos-Perez, “Using GNSS-R Imaging of the Ocean Surface for Oil Slick De-

tection," *IEEE Journal of Selected Topics in Applied Earth Observations and Remote Sensing,* vol. 6, no. 1, pp. 217-223, Feb. 2013.

[39] G. Carrie, T. Deloues, J. Mametsa, and S. Angelliaume, "Ship Detection Based on GNSS Reflected Signals: An Experimental Plan," in *Space Reflecto,* Oct. 2011.

[40] M. P. Clarizia, P. Braca, C. S. Ruf, and P. Willett, "Target detection using GPS signals of opportunity," in *2015 18th International Conference on Information Fusion (Fusion),* pp. 1429-1436, July 2015.

[41] W. Ji, C. Xiu, W. Li, and L. Wang, "Ocean surface target detection and positioning using the spaceborne GNSS-R Delay-Doppler maps," in *2014 IEEE International Geoscience and Remote Sensing Symposium (IGARSS),* pp. 3806-3809, July 2014.

[42] Y. Lu, D. Yang, W. Li, J. Ding, and Z. Li, "Study on the New Methods of Ship Object Detection Based on GNSS Reflection," *Marine Geodesy,* vol. 36, no. 1, pp. 22-30, 2013.

[43] C. Kabakchiev, I. Garvanov, V. Behar, and H. Rohling, "The Experimental Study of Possibility for Radar Target Detection in FSR Using L1-Based Non-Cooperative Transmitter," in *2013 14th International Radar Symposium (IRS),* vol. 2, pp. 625-630, June 2013.

[44] O. Darrigol, *A History of Optics from Greek Antiquity to the Nineteenth Century,* Oxford, UK: Oxford University Press, 2012.

[45] G. Franceschetti and D. Riccio, *Scattering, Natural Surfaces and Fractals,* Burlington, MA, USA: Academic, 2007.

[46] L. Tsang, J. A. Kong, and K. Ding, *Scattering of Electromagnetic Waves, Theories and Applications,* New York, NY, USA: John Wiley, 2000.

[47] F. T. Ulaby, R. K. Moore, and A. K. Fung, *Microwave Remote Sensing: Active and Passive,* Reading, MA, USA: Addison-Wesley, 1981.

[48] A. K. Fung, Z. Li, and K. S. Chen, "Backscattering from a Randomly Rough Dielectric Surface," *IEEE Transactions on Geoscience and Remote Sensing,* vol. 30, no. 2, pp. 356-369, Mar. 1992.

[49] P. Beckmann and A. Spizzichino, *The Scattering of Electromagnetic Waves from Rough Surfaces,* Norwood, MA, USA: Artech House, 1987.

[50] L. Tsang and J. A. Kong, *Scattering of Electromagnetic Waves, Advanced Topics,* New York, NY, USA: John Wiley & Sons, 2001.

[51] M. F. Chew and A. K. Fung, "A Numerical Study of the Regions of Validity of the Kirchhoff and Small-Perturbation Rough Surface Scattering Models," *Radio Science,* vol. 23, no. 2, pp. 163–170, Mar. 1988.

[52] W. C. Chew, *Waves and Fields in Inhomogeneous Media*, New York, NY, USA: IEEE Press, 1995.

[53] A. J. Poggio and E. K. Miller, *Computed Techniques for Electromagnetics*, New York, NY, USA: Pergamon, 1973, ch. 4.

[54] B. Mandelbrot, *The Fractal Geometry of Nature,* New York, NY, USA: Freeman, 1983.

[55] K. Falconer, *Fractal Geometry,* Chichester, UK: John Wiley, 1990.

[56] J. S. Feder, *Fractals,* New York, NY, USA: Plenum Press, 1988.

[57] M. K. Shepard, B. A. Campbell, M. H. Bulmer, T. G. Farr, and L. R. Gaddis, "The roughness of natural terrain: A planetary and remote sensing perspective," *Journal of Geophysical Research,* vol. 106, no. E12, pp. 32777-32795, Dec. 2001.

[58] W. Dierking, "Quantitative Roughness Characterization of Geological Surfaces and Implications for Radar Signature Analysis," *IEEE Transactions on Geoscience and Remote Sensing,* vol. 37, no. 5, pp. 2397-2412, Sep. 1999.

[59] D. L. Evans, T. J. Farr, and J. J. van Zyl, "Estimates of Surface Roughness Derived from Synthetic Aperture Radar (SAR) Data," *IEEE Transactions on Geoscience and Remote Sensing,* vol. 30, no. 2, pp. 382-389, Mar. 1992.

[60] G. Franceschetti, A. Iodice, M. Migliaccio, and D. Riccio, "Fractals and the small perturbation scattering model," *Radio Science,* vol. 34, no. 5, pp. 1043-1054, Sep.-Oct. 1999.

[61] G. Franceschetti, A. Iodice, S. Maddaluno, and D. Riccio, "A Fractal-Based Theoretical Framework for Retrieval of Surface Parameters from Electromagnetic Backscattering Data," *IEEE Transactions on Geoscience and Remote Sensing,* vol. 38, no. 2, pp. 641-650, Mar. 2000.

[62] J. C. Curlander and R. N. McDonough, *Synthetic Aperture Radar: Systems and Signal Processing*, New York, NY, USA: Wiley-Interscience, 1991.

[63] H. Maitre, *Processing of Synthetic Aperture Radar (SAR) Images*, Hoboken, NJ, USA: John Wiley & Sons, 2008.

[64] D. Massonnet and J.-C. Souyris, *Imaging with Synthetic Aperture Radar*, Lausanne, Switzerland: EPFL Press, 2008.

[65] R. O. Harger, *Synthetic Aperture Radar System: Theory and Design*, New York, NY, USA: Academic Press, 1970.

[66] W. G. Carrara, R. S. Goodman, and R. M. Majewski, *Spotlight Synthetic Aperture Radar: Signal Processing Algorithms*, Norwood, MA, USA: Artech House, 1995.

[67] D. R. Wehner, *High Resolution Radar*, Norwood, MA, USA: Artech House, 1987.

[68] I. S. Robinson, *Satellite Oceanography: An Introduction for Oceanographers and Remote Sensing Scientists,* New York, NY, USA: John Wiley & Sons, 1985.

[69] C. Elachi, *Spaceborne Radar Remote Sensing: Applications and Techniques*, New York, NY, USA: IEEE Press, 1988.

[70] C. A. Wiley, "Pulsed Doppler radar methods and apparatus," U.S. Patent 3196436 A, 1965.

[71] C. Elachi, "Radar Images of the Earth from Space," *Scientific American,* vol. 247, no. 6, pp. 54-61, Dec. 1982.

[72] L. E. Roth and S. D. Wall, *The Face of Venus, the Magellan Radar-Mapping Mission,* NASA Technical Documents, June 1995.

[73] G. Ruello *et al.,* "Synthesis, construction and validation of a fractal surface," *IEEE Transactions on Geoscience and Remote Sensing,* vol. 44, no. 6, pp. 1403-1412, June 2006.

[74] T. F. Bush and F. T. Ulaby, "Fading Characteristics of Panchromatic Radar Backscatter from Selected Agricultural Targets," *IEEE Transactions on Geoscience Electronics,* vol. 13, no. 4, pp. 149-157, Oct. 1975.

[75] J.-S. Lee, "A simple speckle smoothing algorithm for synthetic aperture radar images," *IEEE Transactions on Systems, Man, and Cybernetics,* vol. SMC-13, no. 1, pp. 85–89, Jan. 1983.

[76] G. V. Trunk, "Radar Properties of Non-Rayleigh Sea Echo," *IEEE Transactions on Aerospace and Electronic Systems,* vol. AES-8, no. 2, pp. 196-204, Mar. 1972.

[77] G. V. Trunk and S. E. George, “Detection of Targets in Non-Gaussian Sea Clutter,” *IEEE Transactions on Aerospace and Electronic Systems,* vol. AES-6, no. 5, pp. 620-628, Sep. 1970.

[78] D. C. Schleher, “Radar detection in lognormal clutter,” in *IEEE International Radar Conference,* pp. 262-267, Apr. 1975.

[79] G. R. Valenzuela and M. B. Laing, “Point-Scatterer Formulation of Terrain Clutter Statistics,” Naval Research Laboratory Report 7459, Washington, DC, 1972.

[80] M. P. Warden, “An Experimental Study of Some Clutter Characteristics,” in *AGARD Conference on Advanced Radar Systems,* no. 66, May 1970.

[81] D. C. Schleher, “Radar Detection in Weibull Clutter,” *IEEE Transactions on Aerospace and Electronic Systems,* vol. AES-12, no. 6, pp. 736-743, Nov. 1976.

[82] E. A. Fay, J. Clarke, and R. S. Peters, “Weibull Distribution Applied to Sea Clutter,” in *International Conference on Radar RADAR ’77*, no. 155, pp. 101-104, London: IEE, 1977.

[83] M. Sekine, T. Musha, Y. Tomita, T. Hagisawa, T. Irabu, and E. Kiuchi, “Weibull-Distributed Sea Clutter,” *Communications, Radar and Signal Processing, IEE Proceedings*, vol. 130, no. 5, p. 476, Aug. 1983.

[84] H. Ogawa, M. Sekine, T Musha, M. Aota, M. Ohi, and H. Fukushi, “Weibull-Distributed Radar Clutter Reflected from Sea Ice,” *IEICE Transactions*, vol. E70, no. 2, pp. 116-120, Feb. 1987.

[85] M. Sekine, T. Musha, Y. Tomita, T. Hagisawa, T. Irabu, and E. Kiuchi, “On Weibull-Distributed Weather Clutter,” *IEEE Transactions on Aerospace and Electronic Systems,* vol. AES-15, no. 6, pp. 824-830, Nov. 1979.

[86] R. Booth, “The Weibull Distribution Applied to the Ground Clutter Backscatter Coefficient,” U.S. Army Missile Command, Tech. Rep. RE-TR-69-15, ASTIA Doc. AD 691109, 1969.

[87] M. Sekine, S. Ohtani, T. Musha, T. Irabu, E. Kiuchi, T. Hagisawa, and Y. Tomita, “Weibull-Distributed Ground Clutter,” *IEEE Transactions on Aerospace and Electronic Systems,* vol. AES-17, no. 4, pp. 596-598, July 1981.

[88] K. D. Ward, “Compound Representation of High Resolution Sea Clutter,” *Electronics Letters,* vol. 17, no. 16, pp. 561-565, Aug. 1981.

[89] E. Jakeman and P. N. Pusey, “A Model for Non-Rayleigh Sea Echo,” *IEEE Transactions on Antennas and Propagation,* vol. 24, no. 6, pp. 806-814, Nov. 1976.

[90] C. J. Oliver, “Optimum Texture Estimators for SAR Clutter,” *Journal of Physics D: Applied Physics,* vol. 26, no. 11, pp. 1824-1835, 1993.

[91] K. D. Ward, “A Radar Sea Clutter Model and Its Application to Performance Assessment,” in *International Conference on Radar RADAR ’82,* no. 216, pp. 203-207, London: IEE, 1982.

[92] C. J. Oliver, “A Model for Non-Rayleigh Scattering Statistics,” *Optica Acta: International Journal of Optics,* vol. 31, no. 6, pp. 701-722, 1984.

[93] R. Fante, “Detection of multiscatter targets in K -distributed clutter,” *IEEE Transactions on Antennas and Propagation,* vol. 32, no. 12, pp. 1358-1363, Dec. 1984.

[94] D. E. Kreithen, S. M. Crooks, W. W. Irving, and S. D. Halversen, “Estimation and Detection Using the Product Model,” MIT-Lincoln Lab. Report no. STD-37, 1991.

[95] F. Soulat, "Sea Surface Remote Sensing with GNSS and Sunlight Reflections," Ph.D. dissertation, Universitat Politecnica de Catalunya, Barcelona, Spain, 2003.

[96] G. Gibbons, "China GNSS 101. Compass in the rearview mirror," *Inside GNSS Magazine*, pp. 62-66, Jan./Feb. 2008.

[97] B. Hofmann-Wellenhof, H. Lichtenegger, E. Wasle, *GNSS – Global Navigation Satellite Systems,* Wien, Austria: Springer-Verlag, 2008.

[98] S. Feairheller and R. Clark, "Other satellite navigation systems," in E. D. Kaplan and C. J. Hegarty, *Understanding GPS – principles and applications,* 2nd ed., Norwood, MA, USA: Artech House, 2006.

[99] H. Habrich, *Geodetic applications of the global navigation satellite system (GLONASS) and of GLONASS/GPS combinations,* Ph.D. dissertation, University of Bern, Bern, Switzerland, 1999.

[100] S. G. Revnivykh, "GLONASS status update," in *UN/Zambia/ESA Regional Workshop on the Applications of Global Navigation Satellite System Technologies in Sub-Saharan Africa,* June 2006.

[101] "First Galileo Signals Received," British Broadcasting Corporation (BBC) Web site, January 13, 2006, [Online]. Available: `http://news.bbc.co.uk/2/hi/science/nature/4610452.stm`. [Accessed Nov. 30, 2016].

[102] Inside GNSS, "China Launches Another Compass GEO Navigation Satellite," June 11, 2010, [Online]. Available: `http://www.insidegnss.com/node/2134`. [Accessed Dec. 2, 2016].

[103] C. Shi *et al.,* "Precise orbit determination of Beidou Satellites with precise positioning," *SCIENCE CHINA Earth Sciences,* vol. 55, no. 7, pp. 1079-1086, 2012.

[104] EBSCO, “Galileo, Compass on Collision Course,” *GPS World,* vol. 19, no. 4, p. 27, Apr. 2008.

[105] T. Grelier, J. Dantepal, A. Delatour, A. Ghion, L. Ries, “Initial observation and analysis of Compass MEO satellite signals,” *Inside GNSS Magazine*, pp. 39-43, May/June 2007.

[106] G. X. Gao, A. Chen, S. Lo, D. De Lorenzo, and P. Enge, “GNSS over China. The Compass MEO satellite codes,” *Inside GNSS Magazine,* pp. 36–43, Jul./Aug. 2007.

[107] G. X. Gao, A. Chen, S. Lo, D. De Lorenzo, and P. Enge, “Compass-M1 broadcast codes and their application to acquisition and tracking,” in *ION National Technical Meeting 2008,* pp. 133-141, Jan. 2008.

[108] W. De Wilde, F. Boon, J.-M. Sleewaegen, and F. Wilms, “More Compass points. Tracking China’s MEO satellite on a hardware receiver,” *Inside GNSS Magazine,* pp. 44–48, Jul./Aug. 2007.

[109] S. Gleason, *Remote Sensing of Ocean, Land and Ice Surfaces Using Bistatically Scattered GNSS Signals From Low Earth Orbit,* Ph.D. dissertation, University of Surrey, Guildford, UK, 2006.

[110] G. Fjeldbo, A. J. Kliore, and V. R. Eshleman, “The Neutral Atmosphere of Venus as Studied with the Mariner V Radio Occultation Experiments,” *Astronomical Journal,* vol. 76, pp. 123–140, Mar. 1971.

[111] G. L. Tyler, “Radio Occultation Experiments in the Outer Solar System with Voyager,” in *Proceedings of the IEEE,* vol. 75, no. 10, pp. 1404–1431, Nov. 1987.

[112] T. P. Yunck, G. F. Lindal, and C.-H. Liu, “The role of GPS in precise Earth observation,” in *IEEE Position Location and Navigation Symposium (PLANS ’88),* pp. 251-258, Nov.-Dec. 1988.

[113] W. G. Melbourne *et al.,* “The Application of Spaceborne GPS to Atmospheric Limb Sounding and Global Change Monitoring,” *JPL Publication,* art. ID 19960008694, June 1994.

[114] E. R. Kursinski *et al.,* “Observing Earth’s Atmosphere with Radio Occultation Measurements Using the Global Positioning System,” *Journal of Geophysical Research,* vol. 102, no. D19, pp. 23429–23465, Oct. 1997.

[115] E. R. Kursinski, G. A. Hajj, S. S. Leroy, and B. Herman, “The GPS radio occultation technique,” *Terrestrial, Atmospheric and Oceanic Sciences,* vol. 11, no. 1, pp. 53–114, 2000.

[116] C. Rocken *et al.,* “Analysis and validation of GPS/MET data in the neutral atmosphere,” *Journal of Geophysical Research,* vol. 102, no. D25, pp. 29849–29866, Dec. 1997.

[117] S. Gleason and D. Gebre-Egziabher, *GNSS Applications and Methods,* Norwood, MA, USA: Artech House, 2009.

[118] B. Lusignan *et al.,* “Sensing the Earth’s Atmosphere with Occultation Satellites,” in *Proceedings of the IEEE,* vol. 57, no. 4, pp. 458–467, Apr. 1969.

[119] C. Hall and R. R. Cordey, “Multistatic Scatterometry,” in *IEEE International Geoscience and Remote Sensing Symposium (IGARSS),* pp. 561-562, Sep. 1988.

[120] M. Martin-Neira, “A Passive Reflectometry and Interferometry System (PARIS): Application to Ocean Altimetry,” *ESA Journal,* vol. 17, no. 4, pp. 331-355, Jan. 1993.

[121] J. L. Garrison, S. J. Katzberg, and M. I. Hill, “Effect of Sea Roughness on Bistatically Scattered Range Coded Signals from the Global

Positioning System," *Geophysical Research Letters,* vol. 25, no. 13, pp. 2257–2260, July 1998.

[122] S. Lowe *et al.,* "First Spaceborne Observation of an Earth-Reflected GPS Signal," *Radio Science,* vol. 37, no. 1, Jan. 2002.

[123] M. P. Clarizia and C. S. Ruf, "Wind Speed Retrieval Algorithm for the Cyclone Global Navigation Satellite System (CYGNSS) Mission," *IEEE Transactions on Geoscience and Remote Sensing,* vol. 54, no. 8, pp. 4419-4432, Aug. 2016.

[124] J. L. Garrison, A. Komjathy, V. U. Zavorotny, and S. J. Katzberg, "Wind Speed Measurements Using Forward Scattered GPS Signals," *IEEE Transactions on Geoscience and Remote Sensing,* vol. 40, no. 1, pp. 50–65, Jan. 2002.

[125] A. Komjathy, J. Maslanik, V. U. Zavorotny, P. Axelrad, and S. J. Katzberg, "Sea Ice Remote Sensing Using Surface Reflected GPS Signals," in *IEEE International Geoscience and Remote Sensing Symposium (IGARSS),* vol. 7, pp. 2855–2857, July 2000.

[126] S. Lowe *et al.,* "5-ms-Precision Aircraft Ocean Altimetry Using GPS Signals," *Geophysical Research Letters,* vol. 29, no. 10, pp. 1375-1378, 2002.

[127] G. Ruffini, F. Soulat, M. Caparrini, O. Germain, and M. Martín-Neira, "The Eddy Experiment: Accurate GNSS-R Ocean Altimetry from Low Altitude Aircraft," *Geophysical Research Letters,* vol. 31, no. 12, June 2004.

[128] S. J. Katzberg, O. Torres, M. S. Grant, and D. Masters, "Utilizing Calibrated GPS Reflected Signals to Estimate Soil Reflectivity and Dielectric Constant: Results From SMEX 2," *Remote Sensing of Environment,* vol. 100, no. 1, pp. 17-28, Jan. 2006.

[129] S. Gleason *et al.,* "Detection and processing of bistatically reflected GPS signals from low-earth orbit, for the purpose of ocean remote sensing," *IEEE Transactions on Geoscience and Remote Sensing,* vol. 43, no. 6, pp. 1229-1241, June 2005.

[130] J. Shuanggen, E. Cardellach, and F. Xie, *GNSS Remote Sensing - Theory, Methods and Applications,* Berlin, Germany: Springer-Verlag, 2014.

[131] E. Cardellach, F. Fabra, O. Nogués-Correig, S. Oliveras, S. Ribó, and A. Rius, "GNSS-R ground-based and airborne campaigns for ocean, land, ice, and snow techniques: application to the GOLD-RTR data sets," *Radio Science,* vol. 46, no. RS0C04, Dec. 2011.

[132] E. Nezry, A. Lopes, and R. Touzi, "Detection of structural and textural features for SAR images filtering," in *IEEE International Geoscience and Remote Sensing Symposium (IGARSS),* vol. 4, pp. 2169-2172, June 1991.

[133] M. Walessa and M. Datcu, "Model-based despeckling and information extraction from SAR images," *IEEE Transactions on Geoscience and Remote Sensing,* vol. 38, no. 5, pp. 2258-2269, Sep. 2000.

[134] F. Argenti and L. Alparone, "Speckle removal from SAR images in the undecimated wavelet domain," *IEEE Transactions on Geoscience and Remote Sensing,* vol. 40, no. 11, pp. 2363-2374, Nov. 2002.

[135] J. J. Ranjani and S. J. Thiruvengadam, "Dual-Tree Complex Wavelet Transform Based SAR Despeckling Using Interscale Dependence," *IEEE Transactions on Geoscience and Remote Sensing,* vol. 48, no. 6, pp. 2723-2731, June 2010.

[136] S. Foucher, G. Bénié, and J. Boucher, "Multiscale MAP filtering of SAR images," *IEEE Transactions on Image Processing,* vol. 10, no. 1, pp. 49-60, Jan. 2001.

[137] W. Zhang, F. Liu, L. Jiao, B. Hou, S. Wang, and R. Shang, "SAR image despeckling using edge detection and feature clustering in bandelet domain," *IEEE Geoscience and Remote Sensing Letters,* vol. 7, no. 1, pp. 131-135, Jan. 2010.

[138] Y. Li, H. Gong, D. Feng, and Y. Zhang, "An adaptive method of speckle reduction and feature enhancement for SAR images based on curvelet transform and particle swarm optimization," *IEEE Transactions on Geoscience and Remote Sensing,* vol. 49, no. 8, pp. 3105-3116, Aug. 2011.

[139] S. Foucher, "SAR image filtering via learned dictionaries and sparse representations," in *2008 IEEE International Geoscience and Remote Sensing Symposium (IGARSS),* vol. 1, pp. 229-232, July 2008.

[140] Y. Huang, L. Moisan, M. K. Ng, and T. Zeng, "Multiplicative noise removal via a learned dictionary," *IEEE Transactions on Image Processing,* vol. 21, no. 11, pp. 4534-4543, Nov. 2012.

[141] B. Xu, Y. Cui, Z. Li, and J. Yang, "An iterative SAR image filtering method using nonlocal sparse model," *IEEE Geoscience and Remote Sensing Letters,* vol. 12, no. 8, pp. 1635-1639, Aug. 2015.

[142] J.-S. Lee, "Digital image smoothing and the sigma filter," *Computer Vision, Graphics, and Image Processing,* vol. 24, no. 2, pp. 255–269, 1983.

[143] J.-S. Lee, J.-H. Wen, T. L. Ainsworth, K.-S. Chen, and A. J. Chen, "Improved sigma filter for speckle filtering of SAR imagery," *IEEE*

Transactions on Geoscience and Remote Sensing, vol. 47, no. 1, pp. 202-213, Jan. 2009.

[144] D. Cozzolino, S. Parrilli, G. Scarpa, G. Poggi, and L. Verdoliva, "Fast adaptive nonlocal SAR despeckling," *IEEE Geoscience and Remote Sensing Letters,* vol. 11, no. 2, pp. 524-528, Feb. 2014.

[145] G. Di Martino, M. Poderico, G. Poggi, D. Riccio, and L. Verdoliva, "Benchmarking framework for SAR despeckling," *IEEE Transactions on Geoscience and Remote Sensing,* vol. 52, no. 3, pp. 1596–1615, Mar. 2014.

[146] K. Dabov, A. Foi, V. Katkovnik, and K. Egiazarian, "Image denoising by sparse 3-D transform-domain collaborative filtering," *IEEE Transactions on Image Processing,* vol. 16, no. 8, pp. 2080–2095, Aug. 2007.

[147] C.-A. Deledalle, L. Denis, and F. Tupin, "How to compare noisy patches? Patch similarity beyond Gaussian noise," *International Journal of Computer Vision,* vol. 99, no. 1, pp. 86–102, Aug. 2012.

[148] O. D'Hondt, S. Guillaso, and O. Hellwich, "Iterative bilateral filtering of polarimetric SAR data," *IEEE Journal of Selected Topics in Applied Earth Observations and Remote Sensing,* vol. 6, no. 3, pp. 1628–1639, June 2013.

[149] L. Torres, S. J. S. SantAnna, C. da Costa Freitas, and A. C. Frery, "Speckle reduction in polarimetric SAR imagery with stochastic distances and nonlocal means," *Pattern Recognition,* vol. 47, no. 1, pp. 141–157, Jan. 2014.

[150] L. Verdoliva, R. Gaetano, G. Ruello, and G. Poggi, "Optical-driven non-local SAR despeckling," *IEEE Geoscience and Remote Sensing Letters,* vol. 12, no. 2, pp. 314–318, Feb. 2015.

[151] H. Xie, L. Pierce, and F. Ulaby, “Statistical properties of logarithmically transformed speckle,” *IEEE Transactions on Geoscience and Remote Sensing,* vol. 40, no. 3, pp. 721–727, Mar. 2002.

[152] J.-S. Lee, M. Grunes, D. Schuler, E. Pottier, and L. Ferro-Famil, “Scattering-model-based speckle filtering of polarimetric SAR data,” *IEEE Transactions on Geoscience and Remote Sensing,* vol. 44, no. 1, pp. 176-187, Jan. 2006.

[153] T. G. Farr *et al.,* “The Shuttle Radar Topography Mission,” *Reviews of Geophysics,* vol. 45, no. RG2004, May 2007.

[154] “Earth Explorer,” U.S. Geological Survey, Reston, VA, USA, [Online]. Available: `http://earthexplorer.usgs.gov/`. [Accessed Feb. 11, 2015].

[155] A. Lopes, E. Nezry, R. Touzi, and H. Laur, “Structure detection and statistical adaptive speckle filtering in SAR images,” *International Journal of Remote Sensing,* vol. 14, no. 9, pp. 1735-1758, 1993.

[156] D. Gragnaniello, G. Poggi, G. Scarpa, and L. Verdoliva, “SAR Despeckling Based on Soft Classification,” in *2015 IEEE International Geoscience and Remote Sensing Symposium (IGARSS),* pp. 2378-2381, July 2015.

[157] G. Franceschetti, M. Migliaccio, D. Riccio, and G. Schirinzi, “SARAS: A SAR raw signal simulator,” *IEEE Transactions on Geoscience and Remote Sensing,* vol. 30, no. 1, pp. 110–123, Jan. 1992.

[158] Z. Wang, A. C. Bovik, H. R. Sheikh, and E. P. Simoncelli, “Image quality assessment: from error visibility to structural similarity,” *IEEE Transactions on Image Processing*, vol. 13, no. 4, pp. 600-612, Apr. 2004.

[159] "COSMO-SkyMed System Description and User Guide," Italian Space Agency (ASI), Rome, Italy, [Online]. Available: http://www.cosmoskymed.it/docs/ASI-CSM-ENG-RS-093-A-CSKSysDescriptionAndUserGuide.pdf.

[160] U.S.I.T.C.- città metropolitana di Napoli, [Online]. Available: http://sit.cittametropolitana.na.it/lidar.html. [Accessed Feb. 11, 2015].

[161] A. G. Bors, E. R. Hancock, and R. C. Wilson, "Terrain Analysis Using Radar Shape-from-Shading," *IEEE Transactions on Pattern Analysis & Machine Intelligence,* vol. 25, no. 8, pp. 974-992, Aug. 2003.

[162] B. K. P. Horn and M. J. Brooks, *Shape From Shading,* Cambridge, MA, USA: MIT Press, 1989.

[163] R. T. Frankot and R. Chellappa, "Estimation of Surface Topography from SAR Imagery Using Shape from Shading Techniques," *Artificial Intelligence,* vol. 43, no. 3, pp. 271-310, June 1990.

[164] B. K. P. Horn, "Obtaining shapes from shading information," in B. K. P. Horn and M. J. Brooks, *Shape from Shading,* pp. 115-155, Cambridge, MA, USA: MIT Press, 1989.

[165] D. N. Ostrov, "Boundary Conditions and Fast Algorithms for Surface Reconstructions from Synthetic Aperture Radar Data," *IEEE Transactions on Geoscience and Remote Sensing,* vol. 37, no. 1, pp. 335-346, Jan. 1999.

[166] G. Di Martino, A. Iodice, D. Riccio, G. Ruello, and I. Zinno, "Angle Independence Properties of Fractal Dimension Maps Estimated from SAR Data," *IEEE Journal of Selected Topics in Applied Earth Observations and Remote Sensing,* vol. 6, no. 3, pp. 1242-1253, June 2013.

[167] A. Iodice, A. Natale, and D. Riccio, "Retrieval of Soil Surface Parameters via a Polarimetric Two-Scale Model," *IEEE Transactions on Geoscience and Remote Sensing,* vol. 49, no. 7, pp. 2531-2547, July 2011.

[168] "Global 30 Arc-Second Elevation (GTOPO30)," U.S. Geological Survey, Reston, VA, USA, [Online]. Available: `https://lta.cr.usgs.gov/GTOPO30`.

[169] A. Gambardella, F. Nunziata, and M. Migliaccio, "A physical full-resolution SAR ship detection filter," *IEEE Geoscience and Remote Sensing Letters,* vol. 5, no. 4, pp. 760-763, Oct. 2008.

[170] "U.S. National Ice Center - Current Daily Ice Analysis," U.S. National Ice Center, Suitland, MD, USA, [Online]. Available: `http://www.natice.noaa.gov/Main_Products.htm`. [Accessed Jan. 16, 2017].

[171] P. Iervolino, R. Guida, and P. Whittaker, "A Model for the Backscattering From a Canonical Ship in SAR Imagery," *IEEE Journal of Selected Topics in Applied Earth Observations and Remote Sensing,* vol. 9, no. 3, pp. 1163-1175, Mar. 2016.

[172] United Nations, "Review of Maritime Transport - 2014," in *United Nations Conference on Trade and Development (UNCTAD),* 2014.

[173] S. Ramongassie *et. al.,* "Radar and AIS sensors constellation for global maritime surveillance," in *2010 IEEE International Geoscience and Remote Sensing Symposium (IGARSS),* pp. 3793-3796, July 2010.

[174] M. P. Clarizia, C. S. Ruf, P. Jales, and C. Gommenginger, "Spaceborne GNSS-R Minimum Variance Wind Speed Estimator," *IEEE Transactions on Geoscience and Remote Sensing,* vol. 52, no. 11, pp. 6829-6843, Nov. 2014.

[175] E. Valencia *et al.,* "Ocean surface's scattering coefficient retrieval by delay-Doppler map inversion," *IEEE Geoscience and Remote Sensing Letters,* vol. 8, no. 4, pp. 750-754, July 2011.

[176] D. Schiavulli, F. Nunziata, G. Pugliano, and M. Migliaccio, "Reconstruction of the normalized radar cross section field from GNSS-R delay-Doppler map," *IEEE Journal of Selected Topics in Applied Earth Observations and Remote Sensing,* vol. 7, no. 5, pp. 1573-1583, May 2014.

[177] M. P. Clarizia, C. Ruf, P. Cipollini, and C. Zuffada, "First spaceborne observation of sea surface height using GPS-Reflectometry," *Geophysical Research Letters,* vol. 43, no. 2, pp. 767-774, Jan. 2016.

[178] C. Li, W. Huang, and S. Gleason, "Dual antenna space-based GNSS-R ocean surface mapping: Oil slick and tropical cyclone sensing," *IEEE Journal of Selected Topics in Applied Earth Observations and Remote Sensing,* vol. 8, no. 1, pp. 425-435, Jan. 2015.

[179] Q. Yan and W. Huang, "GNSS-R Delay-Doppler map simulation based on the 2004 Sumatra-Andaman tsunami event," *Journal of Sensors,* vol. 2016, art. ID 2750862, 2016.

[180] Q. Yan and W. Huang, "Tsunami detection and parameter estimation from GNSS-R delay-Doppler map," *IEEE Journal of Selected Topics in Applied Earth Observations and Remote Sensing,* vol. 9, no. 10, pp. 4650-4659, Oct. 2016.

[181] H. Carreno-Luengo *et al.,* "3Cat-2—An Experimental Nanosatellite for GNSS-R Earth Observation: Mission Concept and Analysis," *IEEE Journal of Selected Topics in Applied Earth Observations and Remote Sensing,* vol. 9, no. 10, pp. 4540-4551, Oct. 2016.

[182] S. Gleason, “Space Reflected GNSS Signals Detected off an Ice Sheet in an Alaskan Sound and from a Diverse Land Surface in the Plains of North America,” in *GNSS-R Workshop,* June 2005.

[183] A. Alonso Arroyo, V. U. Zavorotny, and A. Camps, “Sea ice detection using GNSS-R data from UK TDS-1,” in *2016 IEEE International Geoscience and Remote Sensing Symposium (IGARSS),* pp. 2001-2004, July 2016.

[184] M. Wiehl, B. Legrésy and R. Dietrich, “Potential of Reflected GNSS Signals for Ice Sheet Remote Sensing,” *Progress in Electromagnetics Research,* vol. 40, pp. 177-205, 2003.

[185] K. Eldhuset, “An automatic ship and ship wake detection system for spaceborne SAR images in coastal regions,” *IEEE Transactions on Geoscience and Remote Sensing,* vol. 34, no. 4, pp. 1010-1019, July 1996.

[186] “TerraSAR-X Ground Segment Basic Product Specification Document,” German Aerospace Center (DLR), Germany, [Online]. Available: `http://www.intelligence-airbusds.com/files/pmedia/public/r466_9_tx-gs-dd-3302_basic-product-specification-document_1_9.pdf`. [Accessed Dec. 16, 2016].

[187] “Sentinel-1 User Handbook,” European Space Agency (ESA), Paris, France, [Online]. Available: `https://sentinel.esa.int/documents/247904/685163/Sentinel-1_User_Handbook`. [Accessed Dec. 16, 2016].

[188] “SPOT – Accuracy and Coverage Combined,” Astrium, Paris, France, [Online]. Available: `http://www.intelligence-airbusds.com/files/pmedia/public/r233_9_geo_0013_spot_en_low.pdf`. [Accessed Dec. 16, 2016].

[189] "Landsat 7 User Guide," National Aeronautics and Space Administration (NASA), Washington, DC, USA, [Online]. Available: http://landsathandbook.gsfc.nasa.gov/pdfs/Landsat7_Handbook.pdf. [Accessed Dec. 16, 2016].

[190] "Sentinel-2 User Handbook," European Space Agency (ESA), Paris, France, [Online]. Available: https://sentinel.esa.int/documents/247904/685211/Sentinel-2_User_Handbook. [Accessed Dec. 16, 2016].

[191] "CYGNSS," University of Michigan, Ann Arbor, MI, [Online]. Available: http://clasp-research.engin.umich.edu/missions/cygnss/science.php. [Accessed Dec. 16, 2016].

[192] R. Olive, A. Amezaga, H. Carreno-Luengo, H. Park, and A. Camps, "Implementation of a GNSS-R Payload Based on Software-Defined Radio for the 3CAT-2 Mission," *IEEE Journal of Selected Topics in Applied Earth Observations and Remote Sensing,* vol. 9, no. 10, pp. 4824-4833, Oct. 2016.

[193] "Shoreline database," National Oceanic and Atmospheric Administration (NOAA), Silver Spring, MD, USA, [Online]. Available: https://www.ngdc.noaa.gov/mgg/shorelines/. [Accessed Sep. 19, 2016].

[194] M. Tello, C. Lopez-Martinez, and J. J. Mallorqui, "A novel algorithm for ship detection in SAR imagery based on the wavelet transform," *IEEE Geoscience and Remote Sensing Letters,* vol. 2, no. 2, pp. 201-205, Apr. 2005.

[195] A. Marino, M. Sugimoto, K. Ouchi, and I. Hajnsek, "Validating a Notch Filter for Detection of Targets at Sea With ALOS-PALSAR Data: Tokyo Bay," *IEEE Journal of Selected Topics in Applied Earth*

Observations and Remote Sensing, vol. 7, no. 12, pp. 4907-4918, Dec. 2014.

[196] H. Park, A. Camps, D. Pascual, R. Onrubia, A. Alonso-Arroyo, and F. Martin, "Evolution of PAU/PARIS End-to-end Performance Simulator (P2EPS) towards GNSS reflectometry, radio occulation and Scatterometry simulator (GEROS-SIM)," in *2015 IEEE International Geoscience and Remote Sensing Symposium (IGARSS),* pp. 4757-4760, July 2015.

[197] H. Park *et al.,* "Retracking considerations in spaceborne GNSS-R altimetry," *GPS Solutions,* vol. 16, no. 4, pp. 507-518, Jan. 2012.

[198] J. F. Marchan-Hernandez, A. Camps, N. Rodriguez-Alvarez, E. Valencia, X. Bosch-Lluis, and I. Ramos-Perez, "An Efficient Algorithm to the Simulation of Delay–Doppler Maps of Reflected Global Navigation Satellite System Signals," *IEEE Transactions on Geoscience and Remote Sensing,* vol. 47, no. 8, pp. 2733-2740, Aug. 2009.

[199] H. Park, E. Valencia, N. Rodriguez-Alvarez, X. Bosch-Lluis, I. Ramos-Perez, and A. Camps, "New approach to sea surface wind retrieval from GNSS-R measurements," in *2011 IEEE International Geoscience and Remote Sensing Symposium (IGARSS),* pp. 1469–1472, July 2011.

[200] M. Clarizia *et al.,* "Analysis of GNSS-R delay-Doppler maps from the UK-DMC satellite over the ocean," *Geophysical Research Letters,* vol. 36, no. 2, art. ID L02608, Jan. 2009.

[201] "GeoHack - Hibernia Gravity Base Structure," W. T. Labs, [Online]. Available: `https://tools.wmflabs.org/geohack/geohack.php?pagename=Hibernia_Gravity_Base_Structure&params=46_45_1.57_N_48_46_58.54_W_`. [Accessed Sep. 20, 2016].

[202] J. Maslanik and J. Stroeve, “Near-Real-Time DMSP SSMIS Daily Polar Gridded Sea Ice Concentrations, Version 1. [nt_20150401_f17_nrt_n],” NASA National Snow and Ice Data Center Distributed Active Archive Center, Boulder, CO, USA, [Online]. Available: http://nsidc.org/data/nsidc-0081#. [Accessed Oct. 17, 2016].

[203] L. Guoyo, *World Atlas of Oil and Gas Basins,* Chichester, UK: Wiley-Blackwell, 2011.

[204] “Number of offshore rigs worldwide as of 2015, by region,” The Statistics Portal, [Online]. Available: https://www.statista.com/statistics/279100/number-of-offshore-rigs-worldwide-by-region/. [Accessed Sep. 21, 2016].